

Measurements and Simulations with the Extended KATRIN Muon Detector System

submitted
Master Thesis of

Richard Rink

Institute for Experimental Nuclear Physics
Karlsruhe Institute of Technology

Reviewer:	Prof. Dr. Guido Drexlin
Second reviewer:	Prof. Dr. Ulrich Husemann
Advisor:	Dr. Florian Fränkle

Duration: 16. October 2013 – 15. October 2014

I declare that I have developed and written the enclosed thesis completely by myself, and have not used sources or means without declaration in the text.

Karlsruhe, 15.10.2014

.....
(Richard Rink)

Abstract

Neutrinos are the most abundant massive Standard Model particles in the universe. Neutrino oscillation experiments showed that neutrinos are massive particles, however the absolute mass scale of neutrinos is still unknown and one of the big open questions in particle physics. So far only upper and lower limits exist. The **K**Arlsruhe **T**RItium **N**eutrino (KATRIN) experiment aims to determine the effective mass of the electron antineutrino with a sensitivity of $200 \text{ meV}/c^2$ (90% C.L.). To achieve this sensitivity, a total background rate in the order of 0.01 counts per second is required. In order to determine the neutrino mass, KATRIN will measure the tritium β -spectrum in the endpoint region ($\sim 18.6 \text{ keV}$) with a high-resolution electrostatic spectrometer of MAC-E filter type.

This thesis focusses on the investigation of a major background component, the emission of muon induced secondary electrons from the inner surface of the spectrometer vessel. For detailed studies of this background, a set of muon detectors is installed close to the spectrometer. This allows the search for correlations between muons crossing the spectrometer tank and background counts at the focal plane detector (FPD) system. Within the frame of this thesis, the muon detection system was extended by mounting an additional scintillator module on a movable platform above the spectrometer. Measurements and corresponding simulations were performed in order to investigate the performance of the extended system. The system features a high spatial resolution at relatively high coincidence rates. Geant4 was used to simulate muons inciding on the main spectrometer and their interactions with the muon detectors. The interaction points at the inner spectrometer surface of muons, detected by the muon system, were used as start parameters of secondary electrons for further electromagnetic simulations. For this, the particle tracking software Kassiopeia was used. The combination of these two simulation programs is a powerful method, that offers the possibility to derive expectations for coincidence measurements of the upcoming spectrometer detector system commissioning phase.

The cosmic muon flux at sea level depends on various parameters like temperature or pressure in the atmosphere and therefore is not constant over time. It is expected that the KATRIN background will be dominated by secondary electrons due to cosmic muons. Any variation of the muon flux therefore translates in a variation of the background rate and thus creating a non-Poissonian distributed background, which might decrease the neutrino mass sensitivity. A long term measurement over three months was performed to determine the magnitude of these variations on long times scales. In this context, also the stability of the muon modules was investigated. A sensitivity analysis using the Kasper module KaFit is presented. A background model was developed in order to determine the influence of the muon flux fluctuations on the sensitivity. It combines the expected Poissonian nature of the background on short time scales with the expected non-Poissonian nature on long time scales. For the used background model and a mean background rate of 10 mcps within the uncertainties no deviation from the reference sensitivity with Poissonian distributed background (197 meV) could be observed. At higher background rates worse sensitivities were determined compared to a purely Poissonian background. For a 100 mcps mean background scenario, the sensitivity decreases from 254 meV to 266 meV and for 400 mcps

from 324 meV to 393 meV.

Zusammenfassung

Neutrinos sind die am häufigsten vorkommenden massiven Teilchen des Standardmodells im Universum. Experimente zur Untersuchung von Neutrinooszillationen haben gezeigt, dass Neutrinos massive Teilchen sind. Allerdings ist ihre absolute Massenskala noch unbekannt und eine der großen Fragen der Teilchenphysik. Bisher existieren nur obere Schranken auf die Neutrinomasse. Das **K**ARlsruhe **TR**Itium **N**eutrino (KATRIN) Experiment plant die effektive Masse des Elektronantineutrinos mit einer bisher unerreichten Sensitivität von $200 \text{ meV}/c^2$ zu messen (90% C.L.). Um diese Sensitivität zu erreichen muss eine Untergrundrate in der Größenordnung von 0,01 Ereignissen pro Sekunde erreicht werden. KATRIN wird das integrierte β -Spektrum von Tritium in der Endpunktregion ($\sim 18.6 \text{ keV}$) messen mit einem hochauflösenden elektrostatischen Spektrometer vom Typ MAC-E-Filter.

Diese Arbeit beschäftigt sich im Wesentlichen mit einer der Hauptuntergrundquellen, der myoninduzierten Emission von Sekundärelektronen von der inneren Tankwand des Spektrometers. Um diese Untergrundquelle genau zu untersuchen, wurde ein Myon-Detektor-System nahe am Spektrometer installiert. Dies ermöglicht es, nach Korrelationen zwischen Myonen, welche den Tank durchqueren, und Untergrundereignissen am Fokalebeneendetektor zu suchen. Im Rahmen dieser Arbeit wurde das bestehende Myon-Detektor-System durch ein zusätzliches Szintillatormodul auf einer beweglichen Plattform über dem Spektrometer erweitert. Messungen und entsprechende Simulationen wurden durchgeführt, um die Leistungsfähigkeit des erweiterten Systems zu überprüfen. Das System zeichnet sich durch eine hohe Ortsauflösung und durch relativ hohe Koinzidenzraten aus. Geant4 wurde verwendet, um auf das Spektrometer und die Myondetektoren einfallende kosmische Myonen zu simulieren. Die Punkte an denen Myonen, welche in den Myondetektoren registriert wurden, die Tankwand treffen, wurden als Startparameter für weitere elektromagnetische Simulationen verwendet. Hierfür wurde die Trackingsoftware Kassiopeia benutzt. Die Kombination dieser beiden Simulationsprogramme ermöglicht es, Vorhersagen für Koinzidenzmessungen der bevorstehenden Messphase mit Spektrometer und Detektorsystem zu machen.

Der Fluss kosmischer Myonen auf Meereshöhe hängt von verschiedenen Parametern wie beispielsweise der Temperatur oder dem Druck in der Atmosphäre ab. Daher ist dieser zeitlichen Schwankungen unterworfen. Es wird erwartet, dass der Untergrund von KATRIN durch Sekundärelektronen, induziert von kosmischen Myonen, dominiert wird. Variationen in der Myonrate übertragen sich auf den Untergrund und erzeugen so einen nicht-poissonverteilten Untergrund, welcher sich negativ auf die Sensitivität auswirken könnte. Eine Langzeitmessung des Myonflusses über drei Monate wurde durchgeführt um die Stärke dieser Schwankungen auf langen Zeitskalen zu bestimmen. Ebenfalls wurde die Langzeitstabilität der Myonmodule bestimmt. Eine Sensitivitätsuntersuchung mit dem Kasper-Modul KaFit wurde durchgeführt. Eine Untergrundmodell wurde entwickelt, um den Einfluss dieser Untergrundkomponente auf die Sensitivität von KATRIN zu untersuchen. In diesem Modell wird angenommen, dass der Untergrund auf kurzen Zeitskalen poissonverteilt ist, aber auf langen Zeitskalen eine nicht-poissonverteilte Komponente hat.

Unter Annahme dieses Untergrundmodells konnte für eine mittlere Untergrundrate von 0,01 Ereignissen pro Sekunde innerhalb der Unsicherheiten keine Abweichung von der Sensitivität bei einem rein poissonverteilten Untergrund (197 meV) beobachtet werden. Für höhere Untergrundraten ergeben sich schlechtere Sensitivitäten verglichen mit einem poissonverteilten Untergrund der selben mittleren Rate. Für eine mittlere Untergrundrate von 0,1 Ereignissen pro Sekunde ergibt sich eine Verschlechterung der Sensitivität von 254 meV zu 266 meV und für 0,4 Ereignissen pro Sekunde eine Verschlechterung von 324 meV zu 393 meV.

Contents

1. Neutrino Physics	1
1.1. Historical Overview	1
1.1.1. Postulation of the Neutrinos	1
1.1.2. First Detection of the Neutrino	1
1.2. Neutrinos in the Standard Model	3
1.3. Neutrino Sources	3
1.3.1. Primordial Neutrinos	3
1.3.2. Supernova Neutrinos	3
1.3.3. Atmospheric Neutrinos	4
1.3.4. Solar Neutrinos	4
1.3.5. Geo Neutrinos	4
1.3.6. Reactor Neutrinos	4
1.3.7. Accelerator Neutrinos	4
1.4. Neutrino Oscillations	5
1.4.1. Discovery	5
1.4.2. Theoretical Formalism	7
1.5. Determination of the Neutrino Mass	7
1.5.1. Single Beta Decay	8
1.5.2. Neutrinoless Double Beta Decay	8
1.5.3. Cosmology	10
2. KATRIN Experiment	11
2.1. Measurement Principle	11
2.2. MAC-E Filter	12
2.3. Experimental Setup	13
2.3.1. WGTS and Rear Section	14
2.3.2. Transport Section	14
2.3.3. Pre-Spectrometer	15
2.3.4. Main Spectrometer	15
2.3.5. Monitor Spectrometer	16
2.3.6. Focal Plane Detector System	16
2.4. Background Sources	17
2.4.1. Secondary Electrons from Surfaces	17
2.4.2. Magnetically Stored Particles	18
3. Muon Detection System	19
3.1. Scintillator Modules	19
3.2. Photomultipliers	20
3.3. Module Positions	20
3.4. DAQ System	22
3.5. Muon Panel Operational Parameters and Performance	23
3.5.1. Large Modules	23

3.5.2. Small Module	24
4. Measurements with an Extended Muon System	27
4.1. Motivation	27
4.2. Test Measurement Setup	28
4.3. Coincidence Rates	29
5. Simulations with the Extended Muon System	31
5.1. Geant4	31
5.2. Simulation Setup	32
5.3. Coincidence Rates	34
5.4. Extraction of Surface Crossing Points	35
5.5. Kassiopeia	37
5.6. Resulting Pixel Distributions	38
6. Long Term Muon Measurement	41
6.1. Long Term Stability of Muon Modules	41
6.2. Muon Rate Variations	43
6.3. Sensitivity Investigations with non-Poissonian Background	44
6.3.1. Sensitivity Definition	44
6.3.2. KaFit	45
6.3.3. KATRIN Likelihood Function	46
6.3.4. Muon Data Background Model	48
6.3.5. Ensemble Test	49
6.3.6. Statistical Uncertainties	51
7. Conclusion	55
Bibliography	57
Appendix	61
A. 2D Simulation of Radon First Spike Events	61
A.1. Spike Events	61
A.2. Simulation Model	63
A.3. Comparison of Simulation and Data	64
B. Muon Flux Generator	67
C. Muon Panel Performance	69
D. Surface Interaction Points of Coincidence Events	73
E. ADC Peak Positions	77
F. Run Descriptions Web Page	79
List of Figures	82
List of Tables	83

1. Neutrino Physics

This chapter is a general overview of neutrino physics. It covers the postulation of the neutrino by W. Pauli in 1930 [1] and the first experimental observation of a neutrino in 1956 by L. Cowan and F. Reines [2]. Then the various neutrino sources are described. Afterwards neutrino oscillations are explained, which were firstly observed in 1998 by the Super-Kamiokande experiment [3] and could show that neutrinos are massive particles. Conclusively, different methods to measure absolute neutrino masses are described.

1.1. Historical Overview

Since the theoretical postulation of the neutrino, various efforts were undertaken to obtain an experimental proof for its existence. Finally, it took more than 20 years to confirm the neutrino experimentally.

1.1.1. Postulation of the Neutrinos

In 1914 J. Chadwick investigated the electron energy spectrum from nuclear β -decays [4]. At this time α -, β - and γ -decays were of great interest. In contrast to α - and γ -decays where the spectrum shows discrete lines, Chadwick measured a continuous β -spectrum. For a two-body decay this was not explainable under the assumption of energy and momentum conservation. This even led to theories that put a question mark over the law of energy conservation. W. Pauli tried to explain the observation on 4th December of 1930 with his famous letter to his colleagues [1]. He postulated a neutral spin 1/2 particle that is produced in the β -decay together with the electron.

As β -decay becomes a three-body process, the released energy is split between the two emitted particles, which explains the continuous energy spectrum of the electrons. Pauli called the introduced new particle "neutron". Due to its extreme weak interaction, an experimental confirmation of this theory was not possible at that time. In 1932 Chadwick found a particle with similar properties today known as neutron [6]. But it turned out that its mass is much higher than the one introduced by Pauli (mass in order of electron mass). Afterwards E. Fermi formulated the theoretical description of β -decay [7], which is still established today.

1.1.2. First Detection of the Neutrino

Due to the weak interaction of neutrinos it was a challenge and took more than 20 years to receive an independent experimental proof for the existence of the neutrino. In 1956

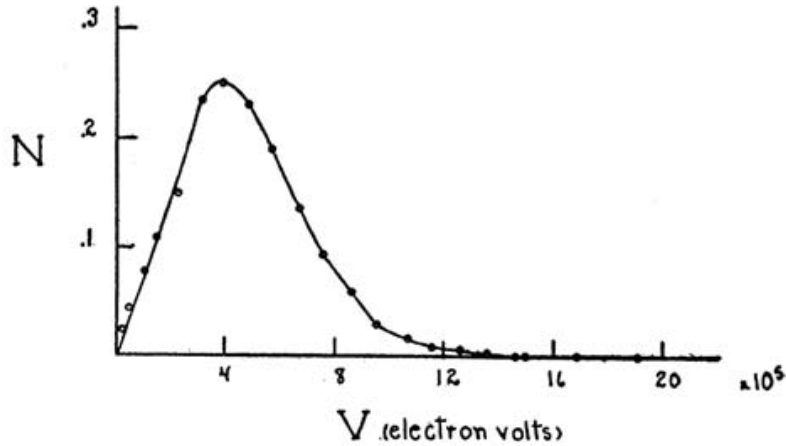


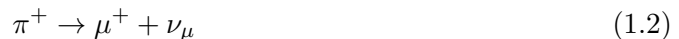
Figure 1.1.: Continuous Radium β -spectrum. Figure from [5]

L. Cowan and F. Reines built up a series of experiments, known as project "Poltergeist". The Savannah river fission reactor served as neutrino source. With the first detector the background rate was too high. Using an improved detector [2] they were able to detect neutrinos and therefore confirm Pauli's postulation. The detector was a water tank with CdCl_2 , surrounded by scintillator material and photomultipliers (PMT). This allowed to detect neutrinos via inverse β -decay:



The annihilation of the positron with an electron in the water produces two 511 keV gammas. Compton scattering of these gammas produces scintillation light that is detected by the PMTs. The neutron is thermalised in the water and captured by Cd nucleus after a few microseconds. This leads to an excited Cd^* nucleus that releases its energy again by emitting gammas. These gammas are delayed with respect to the two photons from the electron positron annihilation. This clear signature allowed to identify neutrino events and was the first experimental proof for the existence of neutrinos, more precisely the $\bar{\nu}_e$.

The muon neutrino was discovered in 1962 by L.M Ledermann, M. Schwartz and J. Steinberger by investigating the pion decay at the particle accelerator Alternating Gradient Synchrotron [8].



The muons were shielded so that only the neutrinos were able to pass the barrier. A detector was placed behind the shielding where muons could be detected. This showed that there was a second kind of neutrino interacting with the detector with different behaviour than the already known electron neutrino exists. Finally, in the year 2000 the third kind of neutrino, ν_τ was discovered at the Fermilab in the DONUT experiment [9]. A proton beam was shot on a tungsten target. Among other particles, D_S mesons were created in this collision.



The beam of τ -leptons and thus its decay products, i.e. also $\bar{\nu}_\tau$ -s, were focused on a target consisting of stainless steel layers and emulsion plates. The neutrinos produce τ -leptons within the stainless steel and their track can be determined with the emulsion plates. When the τ decay, they also produce neutrinos, which results in a kink in the trajectory due to missing energy.

1.2. Neutrinos in the Standard Model

The Standard Model [10] describes the elementary particles and their interactions. It is widely established as it has passed a lot of tests and is in very good agreement with many precision measurements. It contains twelve fermions, six leptons and six quarks, and their antiparticles. Their interactions are described by 4 gauge bosons. The Higgs boson is responsible for particle masses. Today all particles of the standard model have been detected. The last one, a Higgs-like particle, was discovered in 2012 at CERN [11][12]. Figure 1.2 shows the particles and their mass, charge and spin. The fermions are arranged in 3 columns that correspond to three generations. Ordinary matter consists of particles of the first generation/column. The other particles are produced in cosmic air showers, accelerator experiments or nuclear reactors for instance. In each generation there are two

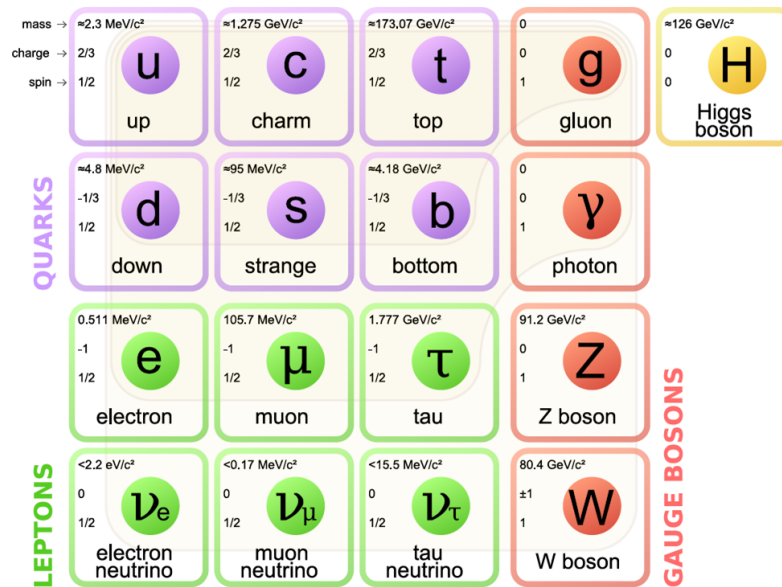


Figure 1.2.: Overview of elementary particles and their properties in the SM. Figure taken from [13]

leptons. One carries electric charge and can interact electromagnetically and weakly. The second one, the neutrino, is electrically neutral and thus can only interact via the weak force. Therefore, the detection of neutrinos is a very challenging task.

1.3. Neutrino Sources

There are a number of different neutrino sources over a wide energy range. Most of them are natural, but there are also artificially produced neutrinos e.g. from nuclear reactors. This section gives a short overview over some important neutrino sources.

1.3.1. Primordial Neutrinos

In the early universe a large number of neutrinos was produced. Since the time of the freeze out of the weak interaction, a large number of neutrinos propagates freely through space. These relic neutrinos have energies in the order of a few meV and their density is about $336/\text{cm}^3$.

1.3.2. Supernova Neutrinos

A supernova (SN) emerges when a star reaches the end of his life cycle. Type 2 SN, which can only occur for a star with higher mass than the Chandrasekha limit ($M > 8M_{\odot}$),

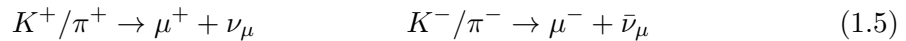
produce a huge number of neutrinos. In a type 2 SN, the star collapses when no nuclear fuel is left and no core fusion is possible anymore. A shock wave rejects the outer layer of the star into space and the large gravitational pressure enables electron capture:



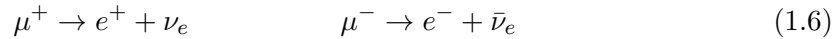
The core becomes a very hot ($\approx 10^{11}$ K) and dense neutron star. The neutrinos cool the core by carrying away most of its energy. The majority of the neutrinos is emitted within a time window of about 10 s. This relatively short neutrinos-pulse of SN1998a could be measured with the Super-Kamiokande experiment [3].

1.3.3. Atmospheric Neutrinos

Cosmic rays, which mostly consist of protons, interact in the atmosphere with nitrogen and hydrogen molecules. In the resulting cosmic air showers of secondary particles, pions π^\pm and kaons K^\pm are produced in a cascade. In the decay process of these particles muons, ν_μ and their antiparticles are produced:



In the muon decay additionally, electrons and ν_e are produced, or their antiparticles respectively.



1.3.4. Solar Neutrinos

A large fraction of the neutrino flux on Earth originates from fusion reaction in the inner core of the sun. The dominant reaction is the proton-proton fusion:



This fusion takes place in several steps where many neutrinos are produced. Another fusion chain is the carbon-nitrogen-oxygen-cycle. Figure 1.3 shows the solar neutrino spectrum expected by the Standard Solar Model (SSM). The first measurements of the solar neutrino flux showed a significant deficit to the expectations, which boosted the theory of neutrino oscillations. This is described in 1.4.1 in more detail.

1.3.5. Geo Neutrinos

Radionuclides like ${}^{238}\text{U}$, ${}^{232}\text{Th}$ or ${}^{40}\text{K}$ appear naturally on the Earth. In their decay-chains antineutrinos with MeV energies are produced. Studying geo neutrinos also provides informations about geophysical processes and the internal structure of the Earth [15].

1.3.6. Reactor Neutrinos

An artificial neutrino source on the Earth are nuclear fission reactors. In the β -decays of fission products a huge number of neutrinos is produced. Each fission produces on average six neutrinos with MeV energies, which are emitted isotropically. Due to the high flux reactor neutrinos can be used to investigate neutrino oscillation parameters.

1.3.7. Accelerator Neutrinos

Particle accelerators can be used to produce a beam of high energetic neutrinos. Commonly protons are shot on a target of graphite or beryllium where pions and kaons are produced. The pions and kaons are then further focussed and separated by their electric charge. They decay (equation 1.5) and by shielding the other decay products a focussed neutrino beam with GeV energies is generated. In combination with a remote neutrino detector, the beam can be used for neutrino oscillation studies.

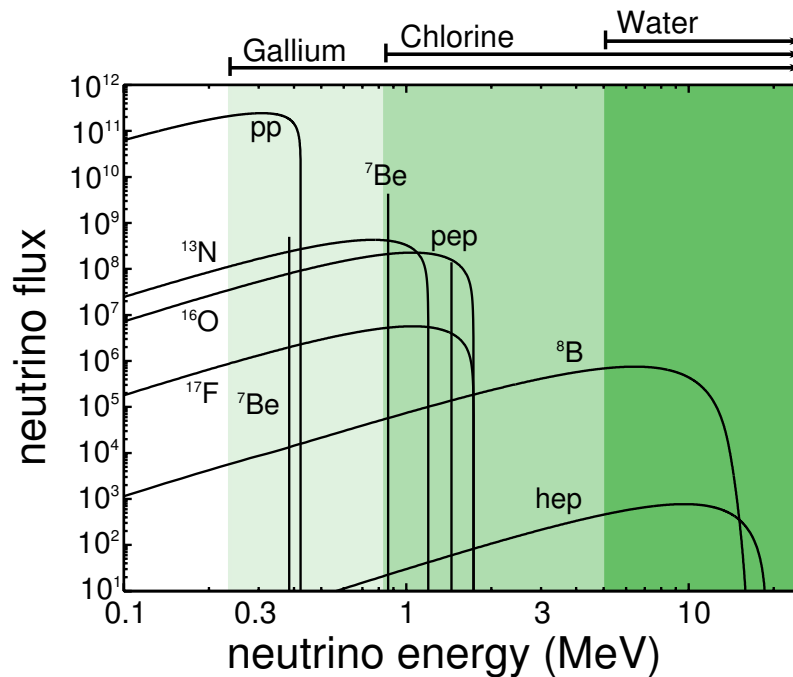


Figure 1.3.: Solar neutrino spectrum for various production mechanisms. The sensitive regions for different detector materials are shown. [14]

1.4. Neutrino Oscillations

In the standard model 1.2, neutrinos are assumed to be massless. The observation of oscillations of atmospheric neutrinos in 1998 [3] was the first proof that neutrinos are massive particles. This has extensive consequences for particle physics and cosmology. The oscillation phenomena is based on the fact that the neutrino flavour eigenstates are not equal to the neutrino mass eigenstates. The theoretical description was first formulated by Pontecorvo in 1957 [16] and extended by Maki, Nakagawa and Sakata in 1962 [17]. The mixing of neutrinos is described by the PMNS-matrix¹.

1.4.1. Discovery

A first hint on a non-zero neutrino mass was found by R. Davis with the homestake experiment. In the sun electron neutrinos are produced in fusion reactions 1.3.4. Davis detected neutrinos from the sun with a radiochemical detection technique [18]. The detector consisted of a tank filled with 600 t perchlorethylen. The solar neutrinos interact with the nucleus of the ^{37}Cl isotope, which transmutes into an argon atom:



Via electron capture the argon nucleus becomes an excited $^{37}\text{Cl}^*$ nucleus, which goes back to the ground state by emitting auger electrons. By extracting the argon atoms he was able to detect the auger electrons with proportional counters. For his experiment he received the Nobel prize in physics in 2002. Considering the distance between Earth, he determined the neutrino flux through the detector. The measured number of ν_e was smaller than the prediction of the Standard Solar Model (SSM). This result was confirmed by other experiments like GALLEX [20], GNO [21], or Kamiokande [22] and was called the "solar neutrino problem". As a consequence, the validity of the SSM was put into question. An other explanation is that there are neutrino flavour changes during their

¹Pontecorvo, Maki, Nakagawa, Sakai

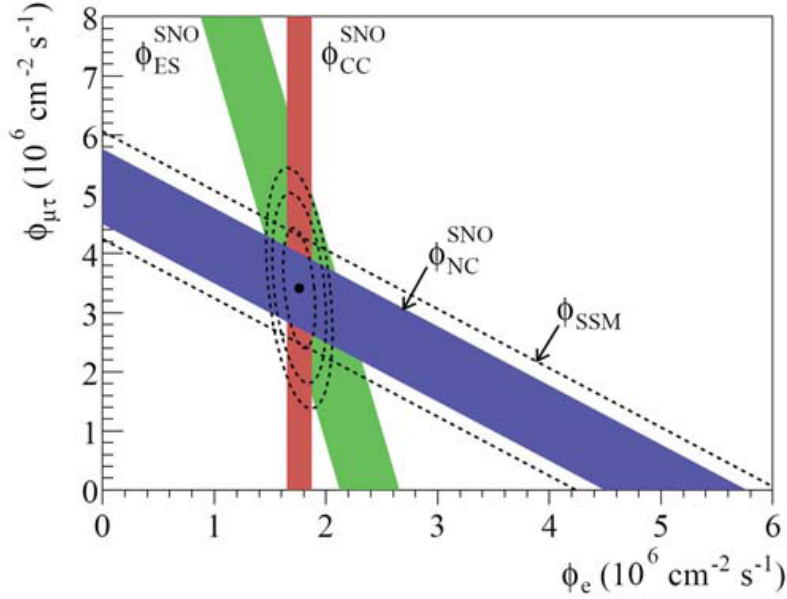


Figure 1.4.: The bands show the rates for different reactions determined at SNO in the plane of electron neutrino flux and the sum of muon and tau neutrino flux. As the ES reaction is only possible for electron electron neutrinos this reaction sets the flux of ν_e . The probability for the NC reaction is equal for all three flavours. Thus the NC rate determines the total neutrino flux, which is in good agreement of the SSM model. The intersection area suggests that 1/3 of all neutrinos are ν_e and 2/3 are ν_μ and ν_τ . Figure from [19]

way from the sun to the Earth. The Sudbury Neutrino Observatory was able to confirm the hypotheses that neutrinos undergo neutrino oscillations by measuring the total solar neutrino flux of all three neutrino flavours, thus solving the solar neutrino problem [23]. A target of 1 kt heavy water D_2O was used. The neutrinos can interact via elastic scattering (ES), neutral current (NC) and charged current (CC). ES is only possible for ν_e :

$$\nu_\alpha + e^- \rightarrow \nu_\alpha + e^- \quad (1.9)$$

All flavours can interact via NC:

$$\nu_\alpha + d \rightarrow \nu_\alpha + p + n \quad (1.10)$$

The CC reaction is also possible for all flavours but the dominant contribution comes from ν_e :

$$\nu_e + d \rightarrow e^- + p + p \quad (1.11)$$

Each reaction produces a different signal in the detector that allows to obtain the rates for ES, NC and CC. Because ES is only possible for ν_e and the neutrino fluxes enter with different weight into CC and NC one can extract the individual flavour flux by determining the frequency of the three channels.

$$\Phi_{\text{tot}} = \Phi_{\text{ES}} + \Phi_{\text{NC}} + \Phi_{\text{CC}} \quad (1.12)$$

$$\Phi_{\text{ES}} = \Phi_e \quad (1.13)$$

$$\Phi_{\text{NC}} = \Phi_e + \Phi_{\mu\tau} \quad (1.14)$$

$$\Phi_{\text{CC}} = \Phi_e + 0.13 \cdot \Phi_{\mu\tau} \quad (1.15)$$

The results are shown in figure 1.4. The total neutrino flux is composed of 1/3 ν_e and 2/3 ν_μ and ν_τ [24][19]. This shows that the SSM is correct and verifies the existence of neutrino oscillations.

1.4.2. Theoretical Formalism

Neutrinos can be described theoretically by two different sets of eigenstates. One set of eigenstates $|\nu_\alpha\rangle$ ($\alpha = e, \mu, \tau$) that is defined by the weak interaction and one set $|\nu_i\rangle$ ($i = 1, 2, 3$), defined by the mass. The two sets are not identical and related over the PMNS-matrix ² U:

$$|\nu_\alpha\rangle = \sum_i U_{\alpha i} |\nu_i\rangle \quad (1.16)$$

The matrix U can be parametrised by 3 rotation angles, one complex Dirac phase δ_D and two complex Majorana phases $\delta_{M1/2}$. The complex phases can cause CP violation in the lepton sector.

$$U = \begin{pmatrix} 1 & 0 & 0 \\ 0 & c_{2,3} & s_{2,3} \\ 0 & -s_{2,3} & c_{2,3} \end{pmatrix} \begin{pmatrix} c_{1,3} & 0 & s_{1,3}e^{-i\delta_D} \\ 0 & 1 & 0 \\ -s_{1,3}e^{-i\delta_D} & 0 & c_{1,3} \end{pmatrix} \begin{pmatrix} c_{1,2} & s_{1,2} & 0 \\ -s_{1,2} & c_{1,2} & 0 \\ 0 & 0 & 1 \end{pmatrix} \begin{pmatrix} e^{i\delta_{M1}} & 0 & 0 \\ 0 & e^{i\delta_{M2}} & 0 \\ 0 & 0 & 1 \end{pmatrix} \quad (1.17)$$

Abbreviations: $s_{i,j} = \sin(\Theta_{i,j})$, $c_{i,j} = \cos(\Theta_{i,j})$.

At the time a neutrino is produced it is in a pure flavour eigenstate $|\nu_\alpha\rangle$, which is a superposition of mass eigenstates:

$$|\nu_\alpha(t=0)\rangle = U_{\alpha 1}^* |\nu_1\rangle + U_{\alpha 2}^* |\nu_2\rangle + U_{\alpha 3}^* |\nu_3\rangle \quad (1.18)$$

With the neutrino energy E the time dependent state is given by:

$$|\nu_\alpha(t)\rangle = U_{\alpha 1}^* e^{-iE_1 t} |\nu_1\rangle + U_{\alpha 2}^* e^{-iE_2 t} |\nu_2\rangle + U_{\alpha 3}^* e^{-iE_3 t} |\nu_3\rangle \quad (1.19)$$

For $t > 0$ this state is no longer a pure flavour eigenstate. The probability to find a neutrino in a certain state $|\nu_\beta\rangle$ is then the projection of the time dependant state $|\nu_\alpha(t)\rangle$ on $|\nu_\beta\rangle$:

$$P(\nu_\alpha \rightarrow \nu_\beta(t)) = |\langle \nu_\beta(t) | \nu_\alpha(t) \rangle|^2 = \sum_{kj} U_{\alpha k}^* U_{\beta k} U_{\alpha j} U_{\beta j}^* e^{-i(E_k - E_j)t}. \quad (1.20)$$

Assuming ultra relativistic neutrinos the approximation $p_k = E$ yields

$$P(\nu_\alpha \rightarrow \nu_\beta(L/E)) = |\langle \nu_\beta | \nu_\alpha(t) \rangle|^2 = \sum_{kj} U_{\alpha k}^* U_{\beta k} U_{\alpha j} U_{\beta j}^* e^{-i \frac{\Delta m_{kj}^2 L}{2E}}, \quad (1.21)$$

with $\Delta m_{kj}^2 = m_k^2 - m_j^2$, L the distance between neutrino production and detector and the neutrino energy E . As one can obtain from equation 1.21, this oscillation behaviour depends on the squared mass differences. Thus, the oscillation behaviour contains no information about the absolute neutrino masses. Recent experimentally determined oscillation parameters can be found in [25].

1.5. Determination of the Neutrino Mass

There are different methods to determine the mass of neutrinos. One way is the investigation of β -decay kinematics, which is the only model independent approach. Alternatives are the search for neutrinoless double beta decay ($0\nu\beta\beta$) and cosmological observations.

²Pontecorvo-Maki-Nakagawa-Sakata-matrix[17]

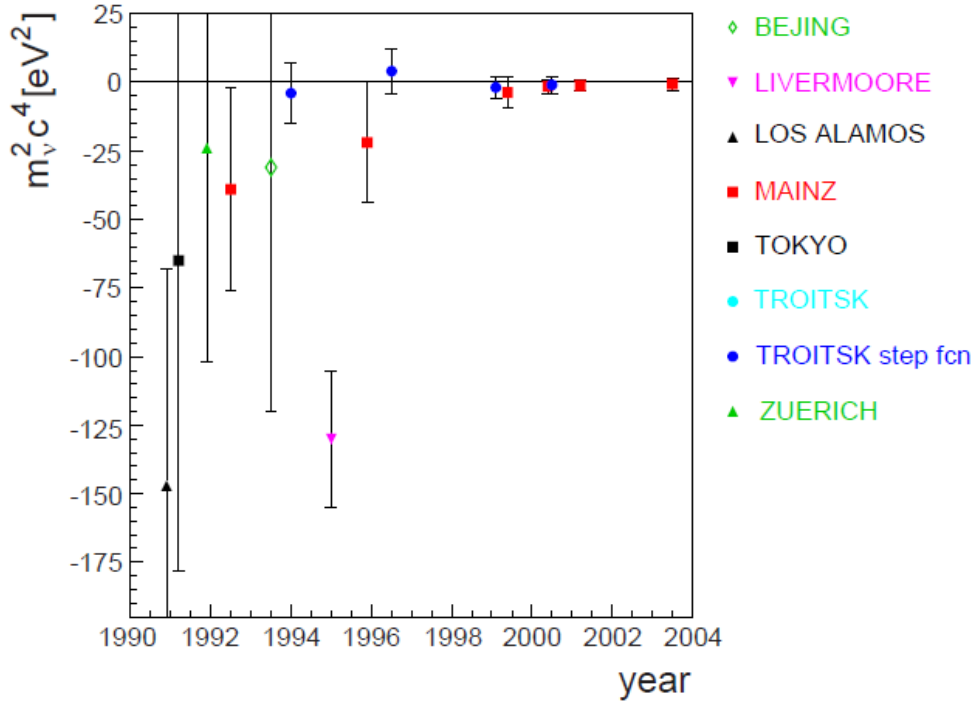


Figure 1.5.: Upper limits on $m_{\nu_e}^2$ measured by β decay experiments in the past. The current best limit is $m_{\nu_e}^2 < 2 \text{ eV}^2$ [25] set by experiments in Mainz and Troitsk. Figure taken from [27]

1.5.1. Single Beta Decay

An approach to determine the neutrino mass is the measurement of a β -electron spectrum with very high accuracy. This method is based on the relativistic energy-momentum relation and thus is mainly model independent. A theoretical description of the β -spectrum (equation 2.2) can be derived with the Fermi theory where the effective neutrino mass $m_{\nu_e}^2$, which is the incoherent sum of the mass eigenvalue, enters as a parameter [26]:

$$m_{\nu_e}^2 = \sum_{i=1}^3 |U_{ei}|^2 \cdot m_{\nu_i}^2 \quad (1.22)$$

This is due to the fact that in the β -decay flavour eigenstates ν_e are produced, which are not identical to the mass eigenstates. An experimental approach to measure the electron energies are electrostatic spectrometers. A variable retarding potential filters electrons below a certain threshold. Thus, the integrated β -spectrum can be measured. To achieve a high sensitivity, a large scale of the spectrometers is required. That is the way the KATRIN experiment aims to determine $m_{\nu_e}^2$ using molecular tritium as a source. A more detailed description of the measurement principle is given in section 2.1. Direct measurements were already performed by several experiments in the past. Until now, no absolute neutrino mass could be measured, but upper limits could be obtained. Figure 1.5 contains the upper limits on $m_{\nu_e}^2$ determined by these experiments.

1.5.2. Neutrinoless Double Beta Decay

The double β -decay ($2\nu\beta\beta$) is a weak process of second order which can only be observed when the single β -decay is energetically forbidden. Two neutrinos and two electrons or positrons are emitted. It was first discovered in 1987 for ^{82}Se [28]. E.Majorana developed

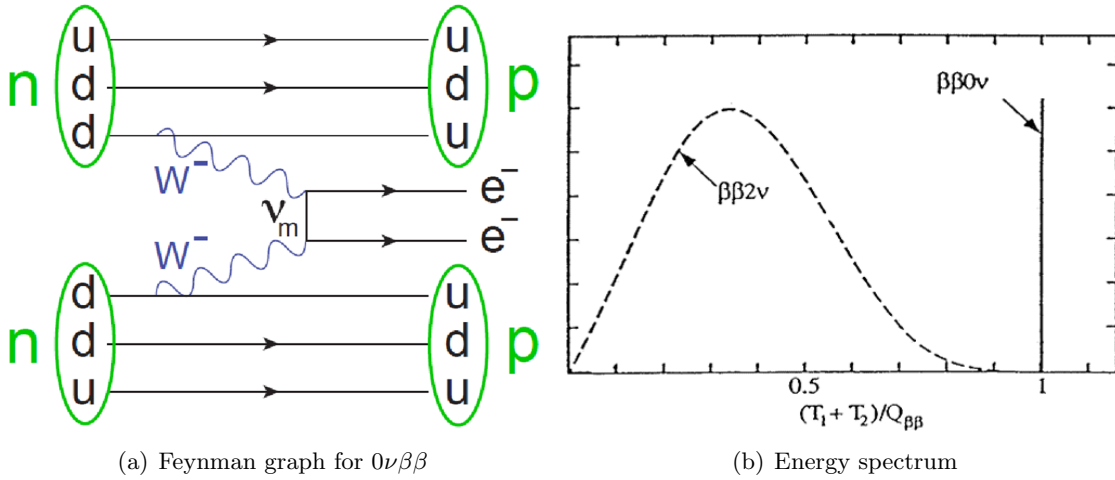


Figure 1.6.: **a:** Feynman diagram for neutrinoless double beta decay. A virtual neutrino is emitted and absorbed as antineutrino in the other vertex. Figure from [29]. **b:** Double β -decay energy spectrum. The continuum belongs to $2\nu\beta\beta$ decays, the peak the $0\nu\beta\beta$ decays. Figure taken from [30]

a theory in which neutrinos can be their own antiparticles (majorana particles) [31]. If neutrinos are indeed majorana particles the two neutrinos produced in the double β -decay can annihilate in a virtual process. The atomic number Z of the initial nucleus with mass number A increases by 2 and the released energy is split between the two emitted electrons or positrons:

$$N(A, Z) \rightarrow N(A, Z \pm 2) + 2e^{\mp} \quad (1.23)$$

As only two particles are emitted the two e^{\pm} need to have a fixed energy because of energy and momentum conservation. Thus, a mono-energetic line at the end of the $2\nu\beta\beta$ spectrum is expected. Because of violation of lepton number conservation this process is forbidden in the SM. Figure 1.6(a) shows the Feynman graph for this process. The neutrino emitted in one vertex has to be absorbed at the other vertex with inverted helicity. Therefore, a non-zero neutrino mass is required as for massless particles the helicity is conserved. Massive particles are in a mixed helicity state. This experimental approach is sensitive to the effective majorana mass:

$$m_{ee} = \left| \sum_{i=1}^3 U_{ei}^2 \cdot m_i \right|. \quad (1.24)$$

As m_{ee} is the coherent sum of the mass eigenvalues, cancellations can arise. This means a smaller neutrino mass would be detected than in single β -decay experiments. The observable in $0\nu\beta\beta$ experiments is the half life $T_{1/2}^{0\nu\beta\beta}$ which can be theoretically described by

$$(T_{1/2}^{0\nu\beta\beta})^{-1} = G^{0\nu\beta\beta}(Q_{\beta\beta}, Z) \cdot \left| M_{GT}^{0\nu\beta\beta} - \left(\frac{g_V}{g_A} \right)^2 M_F^{0\nu\beta\beta} \right|^2 \cdot \frac{\langle m_{ee} \rangle}{m_e^2} \quad (1.25)$$

with phase space factor $G^{0\nu\beta\beta}$, endpoint energy $Q_{\beta\beta}$, atomic number Z , Gamov-Teller $M_{GT}^{0\nu\beta\beta}$ and Fermi matrix elements $M_F^{0\nu\beta\beta}$, axial and vector coupling constants g_V and g_A , and electron mass m_e . The value of interest m_{ee} enters as parameter. There are large uncertainties on the matrix elements. Until now the Heidelberg-Moskau experiment has reached the best sensitivity on $0\nu\beta\beta$. Parts of the collaboration take the view to have found evidence for $m_{ee} = 0.32 \text{ eV}$ [32]. This was content of controversial debates in the field of neutrino research and disputed by the community [33]. Currently there are various double beta experiments like GERDA [34], MAJORANA [35], CUORE [36] and EXO [37].

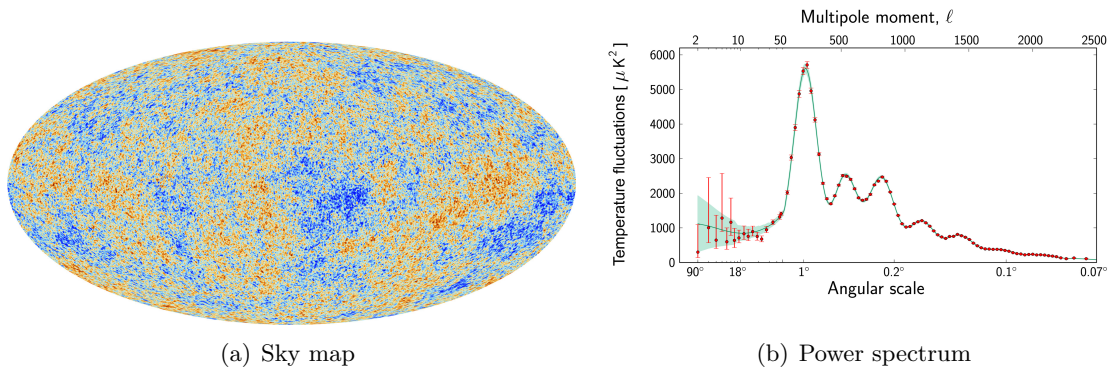


Figure 1.7.: CMB temperature fluctuations measured with the Planck space telescope: **a**: Skymap of small anisotropies in order of μK . Larger anisotropies are excluded. **b**: Dependence of temperature fluctuations on angular scale. Figure taken from [41]

Recent results of the GERDA experiment can mainly exclude the controversial Heidelberg-Moscow claim [38].

1.5.3. Cosmology

Cosmological observations can be used to derive a statement about neutrino masses. However, such approaches are rather model dependent. The cosmic microwave background (CMB) is an isotropic black body radiation with a temperature of 2.7 K [39] and was discovered in 1965 [40]. It originates from the time photons decoupled from matter ca. 10^5 years after the big bang at a temperature of 3000 K. Afterwards the photons cooled down due to the universe's expansion. The CMB carries information about structures in the universe at the time of decoupling. Extensive studies of the CMB were undertaken by satellite experiments. Small anisotropies in the order of μK were found, beside larger anisotropies originating from the Doppler effect and other perturbations. A skymap of the anisotropies on the μK scale is shown in 1.7(a). The fluctuations can be described by spherical harmonics:

$$\frac{\Delta T}{T}(\Theta, \phi) = \sum_{\ell m} a_{\ell m} Y_{\ell m}(\Theta, \phi) \quad (1.26)$$

The power spectrum measured with the Planck space telescope [41] as a function of the multipole moment ℓ is shown in figure 1.7(b). From this spectrum one can derive constraints on various cosmological parameters, such as neutrino masses. The free streaming of neutrinos before the decoupling of matter and radiation washed out structures on small scales, which has an impact on the power spectrum. In 2013 the Planck collaboration set an upper limit on the sum of the neutrino masses [41]:

$$\sum_i m_i \leq 0.23 \text{ eV} \quad (1.27)$$

2. KATRIN Experiment

The Karlsruhe TRitium Neutrino experiment aims to determine the effective mass of the electron anti-neutrino with a sensitivity of $200 \text{ meV}/c^2$ (90% C.L.) [27]. The kinematics of tritium β -decay is analysed with a MAC-E-filter, whose functionality is well-proven by previous neutrino experiments in Mainz [42, 43] and Troitsk [44, 45]. This chapter describes the measurement principle and gives an overview of the experimental setup.

2.1. Measurement Principle

Tritium decays into helium via β -decay. The released energy of 18.6 keV is split between the emitted electron and the electron antineutrino. A small fraction also goes into nuclear recoil. Thus the β -particles show a continuous energy spectrum and its shape depends on the rest masses of e^- and $\bar{\nu}_e$.



Figure 2.1 shows the theoretical spectrum for two different neutrino mass scenarios ($0 \text{ eV}/c^2$ and $1 \text{ eV}/c^2$). With the Fermi theory one can derive a formula for the energy spectrum [46]:

$$\frac{dN}{dE} = \frac{G_F^2}{2\pi^3} \cos^2(\Theta_C) |M|^2 F(Z, E) p(E + m_e c^2) (E_0 - E) \sqrt{(E_0 - E)^2 - m_{\bar{\nu}_e}^2 c^4} \quad (2.2)$$

- $m_{\bar{\nu}_e}$: electron antineutrino mass
- E : Electron energy
- E_0 : Electron endpoint energy for $m_{\bar{\nu}_e}=0$
- p : momentum of the electron
- G_F : Fermi coupling constant
- Θ_C : Cabibbo angle
- M : Nuclear matrix element
- m_e : Electron mass
- $F(Z, E)$: Fermi function

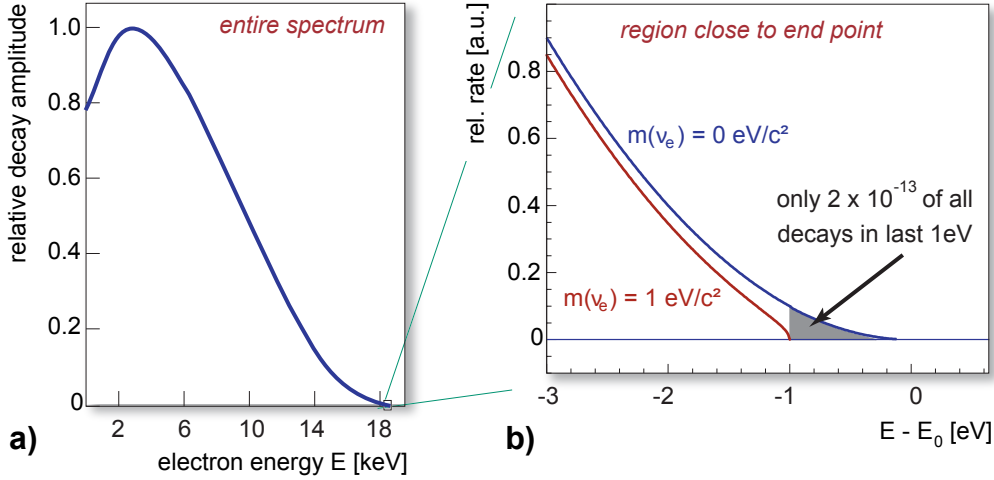


Figure 2.1.: Full tritium spectrum (a) and spectrum in the region close to the endpoint (b). [47]

As equation 2.2 shows, the effect on the spectrum shape is significant for energies close to the endpoint energy E_0 . Therefore, measuring the tritium β -spectrum in this region provides information about the effective electron antineutrino mass, which is the incoherent sum of the mass eigenvalues (see. chapter 1.5.1). Tritium is chosen because of its low endpoint of about 18.6 keV and the high specific activity of 3.6×10^{14} Bq/g, which allows to build a source with high luminosity and a relatively large count rate close to the tritium endpoint. Its low endpoint energy reduces the technical complexity of the experiment, since a relative low retarding potential is needed for the energy analysis.

2.2. MAC-E Filter

In the experimental setup (see 2.3) there are two electrostatic spectrometers both based on the MAC-E-Filter¹ principle [48][49][50]. Superconducting solenoids create a strong guiding field, which leads the electrons adiabatically along the field lines through the spectrometer towards the detector moving on spiral trajectories. The magnetic field drops from B_s at the entrance to its minimum B_{min} in the center of the spectrometer and increases again to its maximum B_{max} at the exit on the detector side. The total electron energy can be split in a longitudinal and a transversal component with respect to the magnetic field direction:

$$E_{tot}^{kin} = E_{\parallel} + E_{\perp} \quad (2.3)$$

As the electrons are emitted isotropically at the tritium source, for the majority of the electrons the fraction E_{\perp} of E_{tot}^{kin} is large. For sufficient count rates, the setup should have a high angular acceptance using a high fraction of the source electrons. The magnetic field in a MAC-E filter changes slowly, therefore the electrons move adiabatically through the spectrometer. For adiabatic electron motion the magnetic moment μ is constant.

$$\mu \approx \frac{E_{\perp}}{|\vec{B}|} \quad (2.4)$$

Equation 2.4 indicates that a reduction of the magnetic field leads to a reduced transversal energy and consequently to increased longitudinal energy due to energy conservation. Transversal energy is transformed in longitudinal energy while the electrons move from the entrance to the middle of the spectrometer. On their path from the middle to the

¹Magnetic Adiabatic Collimation combined with Electrostatic Filter

exit, the process is reversed as the magnetic field increases again. An electrode system on a variable high voltage U_0 creates a retarding potential. Particles with enough energy pass the potential barrier and their momentum is restored as they move to the end of the spectrometer. Electrons with insufficient longitudinal energy in the analysing plane are reflected. This constitutes an electrostatic high pass filter.

Because of technical limitations a vanishing magnetic field in the analysing plane is not realisable. The consequence is a not analysable remaining transversal energy component and associated a finite energy resolution ΔE . Using equation 2.4 one can derive an expression for the energy resolution, which is defined as the maximum possible remaining transversal energy component in the analysing plane. For the energy resolution of KATRIN, with electron energies close to the tritium endpoint E_0 of 18.6 keV this leads to:

$$\Delta E = E_0 \frac{B_{\min}}{B_{\max}} = 0.93 \text{ eV} \quad (2.5)$$

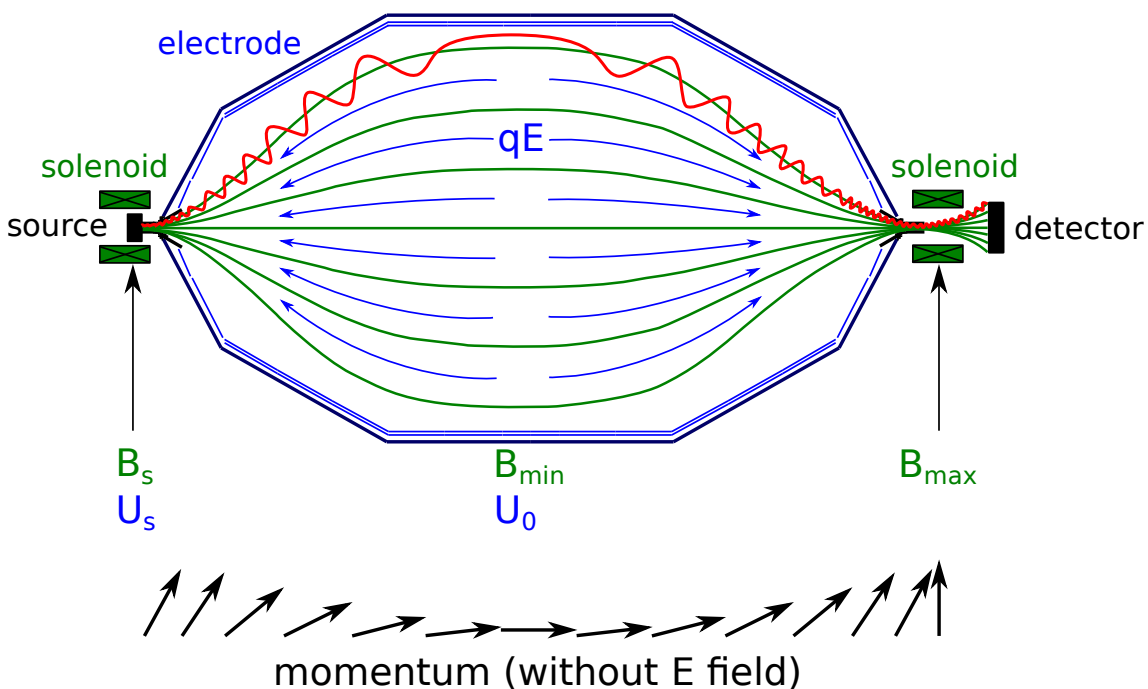


Figure 2.2.: Schematic profile of a MAC-E-Filter: A magnetic guiding field produced by superconducting solenoids leads the electrons through the spectrometer. The magnetic gradient transforms longitudinal energy in transversal energy. The spectrometer tank is set on negative high voltage filtering out electrons that have not sufficient energy to pass the retarding potential.[51]

2.3. Experimental Setup

KATRIN is an experiment with several main components (see a-g figure 2.3). The electrons, produced at the tritium source (see. 2.3 b), need to be transported to the main spectrometer. Electrons are transported in a flux tube of 191 Tcm^2 through the whole experiment. On the transport one has to avoid any energy loss of the signal electrons as this directly influence the measured neutrino mass. For avoidance of background, tritium molecules must not enter into the main spectrometer.

In the pre-spectrometer the uninteresting part of the β -spectrum below 18.4 keV can be filtered out while electrons above this threshold keep their energy for further analysis. The

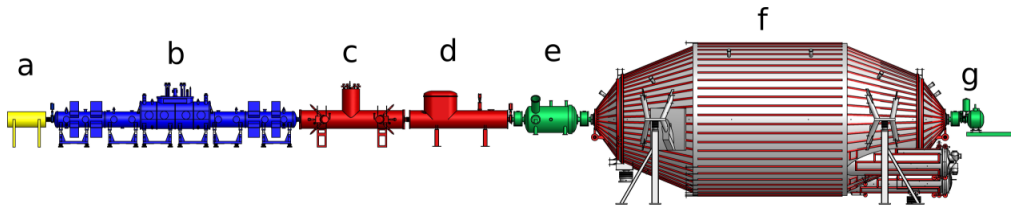


Figure 2.3.: Setup of the KATRIN experiment with rear section (a), WGTS (b), differential pumping section (c), cryogenic pumping section (d), pre-spectrometer (e), main spectrometer (f) and focal plane detector system (g).[47]

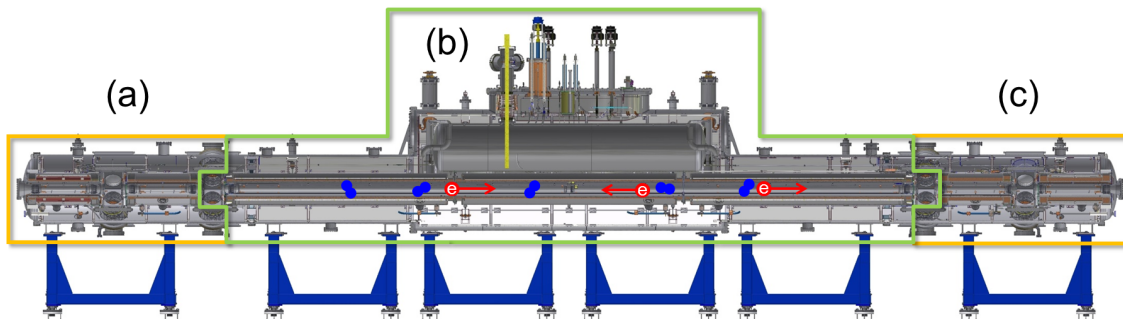


Figure 2.4.: Windowless gaseous tritium source: Tritium is injected in the middle of the beam tube (b) and pumped out at the ends (a+c).[51]

part in the endpoint region, which is sensitive to the neutrino-mass, is analysed with the connected main spectrometer and the detector system at the downstream end of the beam line. A third spectrometer, the monitor spectrometer, is essential for monitoring of high voltage fluctuations of the main spectrometer.

2.3.1. WGTS and Rear Section

The windowless gaseous molecular tritium source (WGTS) [52] produces β -electrons with a tritium activity of more than 10^{11} Bq. A source with high activity is essential, as only one of 10^{13} tritium decays produces electrons in the end point region.

In the source a column density of 5×10^{17} T_2 / cm^2 is created. The column density needs to be stable at $\pm 0.1\%$ in order to keep the systematic uncertainties of the source on an acceptable level. The column density is influenced by various parameters like tritium purity, pumping speed of the turbo molecular pumps, temperature or the injection pressure. Thus there are strict requirements for the stability of these parameters. One has to keep the source at a constant temperature below 30 K ($\Delta T < 30$ mK). This will be achieved with a two phase neon cooling system [53]. At the middle of the WGTS, gaseous molecular tritium is injected. The T_2 -molecules diffuse to the ends of the tube where they are pumped out by turbo molecular pumps, led back and re-injected at the center forming a closed cycle. Superconducting solenoids generate a magnetic field that guides one half of the produced electrons to the spectrometer section for energy analysis and the other half directly into the rear section for rate monitoring via Beta-Induced X-Ray Spectroscopy [54]. Most of the electrons that enter the spectrometer section are reflected there and finally also reach the rear section.

2.3.2. Transport Section

The transport section has the task to guide the signal electrons from the source to the spectrometer section and to remove tritium from the beam line. It consists of an active and

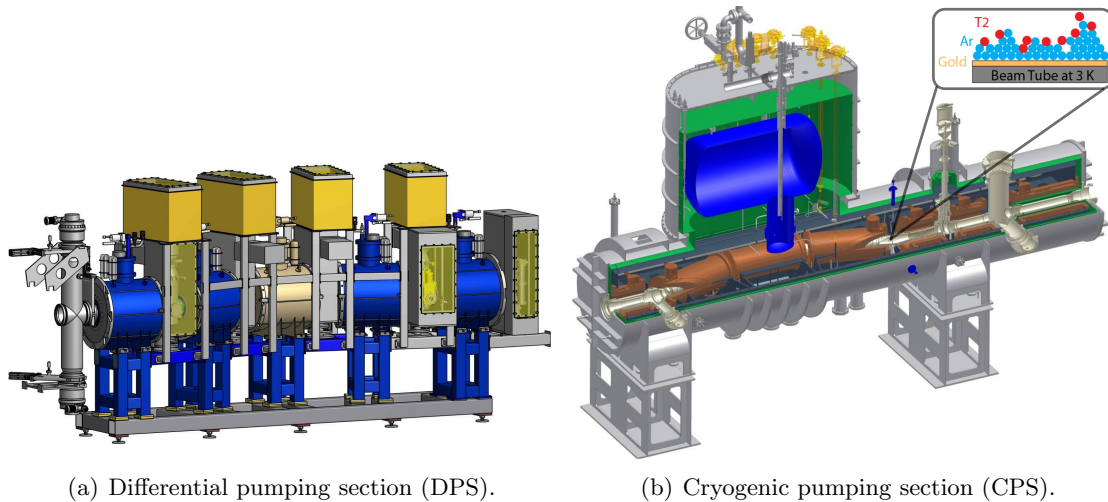


Figure 2.5.: Modules of transport section. DPS: Superconducting solenoids guide the electrons through chicanes. Tritium is pumped out by 4 turbo molecular pumps. CPS: Electrons are guided through the chicanes while tritium molecules are bound when they hit the cold surface. This reduces the tritium partial pressure by 14 orders.

a passive part and has to decrease the tritium partial pressure by 14 orders of magnitude, to keep the background due to tritium decays in the main spectrometer below the design limit [55]. To keep the tritium background below the Katrin design limit a tritium partial pressure of less than 10^{-20} mbar is required. In the differential pumping section (DPS) a pressure reduction is achieved using turbo molecular pumps that can resist the strong radiation and operate in high magnetic fields. The pumped tritium then is reused in the tritium cycle. Further, in the cryogenic pumping section (CPS) tritium molecules are frozen on ultra-cold surfaces which additionally decreases the tritium partial pressure. In both modules the β -electrons are guided through chicanes which avoid the molecular beaming effect as there is no direct line-of-sight.

2.3.3. Pre-Spectrometer

The pre-spectrometer based on the MAC-E-Filter principle is directly connected to the transport section and serves as a pre-filter for electrons below 18.4 keV. The energy of transmitted signal electrons is fully restored by the time they reach the main spectrometer. Two superconducting solenoids create a strong magnetic guiding field (up to 4.5 T). The pre spectrometer is equipped with NEG pumps which can pump tritium. This serves as additional buffer to avoid that tritium molecules reach the sensitive area within the main spectrometer. Until 2011 it has been used for extensive background studies [47].

2.3.4. Main Spectrometer

After passing the pre-spectrometer the remaining electrons enter the large main spectrometer (length 24 m, diameter 10 m, volume 1250 m^3) where the end-point region of the tritium β -spectrum is measured with very high precision. In order to reach this high accuracy an ultra high vacuum of at least 10^{-11} mbar is required, since signal electrons could ionise residual gas molecules on their path to the detector and thus increase the background rate. In addition, any loss of signal electron energy has an impact on the measured tritium spectrum. The vacuum is achieved with 6 turbo molecular pumps and about 3000 m of non-evaporable getter strips in the three pump ports. The magnetic guiding field is created

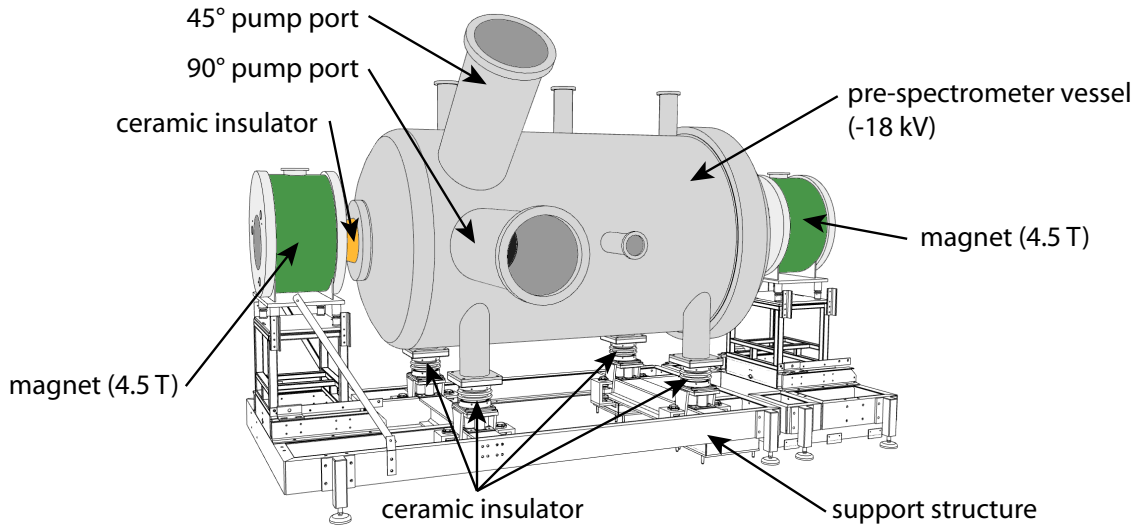


Figure 2.6.: Pre-spectrometer: Two superconducting solenoids create a magnetic guiding field. The electrostatic retarding potential filters out the low-energetic part of the spectrum. Figure from [47]

by the 2 pre-spectrometer solenoids (4.5 T) together with a pinch (6.0 T) and a detector magnet (4.5 T) integrated in the detector system at the exit of the main spectrometer. Furthermore, there is a system of large air coils surrounding the vessel, which allows to fine-tune the shape of the magnetic flux tube within the spectrometer and to compensate the Earth's magnetic field to generate an axial symmetric field within the spectrometer. The retarding potential is generated by setting the tank itself on high voltage. A double layer inner wire electrode system keeps out secondary electrons from the vessel surface induced by cosmic muons or gamma radiation by electrostatic retardation. As the retarding potential needs to be very stable, precise high voltage monitoring is indispensable. This is achieved by the monitor spectrometer with a high precision voltage divider.

2.3.5. Monitor Spectrometer

The spectrometer of the precedent experiment in Mainz is used as a monitor spectrometer. It is connected to main spectrometer and hence can monitor the high voltage stability via continuous measuring transmission functions of a krypton source ($^{83\text{m}}\text{Kr}/\text{K}32$ line) with a very high energy stability. [56].

2.3.6. Focal Plane Detector System

The number of electrons transmitted through the spectrometer section are counted with a focal plane detector at the downstream end of the beam line [57]. The detector consists of a silicon Positive Intrinsic Negative diode (90 mm diameter) divided in 148 pixels of equal area. The detector system contains a pinch and a detector magnet forming the magnetic field inside the main spectrometer. Furthermore, the pinch magnet generates the largest magnetic field (6.0 T) along the beam line and thus, together with B_s (3.6 T), setting the maximum accepted angle of 51° with respect to the magnetic field lines. Electrons which are emitted at the source with larger angles are reflected. This is necessary, because larger angle means more cyclotron motion and consequently higher probability of interaction with residual gas due to the longer path length. The segmentation is necessary due to slight inhomogeneities of magnetic and electric field in the analysing plane. Each pixel has the same area, simplifying the comparison of the rates. Careful selection of materials, lead and copper shielding, as well as a muon veto ensure a low background level. A post acceleration

electrode shifts the signal electron energies up to a higher energy region (+10 keV) with better signal to background ratio.

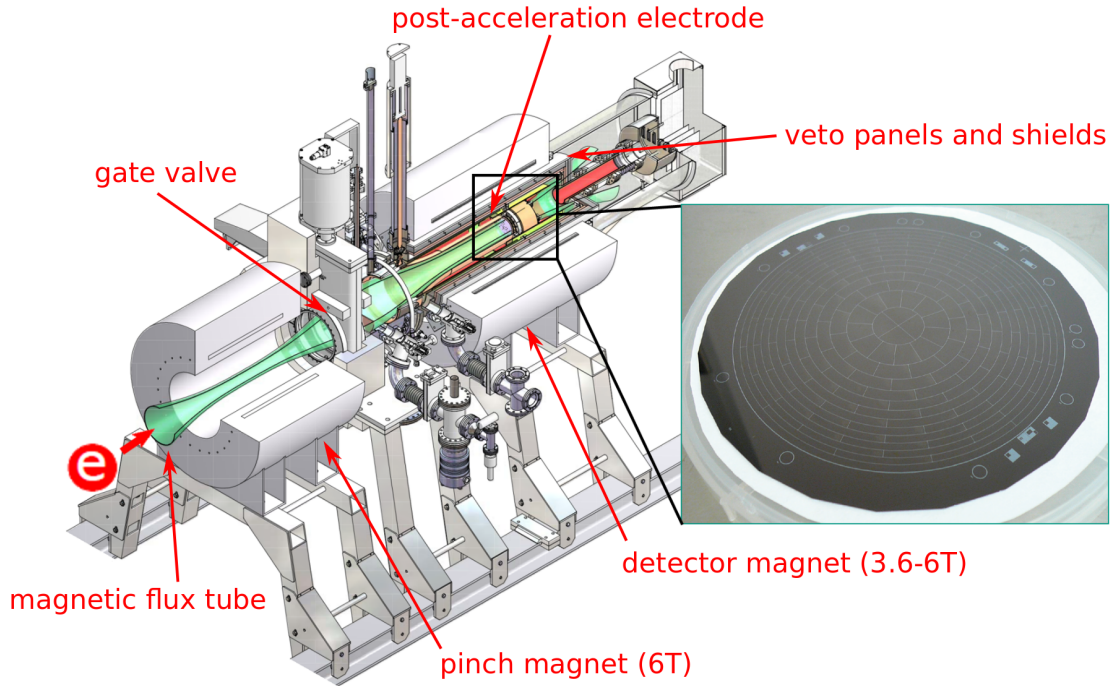


Figure 2.7.: Overview of the focal plane detector system and the segmented silicon PIN diode. [51]

2.4. Background Sources

In order to reach the KATRIN design sensitivity of $200 \text{ meV}/c^2$, the overall background needs to be on the order of 0.01 cps. A detailed understanding of the background processes is essential to reach this goal. To ensure this low background level various commissioning measurements for background studies were performed in the past and will be done in the future. The expected major background sources are magnetically stored particles and muon induced secondary electrons from the vessel wall. These two processes are described in more detail below.

2.4.1. Secondary Electrons from Surfaces

The whole experimental setup is exposed to a permanent flow of cosmic muons (about $189/\text{sm}^2$). Muons or γ 's from natural radioactivity hitting the spectrometer tank can produce secondary electrons. To shield the flux tube from these electrons, there is a two layer inner wire electrode system on a more negative potential than the vessel wall which reflects electrons (electric shielding) up to an energy of $e\Delta U$ back to the surface where ΔU is the potential difference between wire electrode and the vessel. In addition, the symmetric magnetic field reflects electrons coming from outside the flux tube (magnetic shielding). For exact axial symmetric fields only particles generated inside the flux tube were guided to the detector. As small inhomogeneities are not avoidable, the shielding is not perfect. Electrons from outside the flux tube are able to radially drift into the sensitive volume and could eventually reach the detector. This process can take up to $40 \mu\text{s}$. A detailed explanation can be found in [58]. Measurements and simulations concerning muon induced background are the main topics of this thesis.

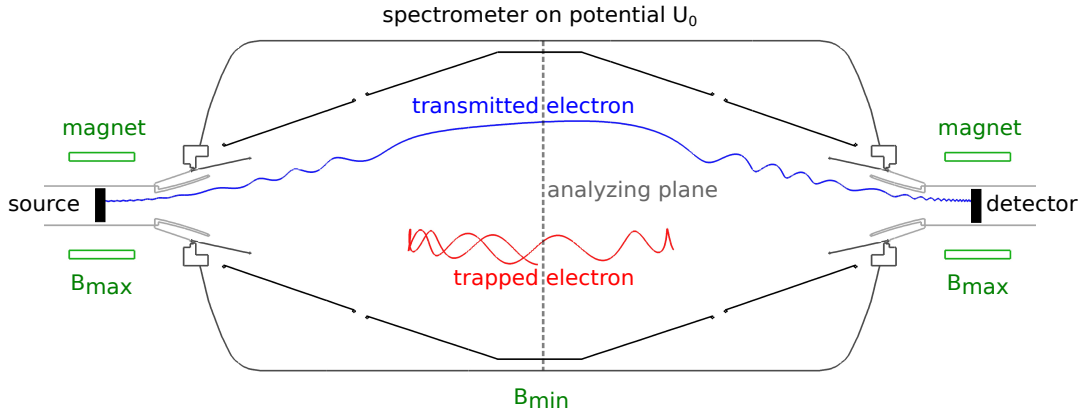


Figure 2.8.: Schematic view of a transmitted electron and a trapped electron due to the magnetic mirror effect in the main spectrometer.

2.4.2. Magnetically Stored Particles

Using a MAC-E-Filter for the energy analysis has the big disadvantage that such a filter acts as a very good magnetic bottle [59]. This means charged particles created by nuclear decays inside the spectrometer volume can be stored there for very long times (up to hours at UHV conditions) and create a large number of secondary electrons via ionisation of the residual gas molecules [60]. The secondaries are accelerated by the electric potential and therefore will have the same energy as the signal electrons from β -decays by the time they arrive at the detector. The major origin of high energetic electrons produced within the main spectrometer is the decay of radon atoms. Radon emanates from the getter material of the NEG² pumps and the vessel surface. The isotopes ^{219}Rn and ^{220}Rn have short half lifes ($\tau_{1/2}^{219} \sim 4\text{s}$, $\tau_{1/2}^{220} \sim 56\text{s}$) and thus they decay before they are pumped out and emit α -particles. In this process high energetic shake-off, conversion- and Auger electrons are emitted. Another contribution comes from tritium atoms. Although the vast majority of the tritium atoms are pumped out before they reach the main spectrometer and most of the remaining tritium there is bond by NEG pumps, a small fraction decays inside the spectrometer producing high energetic electrons.

To minimize the number of radon atoms, effective counter measures are required. Nitrogen cooled baffles are installed between the spectrometer volume and the pump ports where the getter pumps are located [61]. The emanating radon atoms stick on the cold baffle surface. This solution ensures high radon background reduction with adequate pumping speed for hydrogen as the dominant residual gas. However, radon emanating from the inner vessel surface is only partially suppressed by this method. Therefore additional active background reduction methods are investigated e.g. magnetic pulse, electric dipole [51] or electron cyclotron resonance [62].

²Non evaporable getter

3. Muon Detection System

To achieve the required low total background level of about 0.01 cps, detailed studies of all background contributions are essential. One major background component is expected to be caused by muon induced secondary electrons from the vessel wall (see chapter 2.4.1). The magnetic field and the inner wire electrode system inside the main spectrometer shield the sensitive volume of the flux tube from surface electrons, but the shielding is not perfect. Electrons which are produced at the innermost wire layer are not electrostatically shielded. In addition, magnetic materials near the spectrometer can cause small inhomogeneities of the magnetic field. This allows a radial drift of the electrons that can possibly reach the focal plane detector. Therefore, investigation of the muon induced background component are indispensable. For this purpose, a set of eight large muon detectors is positioned close to the main spectrometer each with a sensitive area of 2.05 m^2 . The module positions are illustrated in figure 3.3. This allows to search for potential correlations between muons crossing the tank volume and detector counts, and thus to investigate the influence of cosmics on the background rate. Such correlations were already found with two smaller muon modules ($A \approx 0.3 \text{ m}^2$) at the monitor spectrometer [58]. Most of the incident muons have small polar angles, which means they incide mainly vertical. If one aims to measure coincidences between two modules on opposing sides of the spectrometer it is useful to have a muon module on top of the main spectrometer. Within the frame of this thesis, one of the small modules, previously used at the monitor spectrometer, was mounted on a movable platform above the spectrometer. This allows to take advantage of an enhanced relative position with respect to the large modules on the ground and to measure coincidences with small polar angle. A more detailed motivation is given in section 4.1. Test measurements (see chapter 4) were performed to check the practicability of the extended system and to determine the coincidence rates between the muon modules. In the following "small module" always denotes the module mounted on top of the spectrometer. The modules on the ground are refered to as "large modules".

3.1. Scintillator Modules

The modules are made of synthetic BC-412 plastic scintillator. Muons crossing the module excite molecules in the material, which lose the absorbed energy by emitting photons. The photons are detected with multiple photomultiplier tubes (PMT¹) per module. To increase the detection efficiency, the modules are cased with reflective foil and wrapped

¹Type: 2-inch Philips Valvo XP 2262/PA

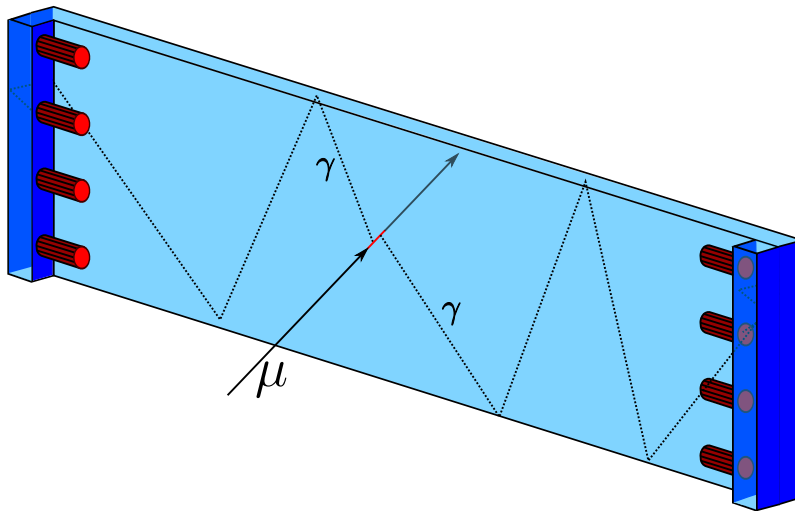


Figure 3.1.: Schematic view of a muon scintillator module with 4 photo multiplier tubes at two short edges each [51].

by light tight foil to inhibit that ambient light is detected. The eight large modules ($3.15 \text{ m} \times 0.65 \text{ m} \times 0.05 \text{ m}$, sensitive area: 2.05 m^2) have four PMTs at the two short edges (see figure 3.1), the smaller modules with a sensitive area of about $\sim 0.3 \text{ m}^2$ two PMTs, each placed side by side on the short edge (see. figure 3.5(a)). The small panels are placed inside wooden boxes. The modules are connected to a DAQ-system via coaxial cables for event recording.

3.2. Photomultipliers

Photomultipliers can be used to detect feeble photon signals exploiting the photo-effect and secondary emission in a vacuum environment. The photons hit a photo-cathode where they produce secondary electrons. The electrons have a maximum kinetic energy of

$$E_{\text{max}}^{\text{kin}} = \nu h - W \quad (3.1)$$

with the frequency of the incident photon ν , the Planck constant h and W , the energy required to detach the electron from the surface. A set of various cascaded dynodes is used to multiply the number of electrons, which leads to a detectable signal. The secondaries are guided from dynode to dynode and accelerated by a voltage of 100 V-200 V generating more electrons via secondary emission each time. Magnetic fields can influence the movement of the electrons in the PMT and so reduce the detection efficiency. As the PMTs need to operate in high magnetic fields near the LFCS² they are shielded by wrapping them in permalloy. The PMTs of the modules are powered by two CAEN SY-127 high voltage supplies with about 1.5 kV.

3.3. Module Positions

The eight large muon modules are placed on three movable trolleys in sets of three or two panels at different positions close to the main spectrometer. For an optimum coverage of the tank surface, they are located very close to the LFCS². The specific positions and the definition of module numbers are shown in figure 3.3. For the first measurement phase (SDS1) only these eight modules were operated at the main spectrometer. Within the

²Low Field Coil System



Figure 3.2.: Modules 6-8 on the east side trolley and DAQ-system. For definition of module numbers see figure 3.3. Picture taken from [63]

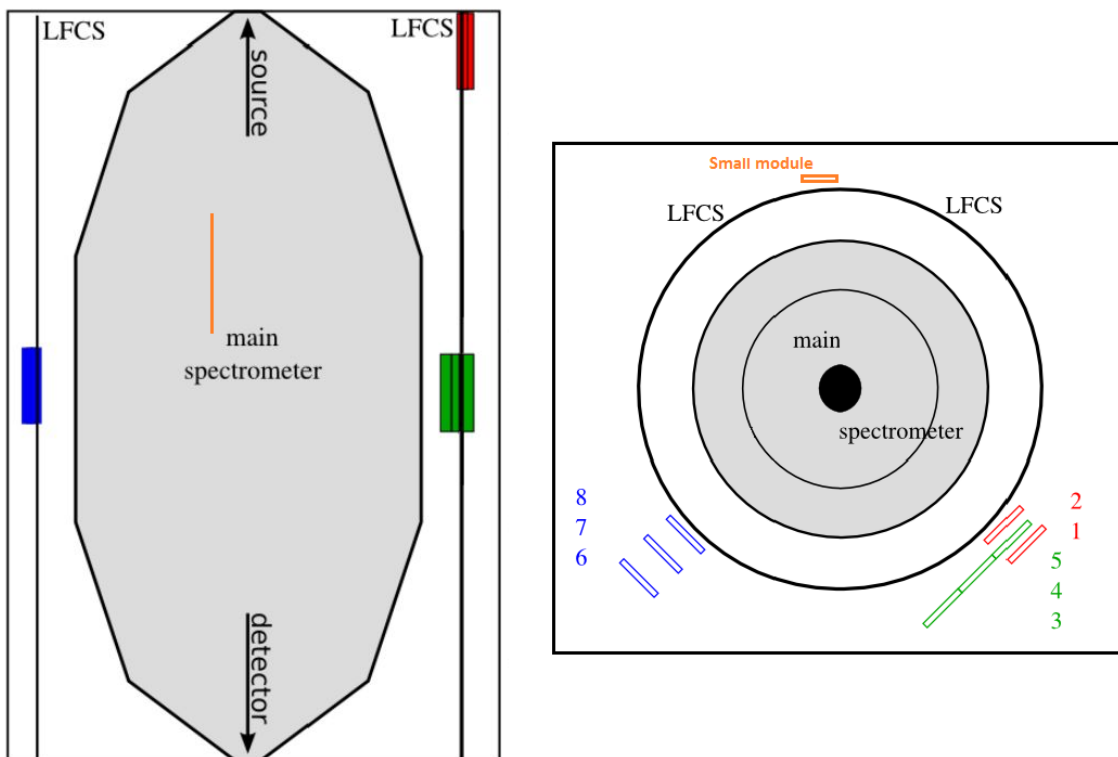


Figure 3.3.: Positioning of the large muon modules on the ground close to the main spectrometer and the small module mounted above the spectrometer. The small module was shifted on the orange line in the left plot. Figure not true to scale. Taken from [63](edited)

Module	1A	1B	2A	2B	3A	3B	4A	4B
Card	3	3	3	3	6	6	6	6
Channel	0	14	3	7	0	14	3	7
HV[kV]	1.55	1.55	1.50	1.60	1.50	1.50	1.50	1.50
Module	5A	5B	6A	6B	7A	7B	8A	8B
Card	6	6	9	9	9	9	9	9
Channel	9	23	0	14	3	7	9	23
HV[kV]	1.50	1.50	1.60	1.50	1.50	1.50	1.50	1.50

Table 3.1.: Assignment of muon modules to FLT-cards, channels and high voltage

frame of this thesis one of the small modules was mounted almost on the beam axis ca. 1.5 m above the main spectrometer to realise an enhanced muon detection system. The module was connected with the muon DAQ and a HV supply, which was temporary fixed at the handrail at the east side of the main spectrometer. With this additional module higher coincidence rates are expected as coincidence events of muons with small polar angle can be measured. Furthermore, due to the geometrical assembly and the small area of the module above the spectrometer, the area on the tank wall wherefrom secondary electrons are emitted can be reconstructed with higher resolution, which offers further measurement options. Test measurements and respective simulations are described in chapter 4 and 5.

3.4. DAQ System

An IPE-Crate Mark IV with 20 FLT slots is used for the data acquisition. Four FLT cards at the slots 3,6,9 and 18 are used. The card at slot 18 was temporary used to read out the small module. The FLT cards have a coincidence-filter implemented. The modules are connected via coaxial cables to the FLT cards and read out via two FLT-channels each. The large modules feature one channel per side meaning that four PMTs belong to one channel. The two PMTs of the small panels are read out with individual channels (Channels 1 and 7 of FLT card at slot 18). The cables all have the same length of ≈ 30 m as precise timing is required for coincidence measurements and differing cable lengths produce deviant signal delay. To synchronise detector and muon DAQ, a high precision clock is connected to both of them. To reduce low energy background, only events where a signal on both channels of a module is found are considered and passed to the second level trigger (SLT) card. The DAQ-system is controlled with the ORCA software³ [64] running on a PC, which is located beneath the panels 6-8 (see figure 3.2) as well as the DAQ. A muon run is labeled by "myo" followed by a number consisting of 8 figures.

Incident muons generate a signal pulse in the PMTs while hitting a muon module. A typical time trace of such a pulse measured with an oscilloscope is shown in figure 3.4(a). As the pulse has a finite length and precise timing is required for coincidence searches, the determination of the time that is assigned to a muon event is not trivial. The signal filtering is a two level process. A Boxcar filter is applied to the time trace which computes an floating average $BC(t)$ in a certain time window t_{BC} . When this floating average exceeds a defined threshold the next level filter, a so called trapezoidal-filter with a shaping length t_T , is "triggered", whose value at the time t is defined as follows:

$$T(t) = \int_{t-\frac{t_T}{2}}^t BC(t') dt' - \int_t^{t+\frac{t_T}{2}} BC(t') dt' \quad (3.2)$$

³Object-oriented Real-time Control and Acquisition

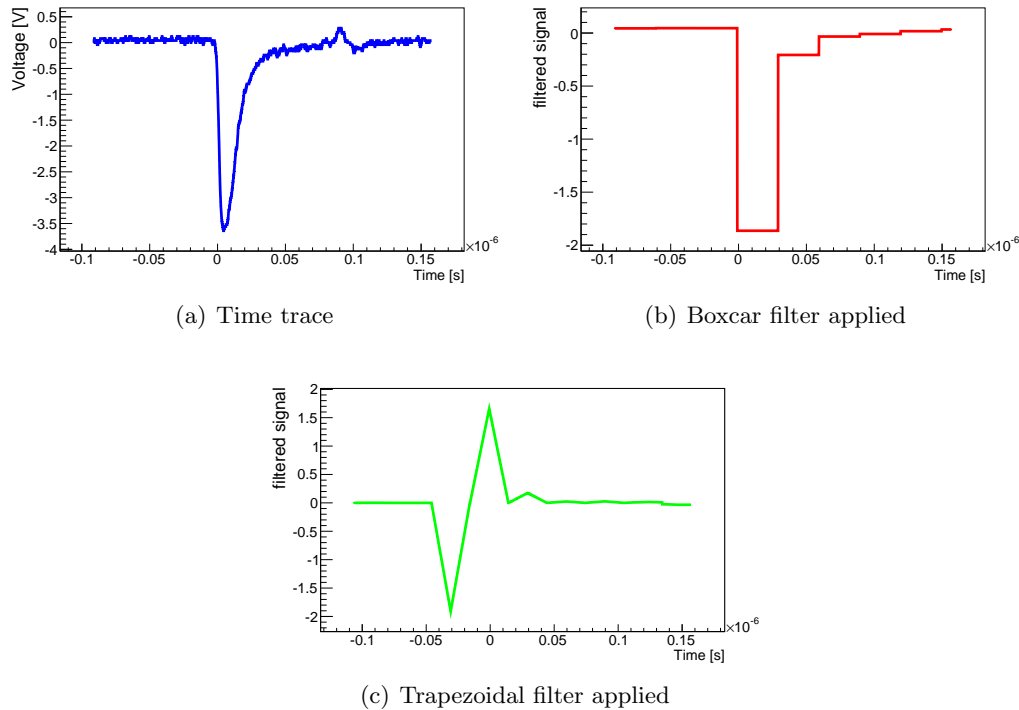


Figure 3.4.: Illustration of the filtering process in the DAQ-system

The shape of this expression has a zero transition between the two peaks as shown in figure 3.4(c). The time of a muon event is then defined as the time of the zero transition plus $3/2$ times the shaping length t_T .

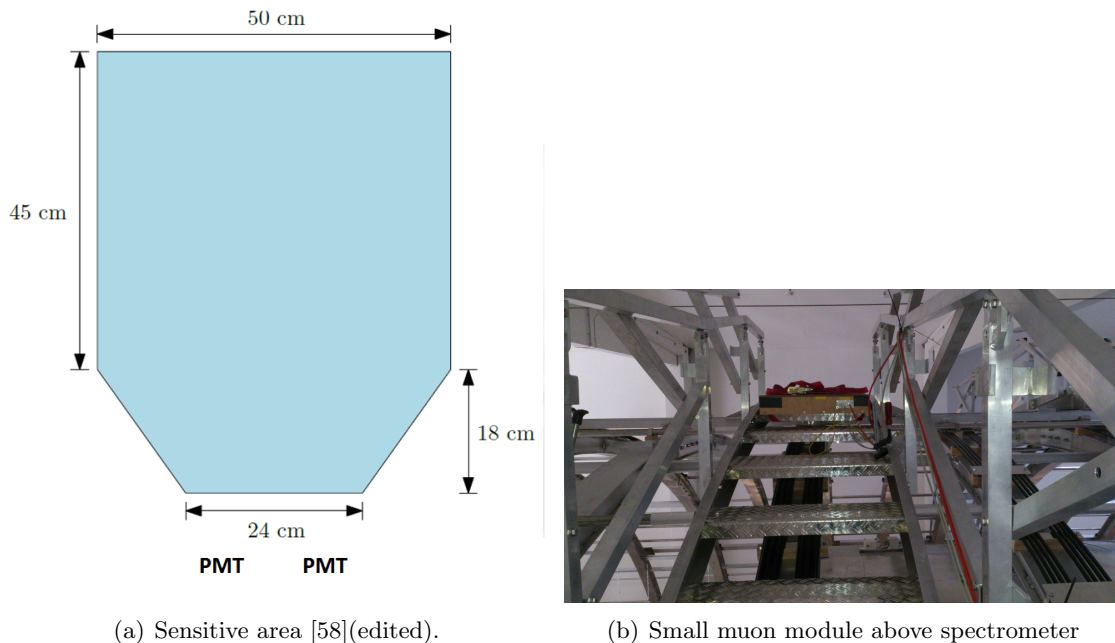
3.5. Muon Panel Operational Parameters and Performance

The energy loss of muons in a scintillator follows a landau distribution. One has to fine tune the acceleration voltages of the PMTs in order to optimise the detection efficiency and minimise noise. As the modules were turned off for a longer time, the voltages were optimised again after reactivation. Also the stability of the ADC value of the MPV⁴ of the landau distribution has to be investigated as the voltages might drift over time, which would directly affect the detection efficiency. Within a long term measurement over three months the stability was sufficient for all large modules. The long term measurement is described in chapter 6 in detail.

3.5.1. Large Modules

The ADC histograms should have a shape similar to figure 3.7(b). For all channels, except one, it was possible to set the voltages to obtain appropriate ADC histograms and the expected count rates. The respective FLT-cards, channels and applied high voltage for each channel are shown in table 3.1. Figure 3.7(a) shows the ADC histogram for channel B of module 2. On the left hand side of the peak the rise is much too steep and thus compared to figure 3.7(b) the low energetic part of the spectrum is missing. Possibly one of the PMTs is not working correctly. As the behaviour of this channel is not understood, module 2 was excluded from all analyses and simulations. Assuming linear and undisturbed moving cosmic muons with a mean flux of about $189/\text{m}^2\text{s}$, the expected count rate for each module is ~ 256 cps taking into account their sensitive area of 2.05m^2 and an angle

⁴Most Probable Value



(a) Sensitive area [58](edited).

(b) Small muon module above spectrometer

Figure 3.5.: Small muon module mounted on a movable platform above the main spectrometer.

of 45 degree with respect to the horizontal plane. The muon rate on the ground varies by a few % over months (see chapter 6) since it is influenced by temperature, pressure and the atmospheric density [65]. Figure 3.6 shows the rate of module 1 with a mean rate of a 256.50 ± 0.06 cps. This matches the expected value. All remaining modules show comparable count rates (see Appendix C), some with slight deviations.

3.5.2. Small Module

The acceleration voltage of the photomultipliers was optimised and set to 1.6 kV. The adc histogram is shown in figure 3.9. A clear Landau peak is visible.

The module has a sensitive area of 0.3 m^2 . With an average cosmic muon flux of about $189 / \text{m}^2 \text{ s}$ a rate of ~ 55 cps is expected. Figure 3.8 shows the detected muon rate over 20 hours with a comparable mean value of 59.60 ± 0.03 cps. The measurements show that the small muon module and seven of the eight large modules work properly and can be used for coincidence measurements.

The muon detection system can not serve as a muon veto. Two facts inhibit to build a veto system for the whole volume of the spectrometer. First, even for a system that would completely enclose the whole spectrometer its inevitable inefficiency combined with the high total cosmic ray exposure of roughly 37500 cps [66] would lead to high uncertainties. Second, even for negligible inefficiency of a veto system, the time between a muon hit at the surface and the potential detector hit varies over a range of $40 \mu\text{s}$, as the background generation process is pretty complicated and requires some steps between secondary electron emission from the wall and incident background electron at the detector. So the time window, which had to be excluded, was much to large taking into account the high muon rate.

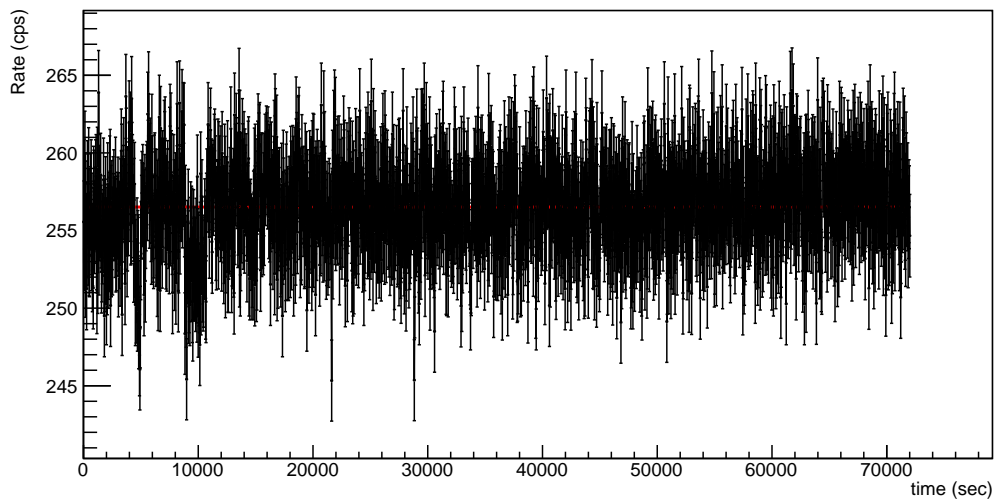
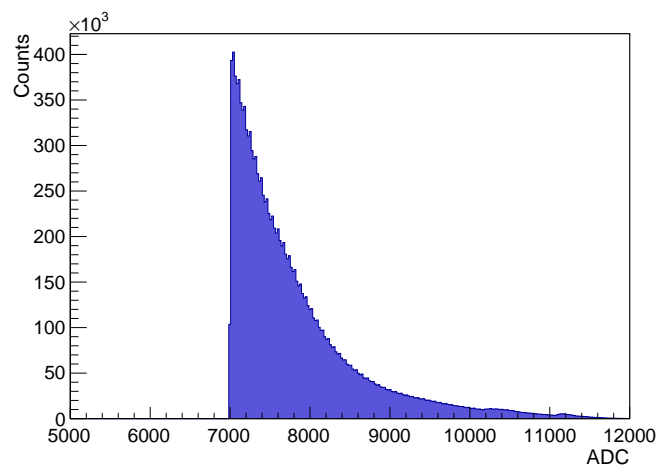
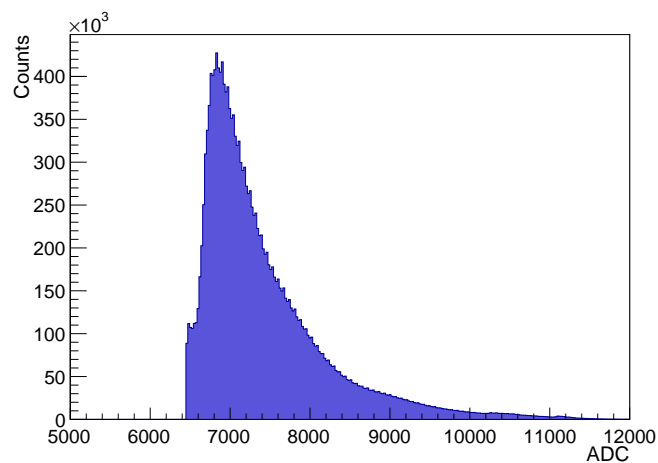


Figure 3.6.: Muon rate over 20 hours measured with module 1. The mean rate is 256.50 ± 0.06 cps. Runs: myo00001410-1429



(a) Panel 2 Side B



(b) Panel 3 Side B

Figure 3.7.: ADC histograms of two muon channels for an one hour run (myo00001410)

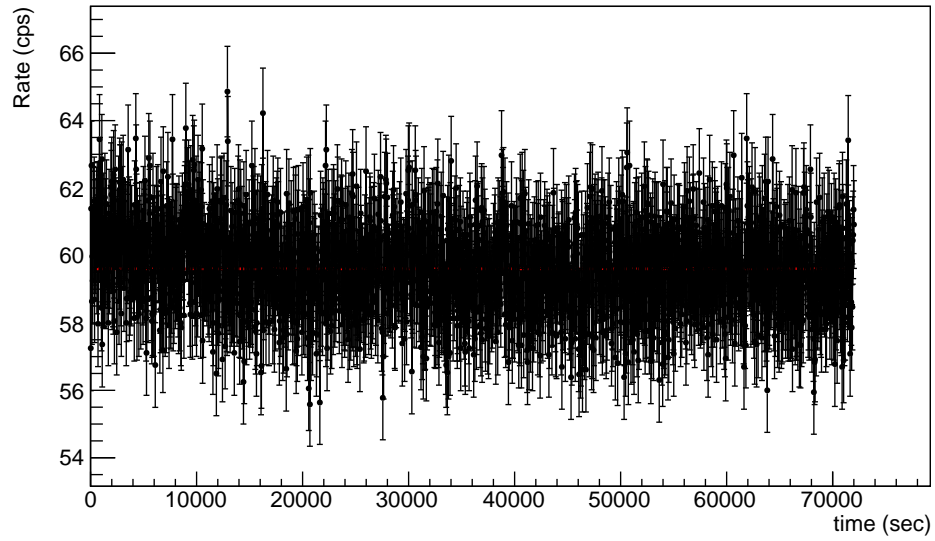


Figure 3.8.: Measured muon rate of the small muon module over 20 hours. The mean rate is 59.60 ± 0.03 cps. Runs myo00001410-1429

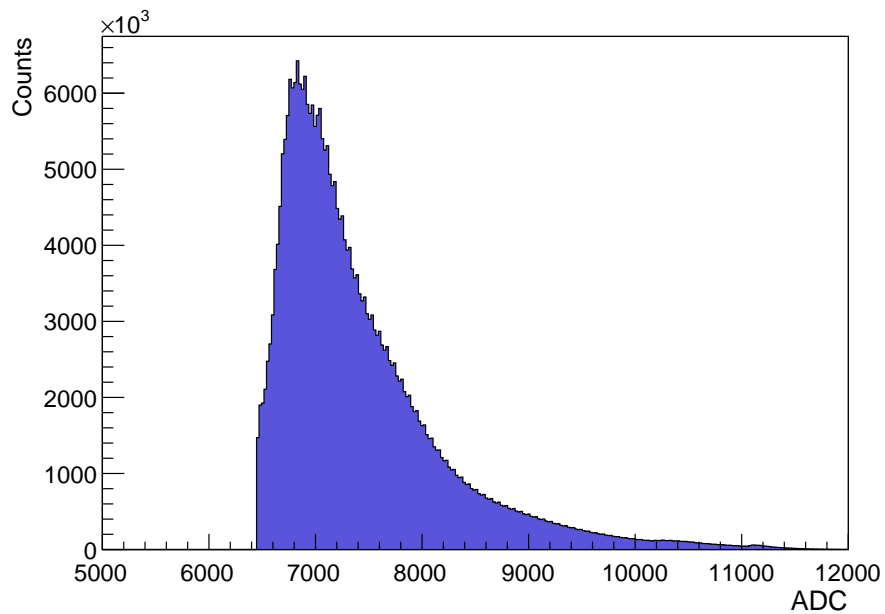


Figure 3.9.: ADC histogram of the small muon panel both channels combined for an 1 hour run (myo00001410).

4. Measurements with an Extended Muon System

Measurements to search for coincidence events between detected muons in the panels and counts of secondary electrons in the focal plane detector, are essential in order to study the mechanism of muon induced background electrons in the KATRIN main spectrometer. For this purpose an asymmetric magnetic field with widened flux tube can be applied within the main spectrometer, which covers large areas of the tank surface. Secondary electrons emitted at the surface are guided from the wall through the main spectrometer. Due to the magnetic mirror effect, most of these electrons are reflected and only a small fraction can be detected at the FPD detector. The muon detection system was extended by an additional module on top of the spectrometer. The undertaken test measurements are described in this chapter.

4.1. Motivation

There are three ways to search for coincident events between muon modules and FPD counts. For each, only events where at least two muon modules were hit can be considered. Then the detected muon necessarily needs to pass the spectrometer volume. This also holds for the 3 stacked modules as they are located close enough to the main spectrometer.

The first way is to look at coincident events in the stacked modules 6-8 at the east side of the spectrometer. The modules are located close to each other and thus a large solid angle is covered. Consequently, this results in high coincidence rates. Due to the large solid angle one can not obtain informations about the area where the muon crossed the spectrometer wall with this method.

Alternatively, one can claim that two modules on opposing sides¹ of the spectrometer were hit. As the distance (>10 m) between them is relative high, in this case the muon can only cross the tank wall in a small region. But the coincidence rates are much lower compared to the first method because only small solid angles are covered. Another fact leads to low coincidence rates. Low energetic cosmic muons decay before they reach the ground. The muon flux strongly decreases for higher polar angles. There are different parametrisations for the polar angle distributions of cosmic muons at sea level. The $\cos^2(\theta)$

¹see figure 3.3 Hits on opposing sides means: Hit in one of the modules on the left side marked in blue and one of the modules on the right side marked in red or green.

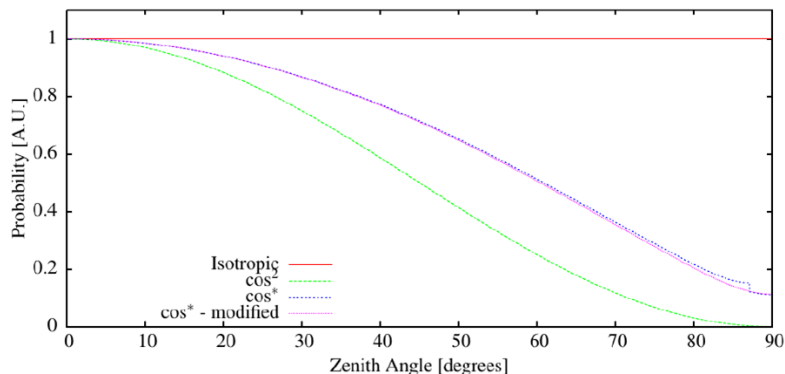


Figure 4.1.: Parametrisations for the angular distribution of the polar angles of cosmic muons.

and $\cos^*(\theta)$ distributions are shown in figure 4.1. The muons fly mainly vertically through the main spectrometer and only very few muons horizontally [67]. In section 5.2 the $\cos^*(\theta)$ distribution is described in detail. Due to this angular dependence of the muon flux, the coincidence rate between the large modules on opposing sides on the ground is small. To achieve a higher coincidence rate it is thus useful to place a module above or below the spectrometer, which allows to measure coincidences of muons with large polar angles. As the weight of the muon modules is too high to place them in the tub under the spectrometer only a module above the tank is an option. A first idea, to mount one of the large modules on a timber at the ceiling of the spectrometer hall, was discarded due to technical limitations. Instead one of the small muon detectors was fixed on the movable ladder on top of the air coils as described in chapter 3. The small area of the small top module over the spectrometer offers another advantage. A muon detected in the small module and one of the large modules on the ground can cross the tank only in a very narrow region and so the crossing point can be reconstructed with higher resolution. Corresponding simulations to determine the crossing points are described in 5.4. With an asymmetric magnetic field applied, one can assign pixels on the detector waver to regions they "see" on the vessel surface and thus search for correlations of muons crossing this region and FPD counts at the corresponding pixels. The undertaken test measurements with this enhanced muon detector setup are described in this chapter. Corresponding simulations and particle tracking from the spectrometer surface through the spectrometer is elucidated in chapter 5. Unless different indicated, in the following "coincidence" denotes a coincident event in at least two muon detectors on opposing sides of the spectrometer and not simultaneous events in muon detectors and focal plane detector. This means events where a muon hits a muon module, then passes the spectrometer volume, and afterwards hits another module on the other side.

4.2. Test Measurement Setup

Test measurements were performed to determine the coincidence rates between the top module and the large modules on the ground. In other words, it is required that the upper module is hit and additionally at least one of the large modules on the ground. The modules were operated as described in chapter 3. The upper module was placed on 5 different positions by shifting the ladder along the spectrometer axis. The specific positions are shown in table 4.1 and illustrated in figure 3.3. The point of origin is in the middle of the main spectrometer and the z-axis points to the entrance on the source side. All positions are ~ 6.5 m above the beam line i.e. ~ 1.5 m on top of the tank and shifted by ~ 0.5 m from the center perpendicular to the beam line to the east.

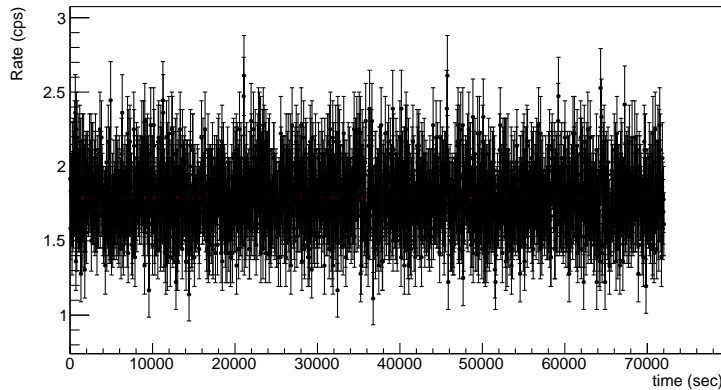


Figure 4.2.: Coincidence rate between the small module at position 1 and any module at the bottom. The mean rate is 1.79 ± 0.01 cps.

4.3. Coincidence Rates

Figure 4.3 shows the coincidence rates between the small module at different positions and any of the large modules on the ground. The rate drops from its maximum at position 1 to its minimum at position 5 along the spectrometer axis. This is plausible since 6 large modules are placed near the middle of the spectrometer where small polar angles between them and the small module are covered. The influence of muon flux variations is neglected. During the measurements the muon flux fluctuated by about 2.5%. The maximum time difference between hits in the two muon detectors is less than 100 ns for coincident events. Therefore, accidental coincidences are very unlikely as the mean time difference between two hits in the large module is about 4 ms and even larger for the small module. The measurements show that with the additional module it is possible to increase

Position	1	2	3	4	5
z[m]	2.1 ± 0.05	3.0 ± 0.05	3.9 ± 0.05	4.8 ± 0.05	5.7 ± 0.05
rate[cps]	1.79 ± 0.01	1.76 ± 0.01	1.61 ± 0.01	1.48 ± 0.01	1.36 ± 0.01
first run	my00001410	my00001485	my00001509	my00001530	my00001554
last run	my00001484	my00001508	my00001529	my00001553	my00001578

Table 4.1.: Coincidence rate between the small module and any module at the bottom for different positions of the small module.

the coincidence rate by almost a factor two compared to the rate between the large modules on the ground. A second small muon module could be used for further improvements.

Figure 4.4 shows the coincidence rate between the large muon detectors on the ground for a measurement time of 20h, not taking into account the top module. The mean rate is 2.19 ± 0.01 cps. As one actually aims to measure coincidences between primary muons and secondary electron FPD counts one also has to take care of the position where detected muons cross the tank. The number of secondary electrons that can reach the detector depends on several parameters. For asymmetric magnetic fields the flux tube should cover the whole area on the surface where muons detected in the muon panels cross the wall. The magnetic field near the electrodes should be maximised in order to minimise the number of secondary electrons reflected by the magnetic mirror effect. Simulations with an asymmetric fields applied are done in section 5.6.

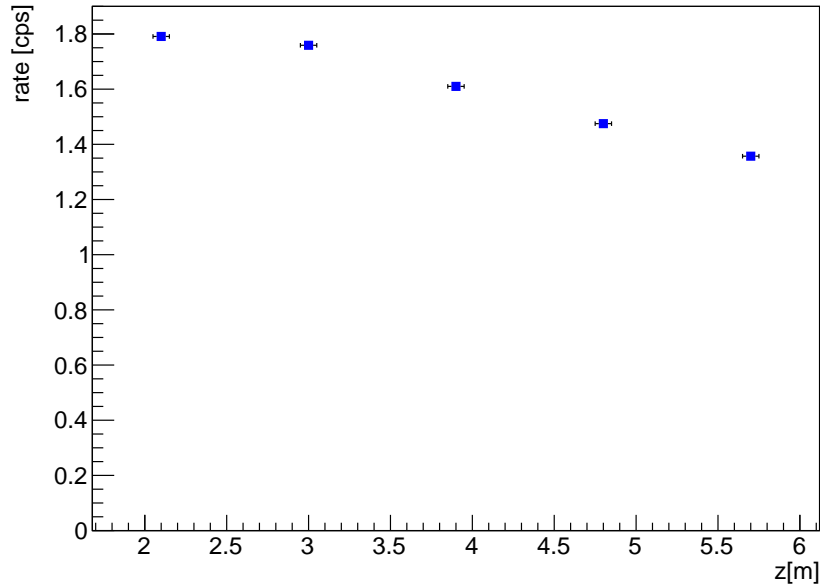


Figure 4.3.: Coincidence rate between the top module and the seven modules on the ground for different positions of the top module. The origin of ordinates is in the center of the spectrometer and the z-axis points upstream. The highest coincidence rate of 1.79 ± 0.01 cps is observed with the top module placed at the position 1 (near the analysing plane of the spectrometer). The systematic uncertainty on the position is estimated to 0.05 m.

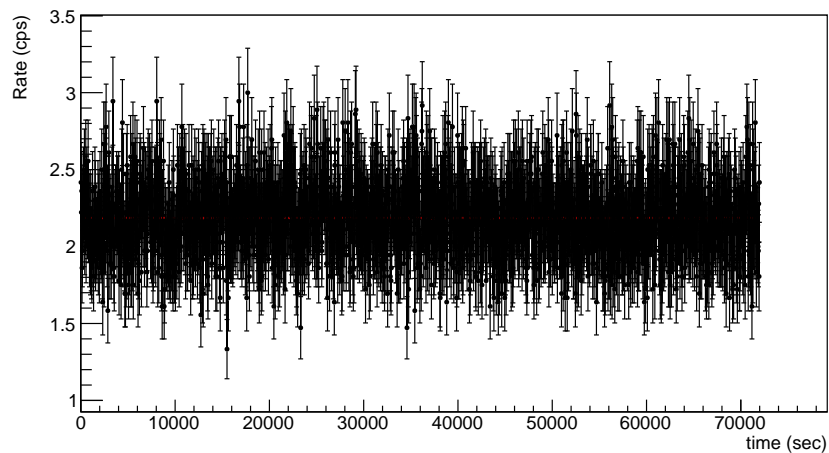


Figure 4.4.: Coincidence rate between large muon detectors on the ground on opposing sides ignoring the small upper panel. The mean rate is 2.19 ± 0.01 cps.

5. Simulations with the Extended Muon System

To derive theoretical expectations for count rates in the muon detectors from primary muons, it is useful to utilize Monte-Carlo based simulations. Due to the energies of the cosmic muons, they are minimal ionising particles. Thus, they move mainly along a straight line. Therefore, here it is rather uncomplicated to simulate muons, as a complex model of interaction with the geometry materials is of lower interest. However, a precise definition of the geometry and all input parameters is required. This chapter describes a simulation of cosmic muons inciding on the main spectrometer and their interaction with the muon detectors using the simulation toolkit Geant4. Coincidence rates were determined to compare with the results of the test measurements with the extended muon detection system (see chapter 4). It is possible to extract the coordinates where the muons cross the tank surface, i.e. the point where secondary electrons possibly are emitted. From these points the electrons can be tracked through the spectrometer to the FPD using electromagnetic simulations provided by the Kassiopeia package.

5.1. Geant4

To simulate cosmic muons hitting the main spectrometer and the muon detectors the Geant4¹ package was used [68]. It is based on Monte-Carlo methods and allows to track particles through matter taking into account their interactions. Due to its flexibility it is widely used in many research fields like medicine, high energy, accelerator and nuclear physics.

The Geant simulation can be divided in 6 parts:

- **Detector Construction:** First, a world volume, the geometry of the spectrometer tank and the muon detectors are defined.
- **Primary Generator Action:** Particle properties like mass and electric charge for the muons are defined. The initial position, energy and momentum direction are generated.
- **Run Action:** A run is the highest level of the simulation hierarchy. The geometries and the defined physical processes are fixed for a run. A run contains a number of events at same conditions.

¹GEometry ANd Tracking

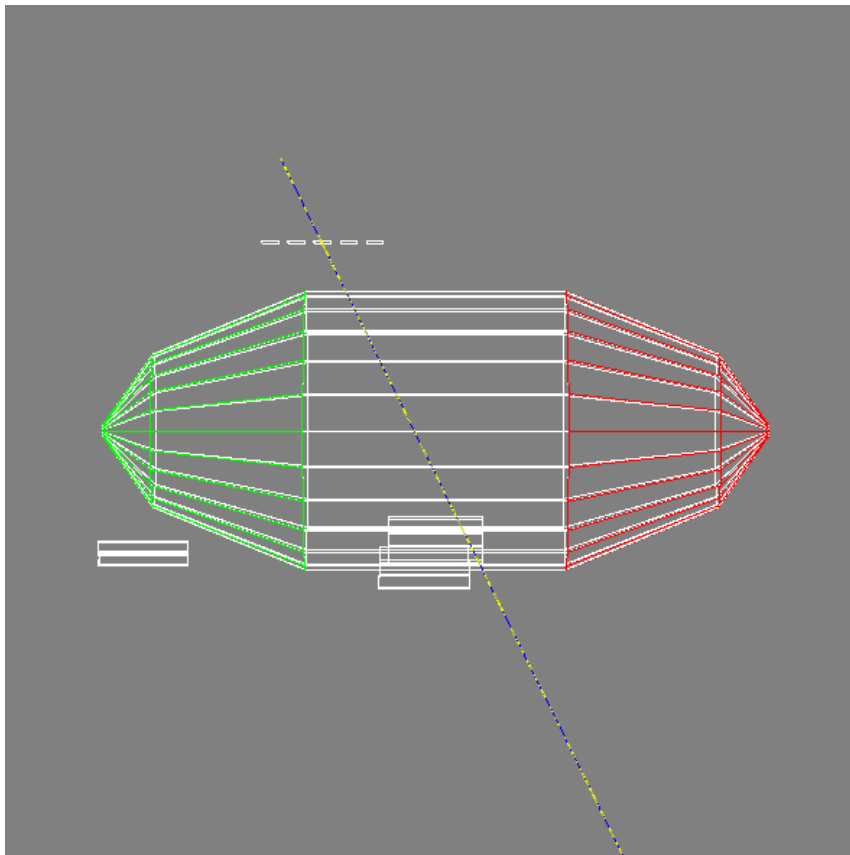


Figure 5.1.: Geant4 geometry of the main spectrometer and muon modules. Upstream is on the left side (green), downstream on the right side (red). The muon panels are shown in white. The yellow-blue line is the trajectory of a tracked muon.

- Event Action: For each event one primary muon with specific initial properties is generated and tracked through the world volume.
- Tracking Action: The track contains position, energy and momentum direction of a particle of the current calculation step.
- Stepping Action: The tracking of the particles is done in steps where in each step the positions and physical quantities are recalculated, yielding the total trajectory. A step contains two points. One pre-step point and one post-step point, which are the points before and after a calculation step. Thus it contains the "delta" information between the tracking points.

5.2. Simulation Setup

An already existing geometry of the main spectrometer (slightly adjusted see. 5.5) and the eight² muon modules [63], was extended by additional modules on top of the spectrometer. Five small modules were added at the corresponding positions of the coincidence test measurements (see 4.3). The module shape was approximated with a flat cube ($0.58 \times 0.5 \times 0.08$ m) with same area than the more complex form of the real module. The deviation between real and approximated volume is small and the influence on the results can be neglected. To reduce computing time, the simulation was run with all five small modules at once and not successive like in the real measurement.

²There are eight large modules, but module 2 was excluded from all analyses and simulations due to inferior performance

Module	x[m]	y[m]	z[m]
1	-5.55	-4.16	10.34
3	-4.02	-5.30	0.41
4	-4.48	-4.84	0.41
5	-4.94	-4.38	0.41
6	6.79	-4.17	1.24
7	6.28	-3.66	1.24
8	5.78	-3.16	1.24
S1	0.49	6.50	2.09
S2	0.49	6.50	2.99
S3	0.49	6.50	3.89
S4	0.49	6.50	4.79
S5	0.49	6.50	5.69

Table 5.1.: Module positions implemented in the Geant4 detector construction. S stands for "Small module". The coordinate origin is in the center of the spectrometer. The x-axis points from the center perpendicular to the beam line eastwards, the y-axis upwards. The z-axis corresponds to the spectrometer axis and points upstream. Module 2 was excluded (see chapter 3).

$\cos(\theta)$	c_0	c_1	c_2	c_3	c_4	max. rel. error
0-0.002	0.11137	0	0	0	0	0.004
0.002-0.2	0.11148	-0.03427	5.2053	-14.1971	6.138	0.3
0.2-1	0.06714	0.71578	0.42377	-0.19634	-0.021145	0.7

Table 5.2.: Parametrisation of the $\cos^*(\theta)$ distribution for different polar angle intervals.

To implement a volume in Geant4 one has to define its center. The coordinates for the large modules (except the excluded module 2) and the 5 different positions of the small module where measured. The position of the platform where the small module was mounted were obtained from a technical drawing [69]. The coordinates implemented in the Geant simulation are contained in table 5.1. The particle generator was adjusted and a $\cos^*(\theta)$ distribution (see equation 5.1) for the primary muons was implemented. The angle θ denotes the polar angle between the horizontal and the particle trajectory. This distribution is proposed in [67] and is defined by the equations 5.1, 5.2 and 5.3, and the parameters in table 5.2:

$$\cos^*(\Theta) = S(\Theta) \cdot \cos^{**}(\Theta) \quad (5.1)$$

with

$$S(\Theta) = 0.986 + 0.0007 \cdot \sec(\Theta) \quad (5.2)$$

and

$$\cos^{**}(\Theta) = \sum_{i=0}^4 c_i \cdot \cos^i(\Theta) \quad (5.3)$$

The distribution is the average over a wide range of muon energies. In [67] for $\cos(\theta)$ larger than 0.8 the flux is assumed as flat. To achieve a continuous distribution the original $\cos(\theta)$ interval was extended to 1. The primary energy was set to a fix value of 1 GeV, as the influence of the energy on the flight paths is negligible. A total number of 13.1 million primary muons were generated in a plane of 30 m \times 20 m above the main spectrometer model and tracked through the world volume. The plane is located 9 m centered over the spectrometer axis. The size and position of the starting plane was defined such that

Position	N	$R^{\text{sim}}[\text{cps}]$
1	7092 ± 84	64 ± 1
2	7027 ± 84	64 ± 1
3	7132 ± 84	65 ± 1
4	7263 ± 85	66 ± 1
5	7183 ± 85	65 ± 1

Table 5.3.: The table shows the number of hits for the small module at different positions. The simulation corresponds to a measurement time of about 110s. This time can be derived from the muon flux of 199 ± 0.14 cps determined with the real measurement.

the muon flux covers the whole tank and also muons with small polar angles can hit the spectrometer and the muon detectors.

5.3. Coincidence Rates

The number N , how often the small module was hit at each position, was determined. To compare these results with experimental data, the "simulated rate" was calculated. For a total number $N_{\text{total}}^{\text{sim}}$ of simulated primary muons in a plane with area A (600 m^2) and a muon flux Φ the simulation corresponds to a certain measurement time T^{sim} .

$$T^{\text{sim}} = \frac{N_{\text{total}}^{\text{sim}}}{A \cdot \Phi} \quad (5.4)$$

This yields a simulated rate of:

$$R^{\text{sim}} = \frac{N}{T^{\text{sim}}} \quad (5.5)$$

For the muon flux Φ the mean flux Φ_{exp} measured with the small module at the time of the test measurement was used. The mean rate of the module was 57.6 ± 0.04 cps, which corresponds to a muon flux Φ_{exp} of about $199 / \text{sm}^2$. This yields a simulated measurement time of ~ 110 s. For the simulated rate of the small module, the detection efficiency then is already considered as it decreases slightly the measured rate and in consequence the muon flux used to determine T^{sim} . The simulated rates are contained in table 5.3. The rates are within 90% in agreement with the measured mean rate of 57.6 cps. For each hit in the upper module it was checked if the muon also passes the volume of at least one large module on the ground and also crosses the main spectrometer wall. Due to the positions of the modules, all muons detected in the small module and at least one large module on the ground cross the spectrometer volume. As there are two panels involved in a coincidence event, one has to correct the simulated coincidence rate by multiplication with the detection efficiency of the modules on the ground of $\eta \approx 93\%^3$ [63] in order to compare with measured rates. The number of coincidence events, the simulated coincidence rates and the deviation to the measured rates $R_{\text{coinc}}^{\text{exp}}$

$$\Delta R = R_{\text{coinc}}^{\text{exp}} - R_{\text{coinc}}^{\text{sim}} \quad (5.6)$$

are shown in table 5.4.

The determined coincidence rates are in the order of the measured rates. Within the uncertainties the trend of decreasing rate along the spectrometer axis could be reproduced. However, at each positions the simulated coincidence rate is significant lower than the

³Only the detection efficiency of module 7 was determined until now. The other modules are treated to have the same detection efficiency

Position	N	$R_{\text{coinc}}^{\text{sim}}[\text{cps}]$	$\Delta R[\text{cps}]$
1	155 ± 12	1.31 ± 0.11	-0.48
2	153 ± 12	1.29 ± 0.11	-0.47
3	118 ± 11	1.00 ± 0.10	-0.62
4	113 ± 11	0.97 ± 0.10	-0.52
5	106 ± 10	0.90 ± 0.09	-0.46

Table 5.4.: Simulated coincidence rate R^{sim} between the small module and any module at the bottom for different positions of the small module.

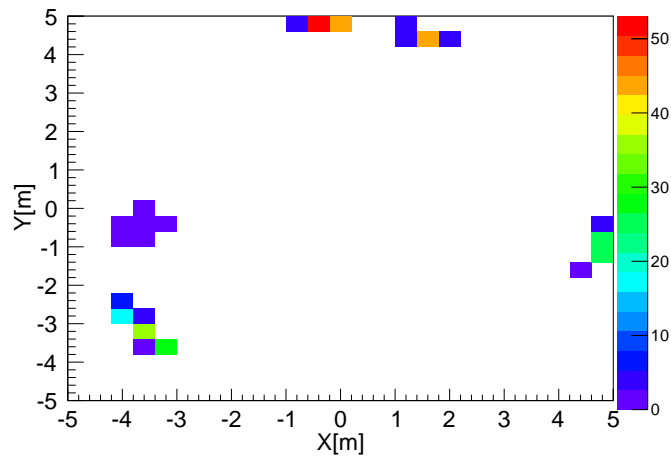
measured rate. The deviation to the measured coincidence rates is between $0.46 - 0.62$ cps which corresponds to a percentage of up to 39% referred to the measurements. A small deviation arises because the simulated coincidence rates were determined using the measured mean rate during the test measurements and not individual rates for the positions respectively. However, this effect is small. The fact that the deviation is large and that it can be observed at each position, suggests an unknown systematic origin in the simulation or in the measurements. Due to the used $\cos^*(\Theta)$ distribution of the muon polar angles, the coincidence rates are strongly influenced by the muon module positions. Deviations between the positions in the simulation geometry and the real modules will influence the simulated coincidence rates. Another reason for the observed deviation might arise from uncertainties in the distribution of the polar angles, as the implemented angular distribution is an approximation. Additionally, some of the low energetic muons might be deflected or even stopped by interactions with the ceiling of the spectrometer hall or at the tank wall. As low energetic cosmic muons only occur with small polar angles at sea level, this would change the shape of the angular distribution and increase the fraction of larger polar angles.

In principle, there might be unknown effects related to the measurement. Accidental coincidences are very unlikely since for the coincidence events the maximum time difference between the hits in the two modules was set two 100 ns and the mean time difference between two hits in the large muon detectors is in the order of 4 ms and even larger for the small module. A high background originating from nuclear decays in the spectrometer hall could not be observed, as the measured rates match the expected muon flux. The simulated muon rate of the small module is even higher than the measured rate.

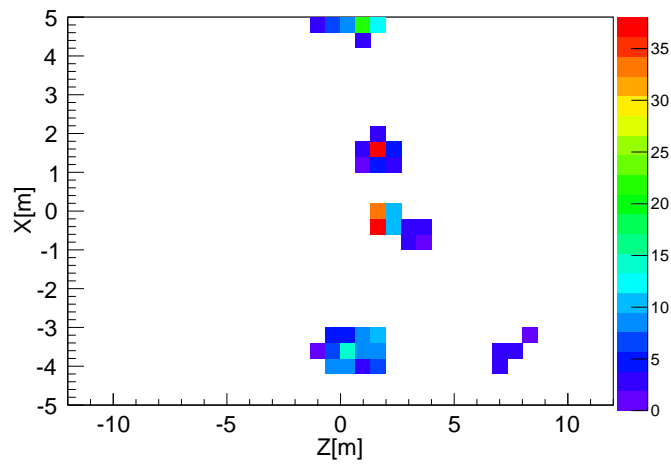
5.4. Extraction of Surface Crossing Points

The Geant simulation was used to extract the coordinates where the muons of simulated coincidence events crossed the tank wall. It was required that in the same event the small module on top and at least one module on the ground were hit. This allows to determine the regions where muons detected in the muon panels produce secondary electrons. The simulation program Kassiopeia 5.5 can then be used to investigate the behaviour of these secondaries within the spectrometer by starting electrons at the wall and track them through the spectrometer volume. This section contains the results for the small module at position 1 (for the other positions see Appendix D). Figures 5.2(a) - 5.2(c) show the coordinates of the interaction points projected to different planes.

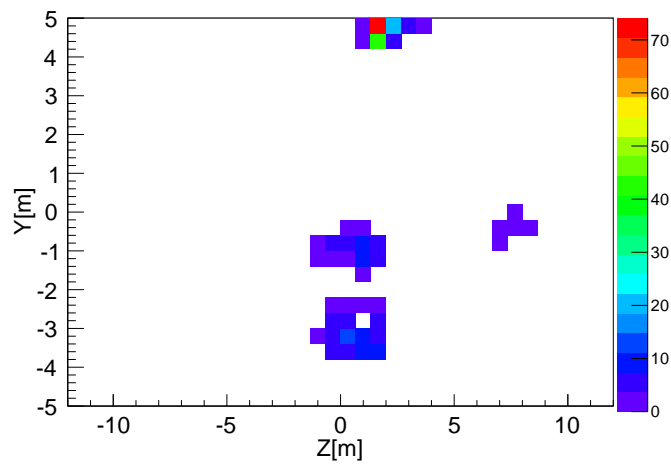
XY plane (figure 5.2(a)): This is the perspective of an observer who looks from the source side downstream. One can observe the expected picture. On the top there are the two spots near the position of the small module belonging to events with modules on the east or west side respectively. Further down on the left side one can see the spot near the 3 stacked modules 6-8 and on the left side a lot of events at lower y values for the modules 3-5. Across one can see a few events belonging to module 1. Due to the geometrical



(a) XY-plane



(b) ZX- plane



(c) ZY-plane

Figure 5.2.: Coordinates for crossing points with tank wall of coincidence events between the small module and any module on the ground projected to different planes.

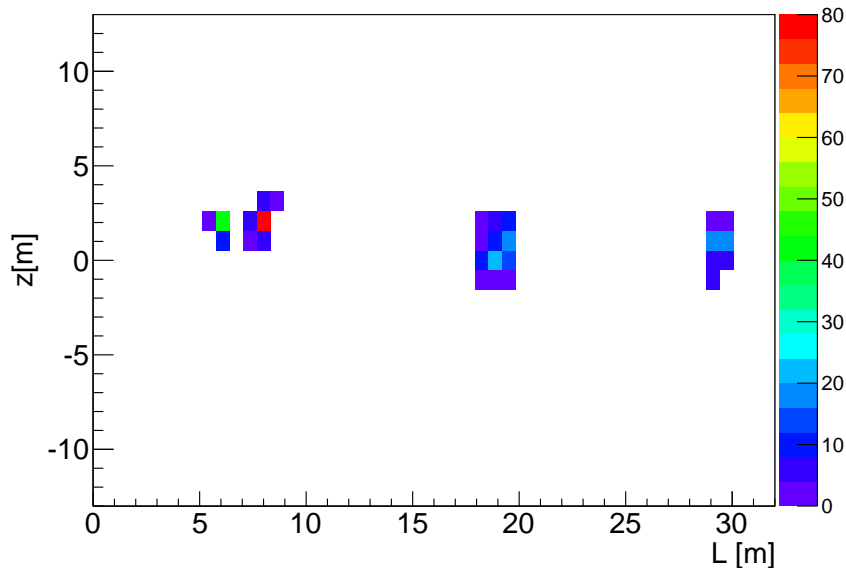


Figure 5.3.: Coordinates where muons of coincidence events crossed the spectrometer surface projected to the area of the cylindrical section of the spectrometer. The origin of the L-axis is at the point $(x=4.9\text{m}, y=0)$. Looking upstream, L denotes the distance from this point moving clockwise on the hull.

arrangement of module 1 relative to the small module at position 1, coincidence events with module 1 are much less likely.

ZX plane (figure 5.2(b)): Shown is the view from above the spectrometer. One can clearly identify the locations of the modules. 3 spots are in the center near the position of the small module. One large on the top for the modules 6-8 at the east side, one on the bottom for modules 3-5 and a few events at higher z-values for module 1.

ZY plane (figure 5.2(c)): This is the perspective from the west side on the spectrometer. The spot on top in the middle near the small module can be seen. Further down there are events on the spectrometer surface near the modules 6-8 and at lower y values for the modules 3-5. On the right side one can imagine the position of module 1.

Surface of cylindrical section (figure 5.3):

Figure 5.3 shows the coordinates of coincidence events projected to the surface of the cylindrical section of the spectrometer. This section has a circumference of about 31 m. The origin of the shown L-axis is at the most eastern point $(x=4.9\text{m}, y=0)$ on the hull. Looking upstream, L denotes the distance from this point moving clockwise along the surface. Consequently, $L \approx 7\text{m}$ is the surface region near the small module where the two spots are visible. Two pixels in this region contain a fraction of about 40% of all coincidence events. One pixel has an area of 0.67m^2 . This shows the very good spatial resolution. The rectangular at $L \approx 18\text{m}$ belongs to the region near the modules 3-5 on the west side and the spot at $L \approx 30\text{m}$ to the stacked modules 6-8. Coincidence events with module 1 involved are missing here as these muons do not cross the spectrometer wall at the cylindrical section.

5.5. *Kassiopeia*

The *Kassiopeia* package [70] is a powerful simulations program of the KASPER framework. It contains a detailed model of the main spectrometer and other KATRIN components.

This enables the simulation of various processes using Monte-Carlo methods. Examples are electromagnetically tracking of particles or their interaction with gas molecules like hydrogen or argon. One important tool is the tracking of particles through the spectrometer volume to produce predictions for measurement results. Several parameters, like air coil currents, tank potential or magnetic fields of the detector and pre spectrometer solenoids, can be set. The resulting electric and magnetic fields inside the spectrometer are calculated. Additionally, one has to define the particles to track with their initial position, direction and energy. For this, many particle generators exist that set these parameters due to particular distributions. Examples are Gaussian, Poissonian distributed or fixed values. Then the particles are tracked until a defined condition terminates the tracking.

A generator was implemented which reads in coordinates from a data file and sets them as initial position for the electrons. Therefore, the Geant4 spectrometer geometry was slightly adjusted to match the geometry in Kassiopeia. Therewith one can derive expectations for coincidence measurements between FPD and muon module counts.

5.6. Resulting Pixel Distributions

By applying asymmetric magnetic fields within the main spectrometer secondary electrons produced from the surface are guided along the magnetic fields towards the detector. Most of them are reflected due to the magnetic mirror effect, but a small fraction follows the magnetic field lines to the detector. In order to maximize the coincidence rate between muon detector and FPD, the magnetic field settings need to be optimized. Most important, one has to reach a high coverage of the surface area that is surveyed by the muon modules and the area that is covered by the flux tube. For the small module at position 1, an asymmetric magnetic field setting proposed in [71](see table 5.5) was applied to derive a prediction for the respective FPD pixel distribution. The geometry of the main spectrometer with the magnetic field lines is shown in figure 5.4. The flux tube covers a large area of the surface at the middle of the spectrometer, where most of the coincidence events occur.

The electrons were started at the respective positions obtained with the Geant simulation. Magnetic tracking was used, which means the particles follow the magnetic field lines and time intensive electric field calculations are omitted. Thus, the simulation is very fast compared to a realistic particle tracking, but provides no information about the fraction of secondary electrons that can reach the detector. More complex simulations are required to determine realistic electron trajectories taking into account the electric potential and the fact that most of them are reflected by the magnetic mirror effect. Nevertheless, magnetic tracking is sufficient to determine the expected pixel distributions at the FPD. Figure 5.5 contains the pixel distribution for the small module at position 1 and the asymmetric magnetic field setting created by the currents in table 5.5. One can see that all events occur in three defined regions. The spot below on the left side belongs to coincidence events in the modules 3-5 at the west side, the spot on the right side to events in the modules 6-8 on the east side of the spectrometer. A fraction of 95% of the electrons from the wall is detected at the FPD. This shows a good agreement between the regions monitored by the muon panels and the surface regions covered by the flux tube. Most of the events occur on top in the middle of the wafer coming from the upper surface region near the small module. A fraction of about 1/3 of all electrons reaching the FPD is detected at 5 pixels coloured in red and green in this region.

Summarising one can note that the Geant4 simulation combined with the Kassiopeia package is a powerful tool for investigations of muon induced background. The Geant simulation gives access to the regions on the spectrometer surface where secondary electrons are emitted. The results confirm the expectation that with a module above the spectrometer

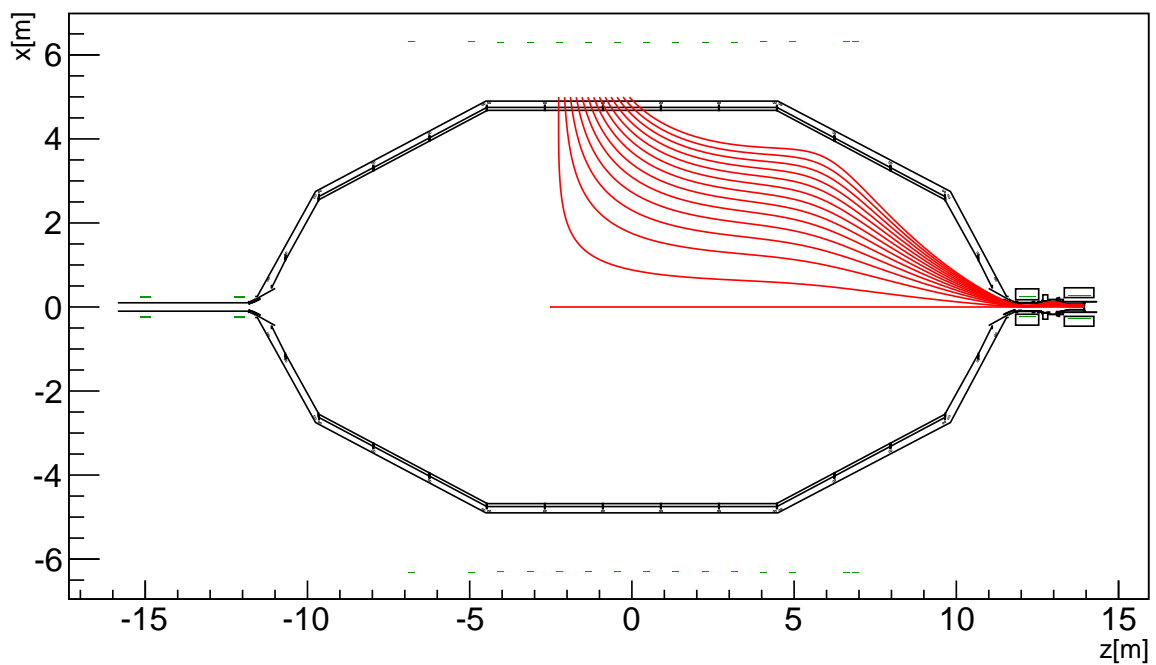


Figure 5.4.: Flux tube of asymmetric magnetic field setting. The set currents can be obtained from table 5.5. In the graphic the common coordinate system for the main spectrometer is used which is different to the one in Geant4. Here, the z -axis is inverted with respect to coordinate system of the simulation. The field is rotationally symmetric to the beam line.

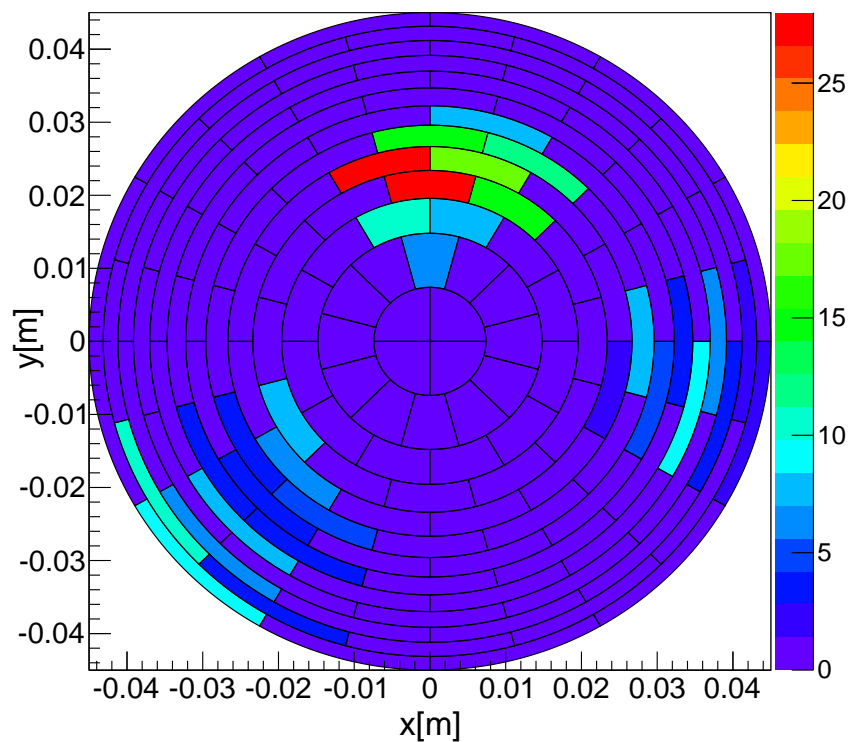


Figure 5.5.: Pixel map for asymmetric magnetic field setting applied (table 5.5).

	Current [A]
Air Coil 1	-100.0
Air Coil 2	-100.0
Air Coil 3	-50.0
Air Coil 4	0.0
Air Coil 5	0.0
Air Coil 6	0.0
Air Coil 7	40.0
Air Coil 8	80.0
Air Coil 9	80.0
Air Coil 10	80.0
Air Coil 11	80.0
Air Coil 12	80.0
Air Coil 13	80.0
Air Coil 14	70.0
Pinch	72.6
Detector	54.6
Pre Spec 1	0.0
Pre Spec 2	0.0

Table 5.5.: Asymmetric magnetic field setting.

a very good spatial resolution can be reached. Consequently, with an appropriate asymmetric magnetic field applied, a large fraction of the events occurs on few pixels of the FPD. For coincidence measurements between muon modules and FPD counts this enables a discrimination criterium. This means selecting events on pixels that "see" the respective regions on the surface and reject all other pixels. The coincidence rates are relative high due to the position of the small module. Further simulations with more complex particle tracking might help to optimise the magnetic field setting in order to achieve a high coincidence rate taking into account that most of the secondary electrons are reflected by the magnetic mirror effect on their paths towards the detector.

6. Long Term Muon Measurement

The cosmic muon flux is not constant over time. As this fact has an direct impact on the background rate due to secondary electrons from the spectrometer surface, further investigations of the muon rate fluctuations are important. The muon intensity I_{SL} at sea level can be written as [65]:

$$I_{SL} = I_i \cdot (1 - a_\mu \Delta p + \beta \Delta h - \gamma \Delta T) \quad (6.1)$$

where I_i denotes the initial cosmic muon flux in the atmosphere and Δp , Δh , ΔT fluctuations of pressure, muon production height and temperature. A long term measurement of the total muon rate was performed for 12 weeks with seven large muon detectors. An analysis to determine the coefficients α_μ , β and γ by fitting expression 6.1 to the total muon rate using local weather data can be found in [72]. The stability of the ADC values of each detector was investigated as drifts can directly affect the detection efficiency. In addition, the influence of the muon flux fluctuations on the KATRIN antineutrino mass sensitivity was investigated performing an ensemble test. The data used for the analysis presented here was taken from the 25th of April at 11:53am to the 17th of July 5:03pm 2014 (muon runs: 1677-3699). Almost each run has a duration of 1h, as the measurement needed to be interrupted a few times for a short times some runs are shorter.

6.1. Long Term Stability of Muon Modules

As described in chapter 3, the ADC histogram of an accurately working muon panel has to have a landau shape, as this is the characteristic form of the muon energy loss in the scintillators. At the re-activation of the modules, the voltages were set in order to reach a sufficient detection efficiency. For the entire duration of the long term measurement, the ADC histogram was recorded for each run and channel to ensure that the modules work reliable during the whole measurement. A Landau function was fitted to the ADC spectrum of each run in order to check for variations of the peak position (MPV¹) over long time scales. This is illustrated in figure 6.1 for muon panel 5, channel on side A. In the peak region the fitted function is in good agreement with the data. The MPV is 6974 ± 0.5 .

In figure 6.2 the peak positions for all used channels are plotted as a function of time. The peaks for all channels are relative constant during the whole time. At a time of 18, 26,

¹Most Probable Value

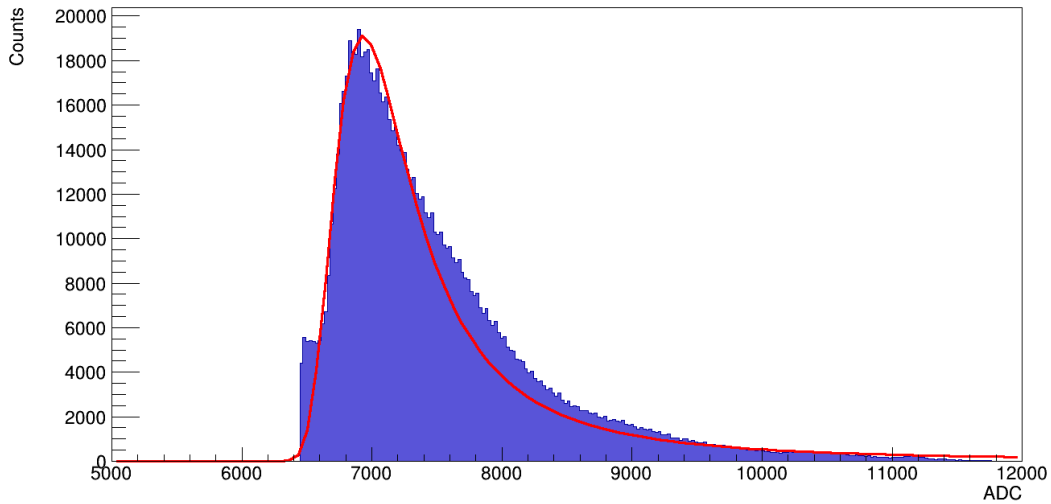


Figure 6.1.: ADC histogram for muon panel 5, side A channel. At the peak region the fitted landau function matches well the ADC shape. The fitted MPV is 6974 ± 0.5 .

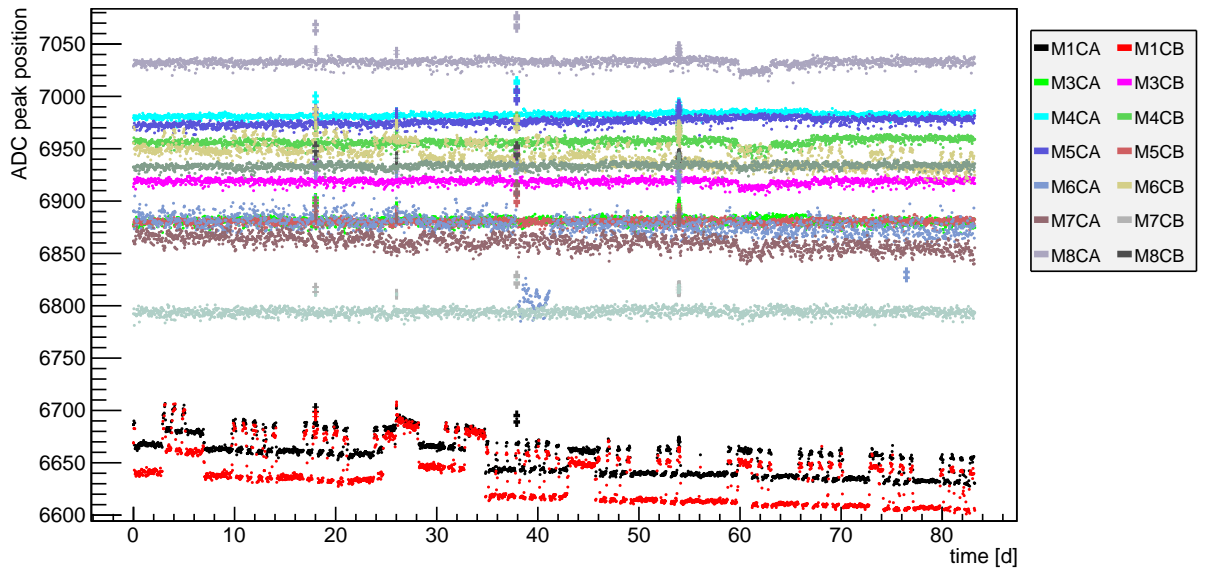


Figure 6.2.: MPV's for all channels of the 7 used modules on the ground over 12 weeks. The largest variations of about ± 30 ADC bins can be observed for the two channel of module 1. Although some fluctuations can be observed, all channels show a good stability. Qualitative quantities can be obtained from table 6.1. For better visualisation of the peak positions for single modules see appendix E.

Channel	Peak
M1CA	6656.7 ± 0.4
M1CB	6637.3 ± 0.5
M3CA	6881.3 ± 0.1
M3CB	6918.8 ± 0.1
M4CA	6982.3 ± 0.1
M4CB	6956.5 ± 0.1
M5CA	6975.9 ± 0.1
M5CB	6880.4 ± 0.1
M6CA	6875.0 ± 0.9
M6CB	6944.9 ± 0.2
M7CA	6860.4 ± 0.2
M7CB	6794.3 ± 0.1
M8CA	7032.4 ± 0.1
M8CB	6933.5 ± 0.1

Table 6.1.: Mean peak positions of the ADC histogram for seven muon modules over 12 weeks.

38, 54 days from the beginning of the measurement a distinct deviation from the mean value can be observed for various channels. At these times, the usual sequence of 1 hour runs was interrupted for a short time to do test measurements with a small panel or for a hardware check and maintenance. Consequently, the fit did not work properly due to the limited statistics in these runs.

The two channels from module 1 show a step-like pattern in some time intervals. This indicates that this is a systematic and no random effect. The photomultipliers might be influenced by the magnetic field in the experimental hall. As alternative, this effect might originate from a light leak in the modules. This means that ambient light can enter the interior of the modules and lead to additional noise. This is indicated by the fact that in several regions sets of five jumps can be observed. On the five weekdays the light usually is switched on in the morning and switched off in the evening. This might lead to additional noise that shifts the MPV of the landau distribution. As the stability of these channels is still good this was not investigated further. Table 6.1 contains the mean values of the MPV's. Summarizing one can state that all channels of the 7 used panels have sufficient stability.

6.2. Muon Rate Variations

Figure 6.3 contains the total muon rate of seven muon detectors over 12 weeks. The rate was averaged over 1 hour to achieve a better visualisation of the long term trend, as on shorter time scales the rate fluctuates over about 2%. The rate was normalised to the mean rate of 1592.62 ± 0.05 cps. Over the entire measurement time, rate variations of about 6% can be observed. There are also superimposed variations on shorter time scales which might originate from temperature fluctuations associated with the day-night cycle for example. Over the whole time window a decreasing trend can be observed. Here no statement about the origin of the fluctuations can be given. Correlations between local weather data and the recorded muon rate are currently under investigation [72].

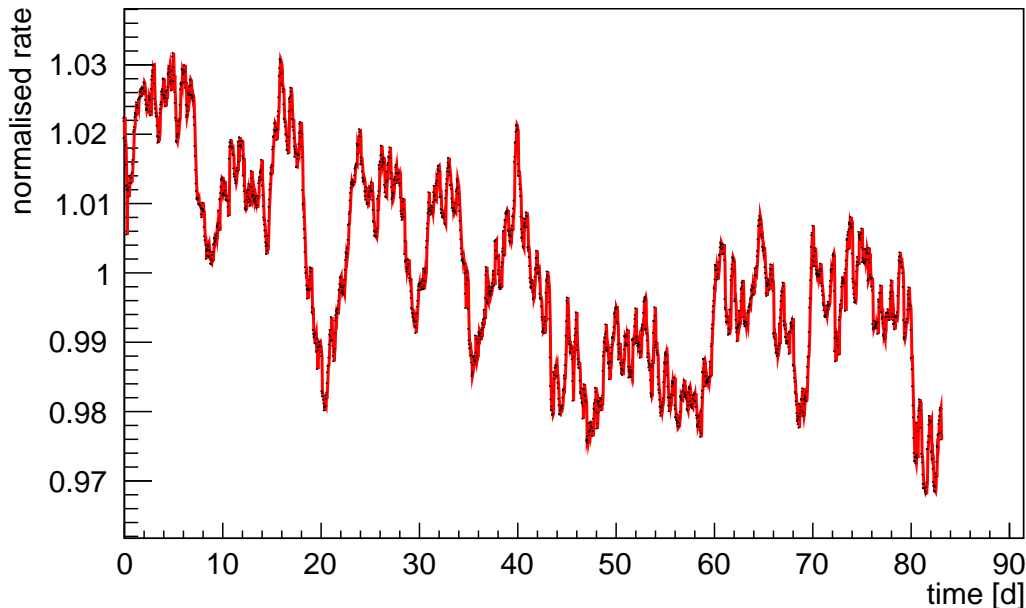


Figure 6.3.: Total muon rate of 7 large muon detectors over 12 weeks. The rate was averaged over 1h and normalised to the mean rate of 1592.62 ± 0.05 cps.

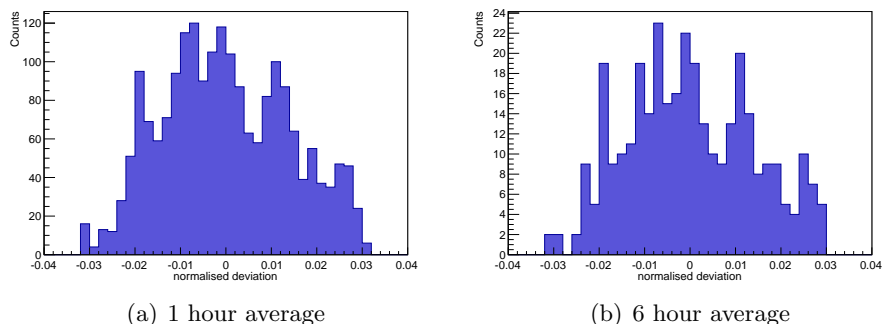


Figure 6.4.: Normalised deviation of the muon rate for each data point of the long term measurement to the mean rate averaged over 1 and 6 hours.

6.3. Sensitivity Investigations with non-Poissonian Background

The statistical uncertainty on the neutrino mass is influenced by the background rate. A non-Poissonian background due to fluctuations of the muon flux might lead to larger uncertainties compared to a Poissonian background. A background model was developed that involves the variations in the muon rate. The influence of this background model on the statistical uncertainty on the neutrino mass at 90% C.L. and thus on the total sensitivity was investigated and is described in this section.

6.3.1. Sensitivity Definition

The sensitivity of an experiment is a measure for its combined systematic and statistic uncertainties. The KATRIN experiment aims to reach a sensitivity on the effective antineutrino mass of $200 \text{ meV}/c^2$ by determining the shape of the tritium β -spectrum. Specifically for KATRIN, this value represents the smallest neutrino mass value up to which the null hypothesis of a vanishing neutrino mass can be rejected. In case of a smaller neutrino

source of systematic shift	achievable / projected accuracy	systematic shift $\sigma_{\text{sys}}(m_\nu^2)$ (10^{-3} eV^2)
description of final states	$f < 1.01$	< 6
T^- ion concentration	$< 2 \cdot 10^{-8}$	< 0.1
unfolding of the energy loss function $f(\varepsilon)$		< 6
monitoring of column density ρd	$\Delta T/T < 2 \cdot 10^{-3}$	$< \frac{\sqrt{3.6.5}}{10}$
	$\Delta \Gamma/\Gamma < 2 \cdot 10^{-3}$	
	$\Delta \varepsilon_T/\varepsilon_T < 2 \cdot 10^{-3}$	
	$\Delta p_{\text{inj}}/p_{\text{inj}} < 2 \cdot 10^{-3}$	
	$\Delta p_{\text{ex}}/p_{\text{ex}} < 0.06$	
background slope	$< 0.5 \text{ mHz/keV (Troitsk)}$	< 1.2
HV variations	$\Delta HV/HV < 3 \text{ ppm}$	< 5
WGTS potential variations	$\Delta U < 10 \text{ meV}$	< 0.2
WGTS mag. field variations	$\Delta B_S/B_S < 2 \cdot 10^{-3}$	< 2
elastic $e^- - \text{T}_2$ scattering		< 5
identified syst. uncertainties	$\sigma_{\text{sys, tot}} = \sqrt{\sum \sigma_{\text{sys}}^2} \approx 0.01 \text{ eV}^2$	

Figure 6.5.: List of systematic uncertainties. Taken from [13]

mass, this value can be set as an upper limit. For Gaussian distributed values of m_ν^2 the sensitivity at 90% C.L. is given by:

$$S_{m_\nu^2} = \sqrt{1.645 \cdot \sigma_{m_\nu^2, \text{tot}}} \quad (6.2)$$

$$\sigma_{m_\nu^2, \text{tot}} = \sqrt{(\sigma_{m_\nu^2, \text{stat}})^2 + (\sigma_{m_\nu^2, \text{sys}})^2} \quad (6.3)$$

with systematic $\sigma_{m_\nu^2, \text{sys}}$ and statistic uncertainties $\sigma_{m_\nu^2, \text{stat}}$. Figure 6.5 contains a list of expected systematic uncertainties on the squared neutrino mass. This list is taken from the KATRIN Design Report [27]. A total systematic uncertainty of $\sim 0.01 \text{ eV}^2$ is identified. Due to possible unknown uncertainties this value might increase. Thus, as proposed in [73], for the sensitivity analysis a total systematic uncertainty of

$$\sigma_{m_\nu^2, \text{sys}} = 0.017 \text{ eV}^2 \quad (6.4)$$

was assumed. The following sections describe the procedure to derive the statistical uncertainty for non-Poissonian background due to muon flux variations.

6.3.2. KaFit

KaFit is a module of the KASPER software framework, which provides various statistical methods to extract neutrino masses from simulated data, since no data of tritium measurements is available yet. This is done by numerical simulation of the whole measurement process.

Measurement simulation: kffit-fitter

The KaFit application kffit-fitter was used to generate physical observables and afterwards to infer parameters from the observations. First of all a spectrum for electrons from tritium decays is simulated with input of various characteristics of the source and transport section. For the sensitivity investigation the reference simulation parameters described in [13] were used. Additionally, a background model has to be assumed. Various models with different probability distributions are implemented. Then the entire process of energy

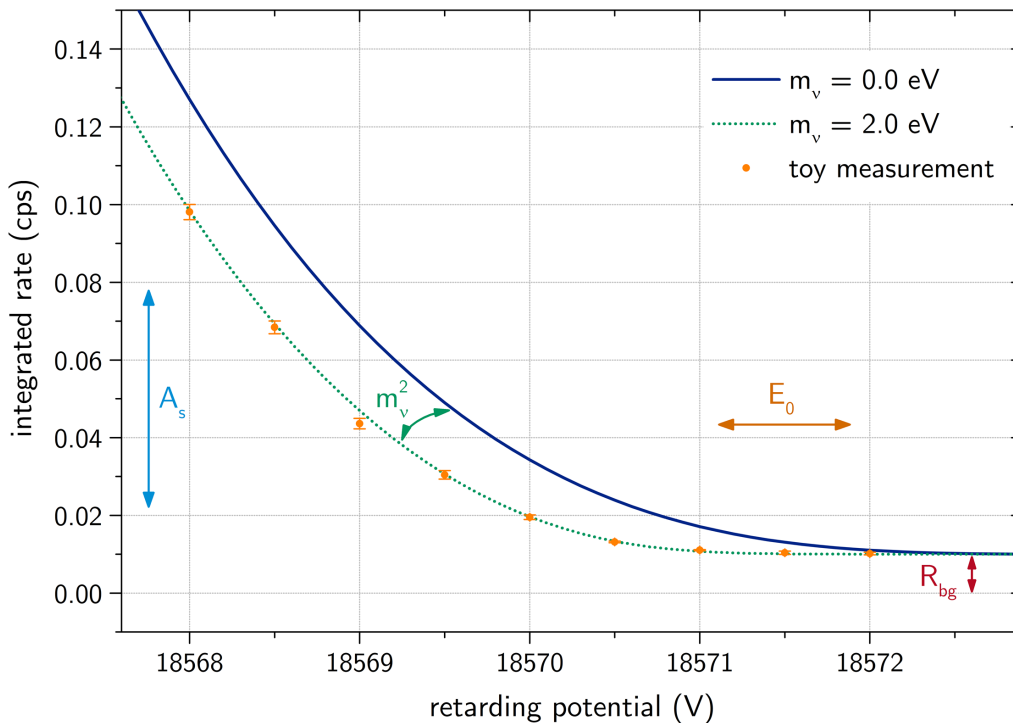


Figure 6.6.: The figure illustrates the parameter inference from an integrated β -spectrum. Squared neutrinos mass m_ν^2 , Endpoint energy E_0 , signal amplitude A_S and background rate R_{bg} are determined by fitting the theoretical spectrum to the data of a toy experiment. Figure taken from [13]

analysis in the spectrometer and detector section is simulated. For the real tritium measurements it is planned to operate the spectrometer at different retarding potentials and a total measurement time of 3 years. The amount of time t_i KATRIN runs at a particular retarding potential has to be optimised, in order to reach a good sensitivity (for example see table 6.2). The integrated β -spectrum, i.e. the numbers N_i of events detected for a retarding potential i , is simulated, which is the rate per time interval multiplied with the corresponding measurement time for the specific retarding potential.

$$N_i = \left(\frac{dN_i}{dt} \right) \cdot t_i \quad (6.5)$$

During a toy measurement, the number N_i is taken from a Poissonian distribution. Combined with the respective number of background events N_i^{bkg} , the total number of events at retarding potential i is:

$$N_i^{\text{toy}} = \text{Poisson}(N_i) + N_i^{\text{bkg}} \quad (6.6)$$

The number N_i^{bkg} depends on the assumed background model. By fitting the theoretical spectrum shape to the simulated integrated spectrum, one can infer theoretical quantities like the parameter of interest m_ν . In the simplest case the theoretical depends on 4 parameters, which are the source activity A_S (amplitude), the tritium spectrum endpoint energy E_0 , the background rate R_{bg} and the squared neutrino mass m_ν^2 .

6.3.3. KATRIN Likelihood Function

For parameter inference a Likelihood function is used. The likelihood is a measure for the probability of a certain observation N for particular theoretical input parameters Θ .

qU [eV]	t_{qU} [s]
18545.00	1050000
18546.00	1050000
18547.00	1050000
18548.00	1050000
18549.00	1050000
18550.00	1050000
18551.00	1050000
18552.00	1050000
18553.00	1050000
18554.00	1050000
18555.00	1050000
18556.00	1050000
18557.00	1050000
18558.00	1050000
18559.00	1050000
18560.00	1050000
18561.00	1050000
18562.00	1050000
18563.00	1050000
18564.00	1050000
18565.00	1050000
18566.00	1050000
18567.00	908164
18567.50	908164
18568.00	908164
18568.50	908164
18569.00	908164
18569.50	908164
18570.00	1975257
18570.50	12214808
18571.00	20728847
18571.50	2020665
18572.00	3300000
18573.00	3300000
18574.00	3300000
18575.00	3300000
18576.00	3300000
18577.00	3300000
18578.00	3300000
18579.00	3300000
18580.00	3300000

Table 6.2.: Measurement time distribution: Amount of time for a specific retarding potential. The total measurement time is about 3 years.

Generally, it can be written as:

$$L(\Theta_{\text{theo}}|N_{\text{obs}}) = P(N_{\text{obs}}|\Theta_{\text{theo}}) = \prod_i p(N_{\text{obs},i}|\Theta_{\text{theo}}) \quad (6.7)$$

For a number of theoretical model parameters Θ_{theo} it is the probability $P(N_{\text{obs}}|\Theta_{\text{theo}})$ how likely it is to obtain a number of observations N . P is the product of the probabilities p of all single observations $N_{\text{obs},i}$. For KATRIN, the likelihood is based on a model of β -decay theory, the experimental characteristics, transmission functions, detection efficiency, background model, statistical and systematic effects. One theoretical input parameter is the squared neutrino mass m_ν^2 KATRIN aims to determine. Nuisance parameters are the tritium endpoint energy E_0 , the signal amplitude A_S , and the mean background rate R_{bg} . Figure 6.6 illustrates a theoretical spectrum fitted to a simulated data and the impact of the 4 parameters on the spectrum shape. For this specific case one can write the likelihood as:

$$L(m_\nu^2, E_0, A_S, R_{\text{bg}}|N_{\text{obs}}) = \prod_i p(N_{\text{obs},i}|N_{\text{theo},i}(qU_i, m_\nu^2, E_0, A_S, R_{\text{bg}})) \quad (6.8)$$

where $N_{\text{obs},i}$ is the measured number of events at a particular retarding potential and $N_{\text{theo},i}$ the corresponding theoretical expected number. The input parameters are determined with a fit of the theoretical spectrum to the data. The parameter values at the global maximum of the likelihood are the best estimators. Or as commonly done, the parameters at the global minimum of $-\text{Log}L(\Theta|N)$.

6.3.4. Muon Data Background Model

A new background model was implemented in KaFit, which is based on real muon data from the performed measurement (see section 6.2). In the KaFit simulation procedure, for each time bin of the MTD a new number of background events N^{bkg} is set, depending on the background model. For a Poissonian distributed background the N^{bkg} is taken from a Gaussian distribution² with mean

$$N_i^{\text{bkg}} = t_i \cdot R_{\text{bg}} \quad (6.9)$$

and standard deviation

$$\sigma_{\text{pois},i} = \sqrt{N_i^{\text{bkg}}} = \sqrt{t_i \cdot R_{\text{bg}}} \quad (6.10)$$

where N_i^{bkg} is the number of background events in the respective MTD bin, which depends on the amount of time t_i for the bin and the mean background rate R_{bg} . This is reasonable for a constant mean background rate. As the muon flux variations have a systematic origin and are no statistical fluctuations, this leads to a probably non-Poissonian background component. To account for changes in the background rate on short time scales, the MTD was split into time bins in the order of hours. In this background model the mean background rate was assumed to be proportional to the measured incident muon flux. On short time scales the background rate is expected to be Poissonian distributed [13] as the muon rate changes rather on large time scales. The measured muon rate was averaged over a few hours and for each 6 hour average a Gaussian distribution for N^{bkg} was determined. The Gaussians were then summed up to derive a new distribution for the background rate that combines the Poissonian nature on short time scales and the non-Poissonian behaviour on longer time scales. One has to make clear that this is an assumption that is not proven by measurements. The true behaviour of muon induced secondary electrons over time is unknown and has to be investigated on long time scales (weeks). Long term coincidence

²For mean values larger than 30 a Poissonian distribution can be approximated with a Gaussian distribution. The used time bins lead to mean background rates of more than 200.

measurements between muon panels and FPD are planned in the near future. A more realistic muon background model might be realised by generating a signal that imitates the characteristics of the muon flux variations over the full 3 years of measurement time based on the long term measurement data. (See appendix B).

6.3.5. Ensemble Test

An ensemble test with 7500 toy measurements with the muon data background model was performed. This means the procedure described in section 6.3.2 was repeated 7500 times. For each run, the theoretical spectrum was fitted to the simulated spectrum for a true value of $m_\nu^2=0$ eV. The outcome are the best fit estimates for the 4 parameters described above including the parameter of interest m_ν^2 .

The reference MTD with scanned energies up to 30 eV below the endpoint energy in the simulation was used (see table 6.2). The measurement time for each potential was split up into bins of 6 hours. Consequently, for each 6 hour bin a new number of background events N^{bkg} is set. As the muon induced background is expected to be the dominant contribution to the total background rate, here no other background components were considered. The total muon rate was averaged over 6 hours. Figure 6.4(b) contains the deviations of the averaged muon rates to the mean rate normalised to the mean of 1592.62 cps. The variations are up to about $\pm 3\%$.

As described in section 6.3.4 the Gaussian distributions for all 6 hour average rates were determined to obtain a distribution for the number of background events per time bin that takes into account the muon flux variations. The ensemble test was done for three different mean background rates, the KATRIN design value of 10 mcps and two higher rates of 100 mcps and 400 mcps. Figure 6.7 contains the obtained distributions for N^{bkg} . For 400 mcps (see figure 6.7(c)) the shape of the distribution becomes a bit asymmetric. This originates from the asymmetric distribution of the muon rates shown in figure 6.4(b). It is only visible for the highest mean background rate, since the deviation to the respective Poissonian is much larger than for the two lower background rates. As this effect is small, all three histograms were fitted with Gaussian functions. The distribution of N^{bkg} was then chosen as a Gaussian with mean

$$N^{\text{bkg}} = R_{\text{bg}} \cdot t_i \quad (6.11)$$

and the standard deviation obtained from the fit as described above.

10 mcps:

For the KATRIN design background rate the standard deviation of the N^{bkg} distribution was determined to:

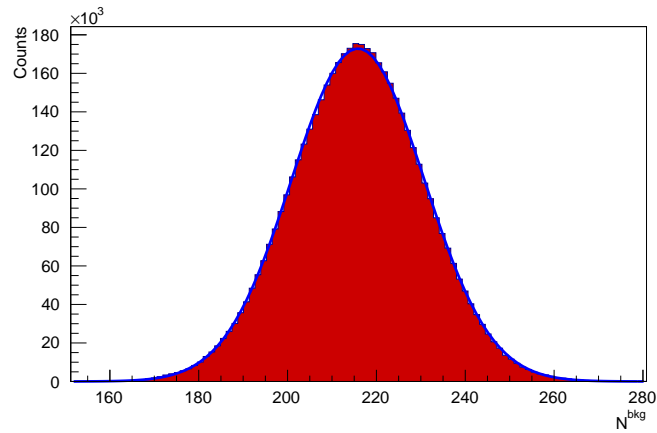
$$\sigma^{10\text{mcps}} = 14.98 = 1.0164 \cdot \sigma_{\text{pois}}^{10\text{mcps}} \quad (6.12)$$

Thus, in this model N^{bkg} is set according to a Gaussian distribution with a standard deviations by 1.64% larger than for a Poissonian background.

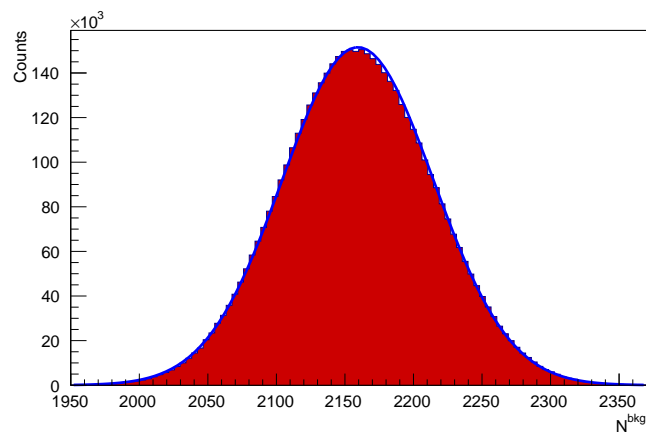
100 mcps:

For the higher background rate the standard deviations increases by 18,80% with respect to a Poissonian background.

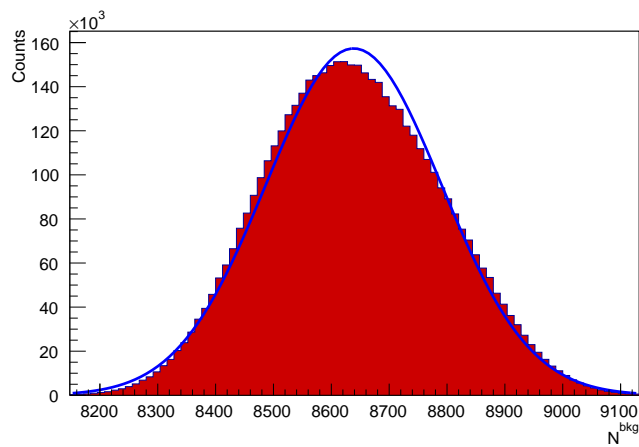
$$\sigma^{100\text{mcps}} = 55.21 = 1.1880 \cdot \sigma_{\text{pois}}^{100\text{mcps}} \quad (6.13)$$



(a) 10 mcps



(b) 100 mcps



(c) 400 mcps

Figure 6.7.: Distribution of the number of background events within 6 hour bins for mean background rates of 10 mcps, 100 mcps and 400 mcps fitted with Gaussian distributions. The mean number of background events within 6 hours are 216, 2160 and 8640 respectively. For 10 mcps the standard deviation is increased by 1.65% compared to a Poissonian distributed background, by 18.80% for 100 mcps and by 63.5% for 400 mcps.

400 mcps:

For 400 mcps the standard deviations increases by 63.50% compared to a Poissonian background.

$$\sigma^{400\text{mcps}} = 151.97 = 1.6350 \cdot \sigma_{\text{pois}}^{400\text{mcps}} \quad (6.14)$$

One can observe a trend that the difference between pure Poissonian background and this background model becomes larger for higher background rates. This indicates that the effect on the neutrino mass sensitivity shows the same dependence.

Generally, smaller time bins are preferable as the muon rate changes on much smaller time scales. However, the number of bins in the measurement time distribution has a big influence on the computational cost. The chosen time scale of 6 hours is the result of weighing up between a realistic background model and keeping the computing time on an acceptable level. A reduced total measurement time is no option as this would directly decrease the sensitivity. By splitting the optimised MTD into smaller time bins of equal size, one has to regard that the ratio of total measurement time for a specific potential and the used time scale for the background rate in most cases is not a whole number. Therefore the number of 6 hour bins was rounded. If the deviations from the original, optimised MTD are too big, this can affect the determined sensitivity. The maximum deviation is less than 0.8%. The total measurement time increases by 0.27% compared to the reference MTD. The influence on the determined uncertainties can be neglected.

6.3.6. Statistical Uncertainties

The m_ν^2 values are assumed to follows a Gaussian distribution. By determining the 1.645σ width one can make a statement about the statistical uncertainty of the m_ν^2 determination at 90% C.L. for the used background model. Combined with the the systematic uncertainty of

$$\sigma_{m_\nu^2, \text{sys}} = 0.017 \text{ eV}^2 \quad (6.15)$$

one can derive a number for the neutrino mass sensitivity (see section 6.3). In the following the results for three different mean backgrounds are presented and compared to sensitivities for pure Poissonian background with apart from that same simulation parameters ³.

Mean background rate: 10 mcps

First, the total background rate was set to 10 mcps which is the design value for the KATRIN experiment. The distribution of the best fit m_ν^2 is shown in figure 6.8. A Gaussian distribution was fitted to the histogram with a standard deviation of:

$$\sigma_{m_\nu^2, \text{stat}} = 0.0166 \pm 0.0001 \text{ eV}^2. \quad (6.16)$$

This yields to a sensitivity at 90% C.L. of:

$$S_{m_\nu^2} = (197 \pm 1) \text{ meV}. \quad (6.17)$$

The sensitivity for a Poissonian background with respective mean rate is $(197 \pm 1) \text{ meV}$ [13]. Thus, for the KATRIN Design background, under assumption of the used background model, within the uncertainties no impact on the sensitivity can be observed.

³The total measurement time is slightly longer (0.27%) with respect to the reference MTD due to rounding effects. The amount of time for a specific retarding potential differs by less then 0.8% compared to the reference MTD. The influence on the results can be neglected.

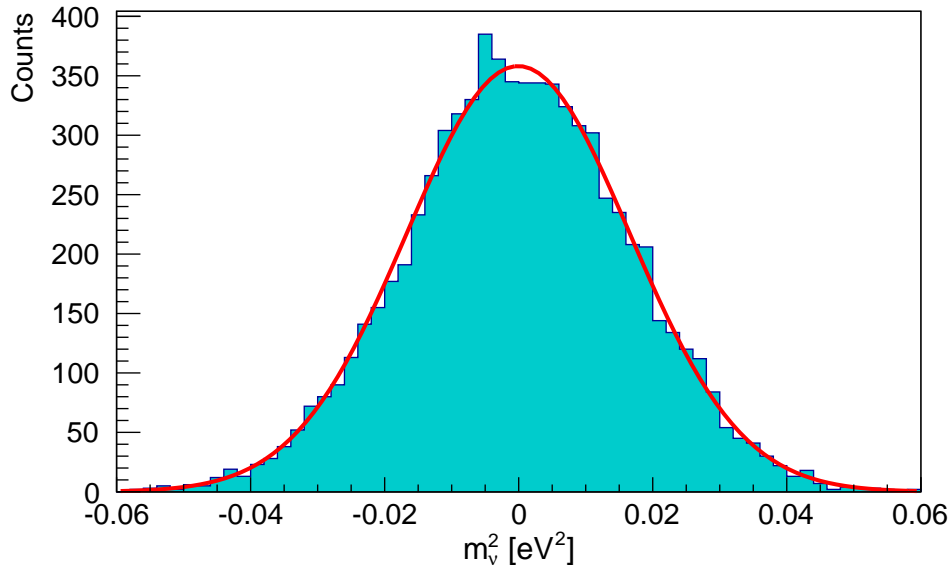


Figure 6.8.: Distribution of best fit squared neutrino masses for non-Poissonian background of 10 mcps fitted with a Gaussian distribution. The simulated neutrino mass was set to $m_\nu=0$ eV.

Mean background rate: 100 mcps

Figure 6.9(a) shows the best fit m_ν^2 estimates for a mean background rate of 100 mcps. The fitted Gaussian has a standard deviations of:

$$\sigma_{m_\nu^2, \text{stat}} = 0.0396 \pm 0.0003 \text{ eV}^2. \quad (6.18)$$

This corresponds to a sensitivity at 90% C.L. of:

$$S_{m_\nu^2} = (266 \pm 1) \text{ meV}. \quad (6.19)$$

For a pure Poissonian background with mean of 100 mcps and the reference parameters, the sensitivity yields (254 ± 1) meV [13]. The muon flux variations lead to a 12 meV worse sensitivity.

Mean background rate: 400 mcps

For 400 mcps (figure 6.9(b)) the standard deviation was determined to:

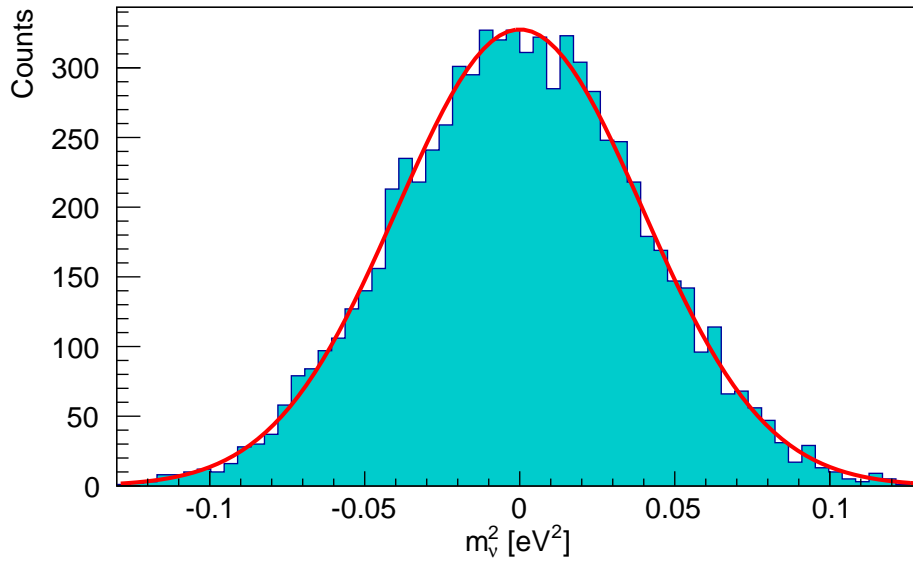
$$\sigma_{m_\nu^2, \text{stat}} = 0.0927 \pm 0.0008 \text{ eV}^2. \quad (6.20)$$

This yields a sensitivity at 90% C.L. of:

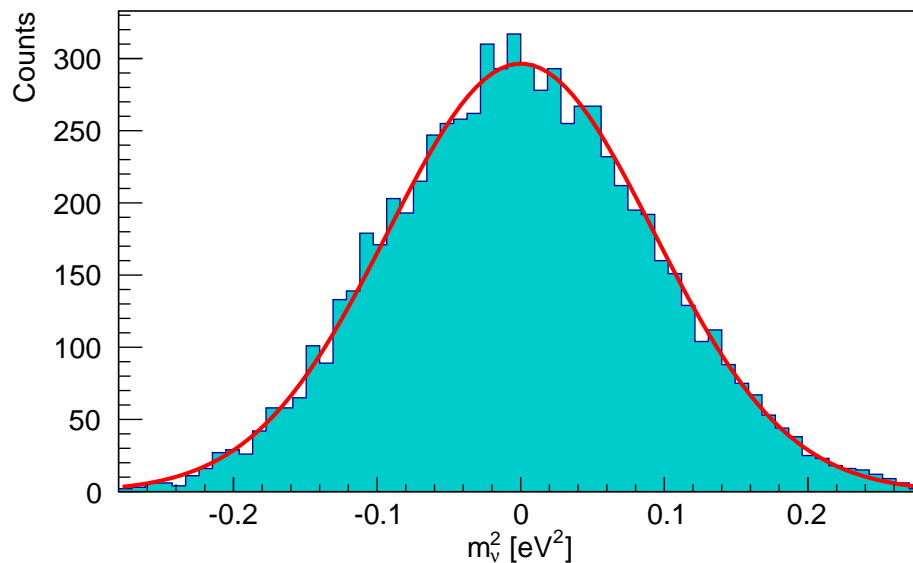
$$S_{m_\nu^2} = (393 \pm 2) \text{ meV}. \quad (6.21)$$

An ensemble test with sample size of 5000 and pure Poissonian background with mean rate of 400 mcps was performed for comparison. This yields a sensitivity of (324 ± 1) meV (90% C.L.). A deviation of 69 meV can be observed.

With the presented estimation within the uncertainties no impact of cosmic muon flux variations on the neutrino mass sensitivity at the KATRIN design background of 10 mcps could be observed. A clear trend appeared that this influence becomes important for background rates significantly larger than the design value compared to a pure Poissonian background. For a mean background rate of 100 mcps a decline of 12 meV could be



(a) 100 mcps



(b) 400 mcps

Figure 6.9.: Distribution of best fit squared neutrino masses for non-Poissonian backgrounds of 100 mcps and 400 mcps fitted with a Gaussian distribution. The simulated neutrino mass was set to $m_\nu=0$ eV.

observed. At a mean background rate of 400 mcps the sensitivity is by 69meV inferior. An overview of these results can be found in the tables 6.3. However, to make a reliable statement about the influence of the muon flux variations, coincidence measurements with muon panels and FPD are indispensable and are planned in the near future [74]. The presented background model is an estimation and the true behaviour of muon induced secondary electrons is unknown.

mean background [mcps]	$\sigma^{\text{non-pois}}[\text{eV}^2]$	$\sigma^{\text{poiss}}[\text{eV}^2]$
10	0.0166 ± 0.0001	0.0165 ± 0.0001
100	0.0396 ± 0.0003	0.0342 ± 0.0001
400	0.0927 ± 0.0008	0.0613 ± 0.0006
mean background [mcps]	$\mathbf{S}^{\text{non-pois}}[\text{meV}]$	$\mathbf{S}^{\text{poiss}}[\text{meV}]$
10	197 ± 1	197 ± 1
100	266 ± 1	254 ± 1
400	393 ± 2	324 ± 1

Table 6.3.: Overview of determined statistical uncertainties and sensitivities (90 % C.L.) on m_ν^2 with non-Poissonian background and reference values with Poissonian background.

7. Conclusion

The KATRIN experiment aims to determine the effective mass of the electron antineutrino with an unprecedented sensitivity of 200 meV by investigating the kinematics of tritium β -decay with a MAC-E filter. To reach its design sensitivity a total background rate of 0.01 cps is required.

One major background arises from muon induced secondary electrons from the inner spectrometer surface. For detailed investigations of this background source a set of large muon detectors is located close to the main spectrometer (chapter 3). This enables the search for coincidence events between muon detector hits and background counts at the FPD. By applying an asymmetric magnetic field with widened flux tube within the main spectrometer, secondary electrons are guided from the surface towards the detector. Most of them are reflected by the magnetic mirror effect, but a small fraction is able to reach the FPD. Such coincidence events were already found with measurements at the monitor spectrometer [58]. One strategy to search for such coincidences is to require that at least two muon detectors on opposing sides of the tank where hit. In this case the muons can cross the tank wall only in relative narrow regions, which can be exploited to reject secondary electrons from other region by cutting on the pixel distribution of the FPD. Most of the muons fly vertical through the spectrometer and the rate decreases strongly for larger polar angles. Therefore, in this measurement modus it is beneficial to have a module above the spectrometer to detect muons with small polar angles. Within the frame of this thesis, a small muon module was mounted on a movable platform above the spectrometer. As the sensitive area of the module above the spectrometer is small, one expects a very good spatial resolution for the coincidence events. Test measurements were performed to determine the rate of coincident events in the small module and any of the large modules on the ground (chapter 4) for different positions of the module on top. The highest coincidence rate (1.79 ± 0.01 cps) could be measured with the small module near the center of the spectrometer.

Monte Carlo Simulations were performed to compare the measurement results with theoretical expectations using Geant4 and Kassiopeia 5. Due to uncertainties in the angular distribution of the simulated cosmic muons and the positions of the muon detectors in the simulation, the simulated coincidence rates between the top module and the large module deviate by about 30% from the measured rates. A Geant4 simulation was used to extract the points on the spectrometer surface where muons detected in the muon detectors cross the spectrometer wall. This offers the possibility to derive predictions for coincidence measurements of the upcoming spectrometer detector system commissioning phase by tracking

particles from the respective regions on the surface through the spectrometer. The results of the simulations can confirm the expectation of a high spatial resolution on the surface and on the FPD as well.

The muon flux at sea level is not constant over time, but varies due to its dependence on several parameters like temperature or pressure in the atmosphere. This leads to a non-Poissonian distributed background component. Thus, a long term measurement (chapter 6) of the muon rate with 7 muon modules was performed to measure the magnitude of these variations. It was found that there are long term variations of about $\pm 3\%$ within a time window of 12 weeks. To estimate the influence of this systematic effect on the background rate, a sensitivity analysis was done using the Kasper module KaFit. A background model was developed that combines the expected Poissonian nature of the muon induced background on short time scales with its non-Poissonian nature on longer time scales with input of the measured muon flux variations. It should be mentioned that for the sensitivity studies a direct correlation between variations of the muon flux and variations of the muon induced secondary electrons was assumed. Long term coincidence measurements between muon modules and the FPD are planned in the near future in order to measure the correlation. The sensitivity investigation revealed that the impact of the muon flux variations on the neutrino mass sensitivity becomes larger for larger mean background rates.

The obtained sensitivities (90% C.L.) were compared to reference sensitivities with Poissonian distributed background [13]. For the design background value of 10 mcps no deviation from the reference value of 197 meV could be observed within the uncertainties of the simulation. At 100 mcps the obtained sensitivity is 266 meV and hence 12 meV larger than the reference value of 254 meV. For a mean background rate of 400 mcps, a sensitivity of 393 meV was determined. This is 69 meV larger compared to a Poissonian background. Under assumption of the used background model, a clear trend can be observed that the influence of muon flux variations on the neutrino mass sensitivity is very small for the design background rate and becomes more severe for higher background rates. Measurements to search for coincident events in muon modules and background events at the FPD are indispensable to understand the behaviour of muon induced background and its dependence from the variable muon flux. Such measurements are planned in the near future.

Bibliography

- [1] W. Pauli. Letter to Gauvereinstagung in Tübingen: "Sehr geehrte radioaktive Damen und Herren". *published in R.Kronig and V. Weisskopf (Eds.), Wolfgang Pauli, Collected scientific Papers, Vol.2, Interscience, New York (1964), 1930.*
- [2] C. L. Cowan, F. Reines, F. B. Harrison, H. W. Kruse, and A. D. McGuire. Detection of the Free Neutrino: a Confirmation. *Science*, 124(3212):103–104, 1956.
- [3] Y. Fukuda et al. Evidence for Oscillation of Atmospheric Neutrinos. *Phys. Rev. Lett.*, 81:1562–1567, Aug 1998.
- [4] J. Chadwick. Intensitätsverteilung im magnetischen Spektrum von β -Strahlen von Radium B+C. *Verh. d. Deutsch. Phys. Ges.*, 15:383, 1914.
- [5] F. A. Scott. Energy Spectrum of the β -Rays of Radium E. *Phys. Rev.*, 48:391–395, 1935.
- [6] J. Chadwick. Possible Existence of a Neutron. *Nature*, 312:312, 1932.
- [7] E. Fermi. Versuch einer Theorie der β -Strahlen. *Zeitschrift für Physik A*, 88:161–177, 1934. 10.1007/BF01351864.
- [8] J-M. Gaillard, K. Goulios, L. M. Lederman, N. Mistry, M. Schwartz, J. Steinberger, and G. Danby. Observation of High-Energy Neutrino Reactions and the Existence of Two Kinds of Neutrinos. *Phys. Rev. Lett.*, 9:36–44, 1962.
- [9] K. Kodama et al. Observation of tau neutrino interactions. *Phys. Lett. B*, 504(3):218–224, 2001.
- [10] Mary K. Gaillard, Paul D. Grannis, and Frank J. Sciulli. The standard model of particle physics. *Rev. Mod. Phys.*, 71(2):S96, 1999.
- [11] G. Aad and others (ATLAS Collaboration). Observation of a New Particle in the Search for the Standard Model Higgs Boson with the ATLAS Detector at the LHC. *Phys. Lett. B*, 716(1):1–29, 2012.
- [12] CMS Collaboration. Combined results of searches for the standard model Higgs boson in pp collisions at $\sqrt{s} = 7$ TeV. *Phys. Lett. B*, 710(1):26–48, 2012.
- [13] Marco Kleesiek. *A Data-analysis and Sensitivity-Optimization Framework for the KATRIN Experiment*. PhD thesis, Karlsruher Institut für Technologie (KIT), 2014.
- [14] J. N. Bahcall, A. M. Serenelli, and S. Basu. New Solar Opacities, Abundances, Helioseismology, and Neutrino Fluxes. *Astrophys. J.*, 621(1):85–88, 2005.
- [15] Borexino Collaboration. Measurement of geo-neutrinos from 1353 days of Borexino-Physics Letters B. *Physics Letters B*, B722, 2013.
- [16] B. Pontecorvo. *Zh. Eksp. Teor. Fiz.*, 34:247, 1957.

- [17] Z. Maki, M. Nakagawa, and S. Sakata. Remarks on the unified model of elementary particles. *Prog. Theor. Phys.*, 28(5):870–880, 1962.
- [18] R. Davis. A review of the Homestake solar neutrino experiment. *Prog. Part. Nucl. Phys.*, 32:13–32, 1994.
- [19] SNO Collaboration. Independent Measurement of the Total Active ^8B Solar Neutrino Flux Using an Array of ^3He proportional counters at the Sudbury Neutrino Observatory. *Phys. Rev. Lett.*, 101(111301), 2008.
- [20] GALLEX Collaboration. GALLEX solar neutrino observations: results for GALLEX IV. *Phys. Lett. B*, 447(1-2):127–133, 1999.
- [21] GNO Collaboration. Complete results for five years of GNO solar neutrino observations. *Phys. Lett. B*, 616(3-4):174–190, 2005.
- [22] Kamiokande Collaboration. Solar Neutrino Data Covering Solar Cycle 22. *Phys. Rev. Lett.*, 77:1683–1686, 1996.
- [23] Q. R. Ahmad (SNO Collaboration). Direct Evidence for Neutrino Flavor Transformation from Neutral-Current Interactions in the Sudbury Neutrino Observatory. *Phys. Rev. Lett.*, 89(011301), 2002.
- [24] B. Aharmim and others (SNO Collaboration). Determination of the ν_e and total $B8$ solar neutrino fluxes using the Sudbury Neutrino Observatory Phase I data set. *Phys. Rev. C*, 75(4):045502, 2007.
- [25] K. A. Olive et al. Review of particle physics. *Chin. Phys.*, C38(090001), 2014.
- [26] G. Drexlin, V. Hannen, S. Mertens, and C. Weinheimer. Current Direct Neutrino Mass Experiments. *Adv. in High Energy Phys.*, 2013(293986), 2013.
- [27] KATRIN Collaboration. Katrin design report 2004. Technical Report FZKA 7090, Forschungszentrum Karlsruhe, 2005.
- [28] S. R. Elliot, A. A. Hahn, and M. K. Moe. Direct evidence for two-neutrino double-beta decay in ^{82}Se . *Phys. Rev. Lett.*, 59(18):2020–2023, 1987.
- [29] M. Schlösser. *Accurate calibration of the Raman system for the Karlsruhe Tritium Neutrino Experiment*. PhD thesis, KIT, 2013.
- [30] R. Beuselinck, J. Sedgbeer, and Y. Shitov. The Supernemo Experiment.
- [31] E. Majorana. Teoria simmetrica dell elettrone e del positrone. *Il Nuovo Cimento (1924-1942)*, 14:171–184, 1937.
- [32] H. V. Klapdor-Kleingrothaus, A. Dietz, H. L. Harney, and I. V. Krivosheina. Evidence for Neutrinoless Double Beta Decay. *Mod. Phys. Lett. A*, 16:2409–2420, 2001.
- [33] C. E. Aalseth et al. Comment on 'Evidence for Neutrinoless Double Beta Decay'. *Mod. Phys. Lett. A*, 17(22):1475–1478, 2002.
- [34] S. Schönert et al. Status of the GERmanium Detector Array (GERDA) for the search of neutrinoless $\beta\beta$ decays of ^{76}Ge at LNGS. *Prog. Part. Nucl. Phys.*, 57(1):241–250, 2006.
- [35] E. Aguayo et al. The MAJORANA Experiment. *AIP Conf. Proc.*, 1417:95–99, 2011.
- [36] M. Sisti et al. From Cuoricino to CUORE: Investigating neutrino properties with double beta decay. *Journal of Physics: Conference Series*, 203(1):012069, 2010.
- [37] M. Auger et al. Search for Neutrinoless Double-Beta Decay in ^{136}Xe with EXO-200. *Phys. Rev. Lett.*, 109(032505), 2012.

- [38] M. Agostini et al. Results on Neutrinoless Double- β -Decay of ^{776}Ge from Phase I of the GERDA Experiment. *Phys. Rev. Letters*, 111(122503), 2013.
- [39] J. C. Mather et al. A preliminary measurement of the cosmic microwave background spectrum by the cosmic background explorer (COBE) satellite. *Astrophys. J.*, 354:37–40, 1990.
- [40] A. A. Penzias and R. W. Wilson. A Measurement of Excess Antenna Temperature at 4080 Mc/s. *Astrophys. J.*, 142(1):419–421, 1965.
- [41] Planck Collaboration. Planck 2013 results. XVI. Cosmological parameters. 2013. Submitted to *Astron. Astrophys.*
- [42] Ch. Kraus et al. Final results from phase II of the Mainz neutrino mass search in tritium. *Eur. Phys. J. C*, 40:447–468, 2005.
- [43] E. Otten and C. Weinheimer. Neutrino mass limit from tritium beta decay. *Rep. Prog. Phys.*, 71:36 pp., 2008.
- [44] V. M. Lobashev et al. Direct search for neutrino mass and anomaly in the tritium beta-spectrum: Status of troitsk neutrino mass experiment. *Nucl. Phys. B Proc. Suppl.*, 91(1-3):280–286, 2001. Neutrino 2000.
- [45] V. V. Aseev et al. Upper limit on the electron antineutrino mass from the troitsk experiment. *Phys. Rev. D*, 84(112003), 2011.
- [46] G. Altarelli and K. Winter. *Neutrino Mass*. Springer Tracts in Modern Physics. Springer, 2003.
- [47] Florian M. Fränkle. *Background Investigations of the KATRIN Pre-Spectrometer*. PhD thesis, Karlsruher Institut für Technologie (KIT), 2010.
- [48] J. Beamson et al. The collimating and magnifying properties of a superconducting field photoelectron spectrometer. *J. Phys. E*, 13(64), 1980.
- [49] V. M. Lobashev and P. E. Spivak. A method for measuring the electron antineutrino rest mass. *Nucl. Instrum. Methods Phys. Res., Sect. A*, 240(2):305–310, 1985.
- [50] A. Picard et al. A solenoid retarding spectrometer with high resolution and transmission for keV electrons. *Nucl. Instrum. Methods Phys. Res., Sect. B*, 63(3):345–358, 1992.
- [51] Nancy Wandkowsky. *Study of background and transmission properties of the KATRIN spectrometers*. PhD thesis, Karlsruher Institut für Technologie (KIT), 2013.
- [52] M. Babutzka et al. Monitoring of the operating parameters of the KATRIN Windowless Gaseous Tritium Source. *New J. Phys.*, 14(103046), 2012.
- [53] S. Grohmann et al. Precise temperature measurement at 30 K in the KATRIN source cryostat. *Cryogenics*, 51(8):438 – 445, 2011.
- [54] M. Röllig. Studien zu einem Röntgendetektorsystem zur Bestimmung der Aktivität in der KATRIN Tritiumquelle. Master’s thesis, KIT, 2011.
- [55] S. Mertens, G. Drexlin, F. Fränkle, D. Furse, F. Glück, et al. Background due to stored electrons following nuclear decays in the KATRIN spectrometers and its impact on the neutrino mass sensitivity. *Astropart. Phys.*, 41:52–62, 2013.
- [56] M. Erhard, S. Bauer, A. Beglarian, T. Bergmann, J. Bonn, G. Drexlin, J. Goullon, S. Groh, F. Glück, M. Kleesiek, N. Haußmann, T. Höhn, K. Johnston, M. Kraus, J. Reich, O. Rest, K. Schlösser, M. Schupp, M. Slezák, T. Thümmler, D. Vénos,

- C. Weinheimer, S. Wüstling, and M. Zbořil. High-voltage monitoring with a solenoid retarding spectrometer at the KATRIN experiment. *Journal of Instrumentation*, 9(6):P06022, 2014.
- [57] Johannes S. Schwarz. *The Detector System of the KATRIN Experiment - Implementation and First Measurements with the Spectrometer*. PhD thesis, Karlsruher Institut für Technologie (KIT), 2014.
- [58] Benjamin Leiber. *Investigations of background due to secondary electron emission in the KATRIN-experiment*. PhD thesis, Karlsruher Institut für Technologie (KIT), 2014.
- [59] H. Higaki et al. Electrons Confined with an Axially Symmetric Magnetic Mirror Field. *AIP Conference Proceedings*, 1037(1):106–114, 2008.
- [60] N. Wandkowsky, G. Drexlin, F.M. Fränkle, F. Glück, S. Groh, and S. Mertens. Validation of a model for radon-induced background processes in electrostatic spectrometers. *Journal of Physics G: Nuclear and Particle Physics*, 40(8):085102, 2013.
- [61] S. Görhardt. *Background Reduction Methods and Vacuum Technology at the KATRIN Spectrometers*. PhD thesis, Karlsruher Institut für Technologie (KIT), 2014.
- [62] S. Mertens. *Study of Background Processes in the Electrostatic Spectrometers of the KATRIN Experiment*. PhD thesis, KIT, 2012.
- [63] P. Rovedo. Muon induced secondary electrons at the katrin experiment detector installation and setup and data analysis. Diploma thesis, Karlsruher Institut für Technologie (KIT), 2013.
- [64] M. Howe. ORCA - Object-oriented Real-time Control and Acquisition.
- [65] O.C. Allkofer. *Introduction to Cosmic Radiation*. Karl Thiemig, 1975.
- [66] B. Leiber and F. Glück. Muon-flux on MainSpectrometer. Electronic Logbook Entry.
- [67] I. Klimushin, E. V. Bugaev, and I. A. Sokalski. Parametrisation of atmospheric muon angular flux underwater. *Phys. Rev. D*, 64(014016), 2001.
- [68] J. Allison et al. Geant4 developments and applications. *IEEE Transactions on Nuclear Science*, 53(1):270–278, feb. 2006.
- [69] H. Hucker. Bogensteg-Uebersicht, 2009. KATRIN internal document.
- [70] D. Furse et al. Kassiopeia - the simulation package for the KATRIN experiment. in preparation.
- [71] A. Müller. Untersuchung von elektrischen und magnetischen abschirmfaktoren am katrin hauptspektrometer. Diploma thesis, Karlsruher Institut für Technologie (KIT), 2014.
- [72] Johanna Linek. Master’s thesis, Karlsruher Institut für Technologie (KIT), 2015. in preparation.
- [73] M. Hötzel. *Simulation and analysis of source-related effects for KATRIN*. PhD thesis, KIT, 2012.
- [74] G. Drexlin and J. Linek. Mini-Proposal SDS-II-BG08, 2014. KATRIN internal document.
- [75] Exhibit 3.0 website. <http://www.simile-widgets.org/exhibit3/>.

Appendix

A. 2D Simulation of Radon First Spike Events

A major background component in the the main spectrometer is the decay of radon atoms in the volume of the spectrometer and the release of high-energy electrons in processes accompanying the α -decay, such as shake-off, auger or internal conversion (see also chapter 2.4.2). Under ultra high vacuum (UHV) conditions these electrons can be stored inside the main spectrometer up to hours due to the magnetic mirror effect, while they cool down via ionisation of residual gas molecules. The secondary electrons are accelerated by the electric potential and thus have energies in the region of interest by the time they hit the detector. The motion of the stored particles can be divided into 3 superimposed components (figure A.1). 1: The stored particles move along the magnetic field lines in axial direction until they are reflected due to the magnetic mirror effect. 2: Inhomogeneities in the electric and magnetic field cause a $\vec{E} \times \vec{B}$ and a $|\nabla\vec{B}| \times \vec{B}$ drift. This results in a slow motion on an azimuthal path around the spectrometer axis (magnetron drift). 3: Additionally, there is a fast cyclotron motion around the magnetic guiding field.

A.1. Spike Events

During the first commissioning measurement phase of the combined main spectrometer and detector system (SDS1) in summer/autumn 2013, detailed studies of radon induced background were performed [57]. While electrons are stored within the spectrometer, an increased detector rate is expected. The typical storing times at UHV conditions are much longer than the time between two radon decays. This yields in an temporal overlap of stored particles. Therefore, the secondary electrons they produce can not be detected individually. Thus, the pressure was artificially elevated by injecting argon into the main spectrometer to decrease the storage times. At elevated pressure it is possible to resolve single decays in the background rate. As argon is a noble gas, it is not problematic to get rid of it later to achieve an ultra high vacuum again.

The detector rate over about 3 hours is shown in figure A.2 for low and elevated pressure in the region of interest. As expected for high pressure, one can see spikes in the detector rate over short times. Each spike comes from one stored particle causing a burst of secondary electrons at the detector. For low pressure, no spikes are visible and the rate stays rather constant over the whole time due to the long storage times, which means the time intervals while electrons are stored overlap. At the top on the right of the figure the rate distribution of individual detector pixels of one single spike is shown. A number of 55 events were detected within a time interval of 672 ms. One can observe a ring-like pattern, which is caused by the magnetron motion of the primary electron. The ring is smeared due to the superimposed cyclotron motion. Due to a misalignment of main spectrometer and FPD, the center of the ring (black dot) does not exactly match the center of the FPD.

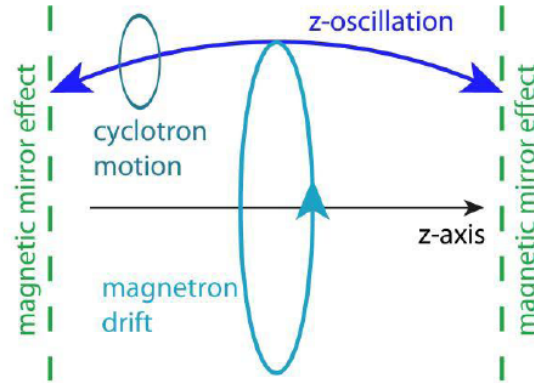


Figure A.1.: Illustration of stored particle motion. The motion can be divided into 3 components. The particle moves in axial direction until it is reflected because of the magnetic mirror effect. Superimposed it performs a magnetron drift with large radius and a cyclotron motion with small radius [47].

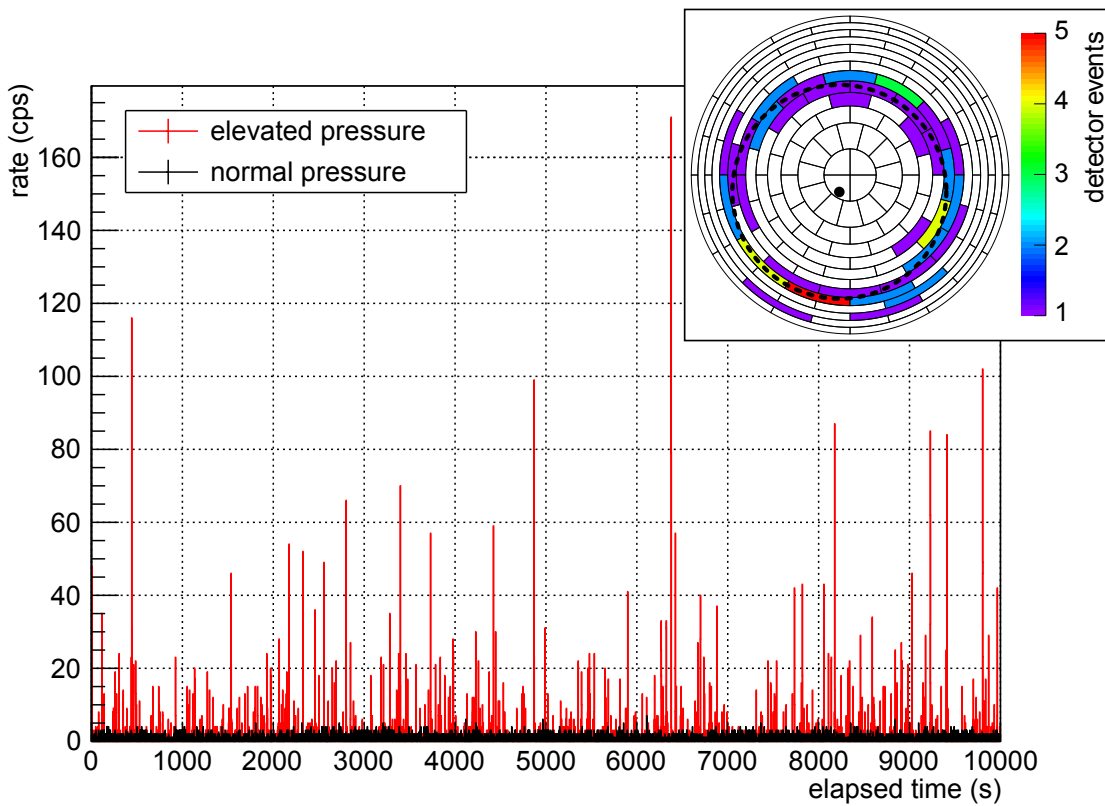


Figure A.2.: Rate over about 3 hours at elevated and low pressure. For elevated pressure over short times of less than a second, spikes are visible, that originate from stored electrons. A ring-like pattern is visible at the detector waver due to the magnetron drift of the stored particles. The superimposed cyclotron motion leads to a smearing of the ring. For low pressure the time intervals where particles are stored overlap due to the long cool down time. Thus no spikes can be observed. Taken from [57]

A spike event is defined by the following criterias:

- One radon spike has at least 3 events to reject events where two counts of other origin occur accidentally within a short time interval.
- The maximum inter-arrival time between 2 events within a spike is $\Delta t < 0.2$ s.
- A spike is caused by one stored electron coming from one radon decay.

The individual pixels of the detector waver have equal areas, but the volume they 'see' inside the main spectrometer differs. To determine the frequency spikes occur at a specific radius, it is reasonable to look at the first events in a spike. Thereby one can obtain informations about the distribution of radon decays independent of the number of secondary electrons in a spike. By normalising the rates to same volumes one might expect the rates to be equal for all pixels. In contrast measurements showed that the number of first spike events normalised to the volume increases for higher radii. For details see section A.3. The hypothesis that this effect is caused by the cyclotron motion of stored electrons from outside the flux tube which produce secondary electrons along their path was checked with a simplified two-dimensional simulation.

A.2. Simulation Model

A two dimensional model was developed that describes the trajectory of stored electrons projected to the analysing plane. The flux tube in the analysing plane is represented by a circle with radius 2.72 m around the point (0,0). The rotation axis of the spectrometer beam line is perpendicular to the plane and goes through the center of the circle in this model. The electron starting coordinates were generated uniformly distributed over the whole plane. These coordinates represent the positions of decaying radon atoms. The initial electron velocity direction is defined by an azimuthal and polar angle. The polar angles were diced uniformly whereas for the polar angles a $\sin(\Theta)$ distribution was used in order to account for the isotropic emission behaviour of electrons released in radon decays. Electron energies were set according to the expected energy spectrum of the radon isotope ^{219}Rn with shortest half live (~ 4 s). The spectrum with the various electron production mechanisms provided by Kassiopieia's radon event generator [51] is visualised in figure A.3. The spectrum of the isotope ^{220}Rn looks very similar. The absolute velocity value was calculated and with azimuthal and polar angle the velocity component parallel to the analysing plane v_{\perp} . The cyclotron radius is given by

$$R = \frac{m_e \cdot v_{\perp}}{e \cdot B} \quad (7.1)$$

As the bulk of the electrons has energies below 10 keV and the maximum energies are in the order of 200 keV, the electrons were treated to be non-relativistic. With the starting point, cyclotron radius and the initial direction of the electrons, the trajectory projected to the analysing plane was calculated and is illustrated in figure A.4. Then a point of first ionisation i.e. a first spike event was chosen randomly, as only the pure trajectory is determined and no interactions with residual gas molecules. If the ring was located completely within the flux tube, one random point of the whole ring was chosen. In case the cyclotron ring was not completely inside the flux tube, the intersection points of the two rings were determined analytically. The point of first ionisation then was taken as a random point on the fraction of the trajectory which is located within the flux tube. If there is no overlap of the trajectory and the flux tube the event was rejected as the produced secondary electrons can not reach the detector. The number of possible ionisation events on a ring segment is given by the initial energy of the stored particle over the mean ionisation energy loss for hydrogen (35 eV). This number has to be divided by 2 to consider the fact that only about the half of the secondary electrons are accelerated towards the detector.

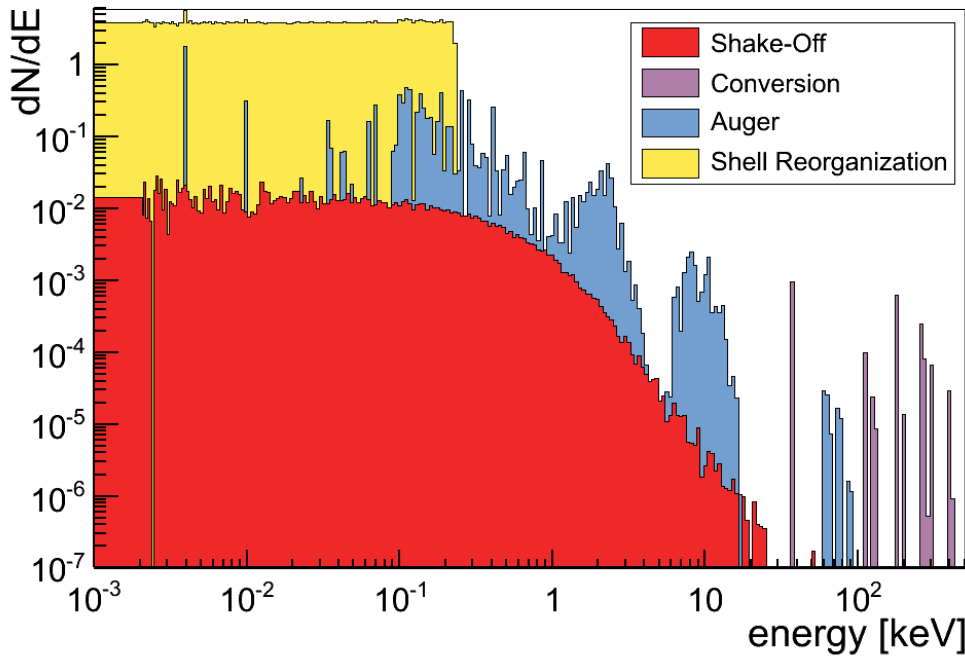


Figure A.3.: Electron energy spectrum from ^{219}Rn decays. Electrons from a few eV up to more than 100 keV are emitted [51].

The remaining electrons are accelerated into the other direction and thus do not contribute to the detected spike events. If the number of possible ionisation events on the respective ring segment is smaller than 3, the event was rejected as a spike is defined to have at least 3 events. Finally the distance from the first ionisation point to the center of the ring was calculated for comparison with the measured radial distribution. This simple model has the big advantage that the trajectory projected to the analysing plane can be calculated analytically. Therefore, no complex particle tracking is required and the simulation is very fast. However, it is a very simplified approach that only considers the cyclotron motion and not the complete trajectory including magnetron drift or axial motion.

A.3. Comparison of Simulation and Data

Figure 7.5(a) shows the measured radial distribution of the first spike event for the 9 G setting at elevated pressure projected to the analysing plane and normalised to the volume the rings 'see' in the main spectrometer. The bins belong to the 13 detector rings and thus get smaller for larger radii. Also shown are the results of the two dimensional model. The simulated data is normalised to the area of the respective ring projected to the analysing plane. The flux tube (191.1 Tm^2) of the 9 G magnetic field setting has a radius of about 2.72 m in the analysing plane. Each bin contains the summed number of first spike events of all pixels on the respective detector ring. The rate increases at higher radii. Electrons with a magnetron radii larger than the flux tube in the analysing plane can anyhow ionise atoms within the sensitive volume because of their cyclotron motion. The simulated radial distribution is in good agreement with the measured data, but at the beginning of the ascent at about 2.1 m a trend of underestimation can be observed.

The probability P , if an electron can create a spike event within the flux tube depends on its starting point, its initial velocity direction and its energy. The number of simulated electrons N_{yes} fulfilling these requirements and the number of electrons that do not N_{no}

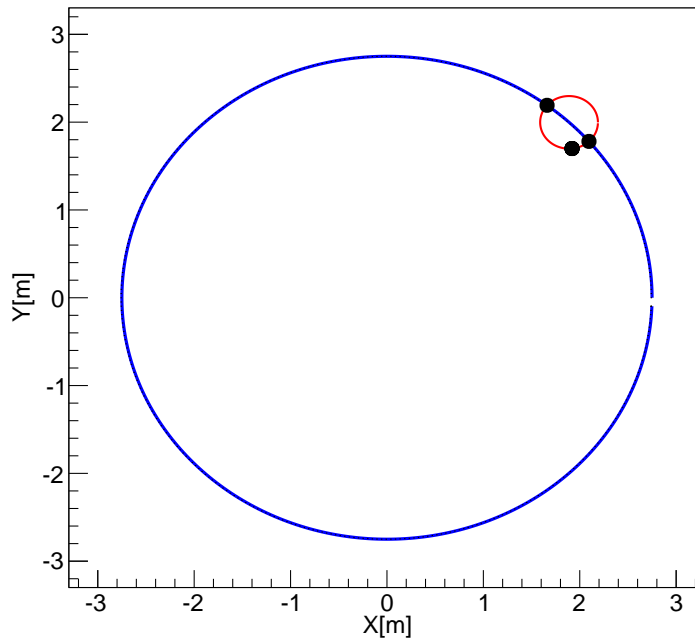
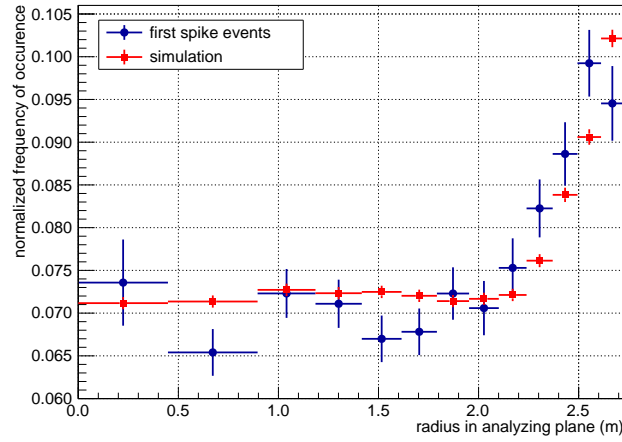


Figure A.4.: Illustration of electrons starting in the analysing plane moving on cyclotron paths (small red ring). The large blue ring represents the flux tube in the analysing plane. Marked are the intersection points and a randomly selected point on the fraction of the trajectory inside the flux tube.

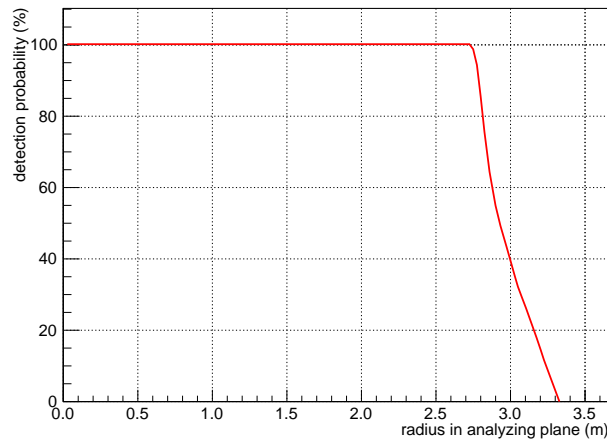
were determined. The probability P is then given by their ratio:

$$P = \frac{N_{\text{yes}}}{N_{\text{no}}} \quad (7.2)$$

Figure 7.5(b) shows this probability over radius. For distances higher than the flux tube radius in the analysing plane the probability drops as only a fraction of the simulated events has appropriate energy and v_{\perp} in order that the trajectory covers a sufficient large area of the flux tube. High energetic electrons still can be detected at radii of ≈ 3.3 m where only high energetic electrons from outside can cross the flux tube. The simulation can confirm the hypothesis and shows that spike events can originate from electrons outside the flux tube.



(a) Radial distribution



(b) Detection probability

Figure A.5.: **a**: Radial distribution of first spike events of a 2D simulation and measurements at elevated pressure for the 9 G magnetic field setup. The rate increases for higher radii because stored electrons with magnetron radius larger than the flux tube radius can create secondary electrons within the sensitive area. The simulated and measured distributions are in good agreement. **b**: Probability that an electron starting at a specific radius can create a spike event (9 G). The sensitive radius of the sensitive area within the analysing plane is 2.72 m. Due to the cyclotron motion of the electrons also electrons with a larger distance of starting point to the spectrometer axis have a chance to create spike events. Visualisation from [57]

B. Muon Flux Generator

It was experimented with the development of a muon rate generator. The idea is to imitate a signal with the same characteristics like the measured muon rate. This might offer the possibility to generate a "muon rate" over years based on the measured muon rate over a few months. Such a signal might be used to develop a more realistic background model than the model used in the sensitivity analysis (see chapter 6.3). In such a model one might generate a mean background rate for each time bin of the measurement time distribution and extract the number of background events of a Poissonian distributed background with the respective background rate. However, for this further software developments of the Kasper module KaFit were required.

The generator uses the muon rate data of the long term measurement. It is based on the trend the real muon rate evolves on two different time scales. For each time bin of the long term measurement, the relative deviation of the rate 12 and 24 hours later was calculated. For the start, the rate was set to an arbitrary value of 1. Then outgoing from this value a variation on the 24 hour scale was chosen randomly following the determined distributions. For the 12 hour scale two random values were chosen respectively. For each time scale the rate was interpolated between the points. The resulting rate was then chosen as the average of the two interpolated rates and the procedure was repeated with the last point of the resulting rate as new start value. Figure B.6 shows the generator principle. In principle more time scales are preferable. The major challenge to develop such a generator is it, to find the best combination and weighting of the influence of different time scales on the resulting rate.

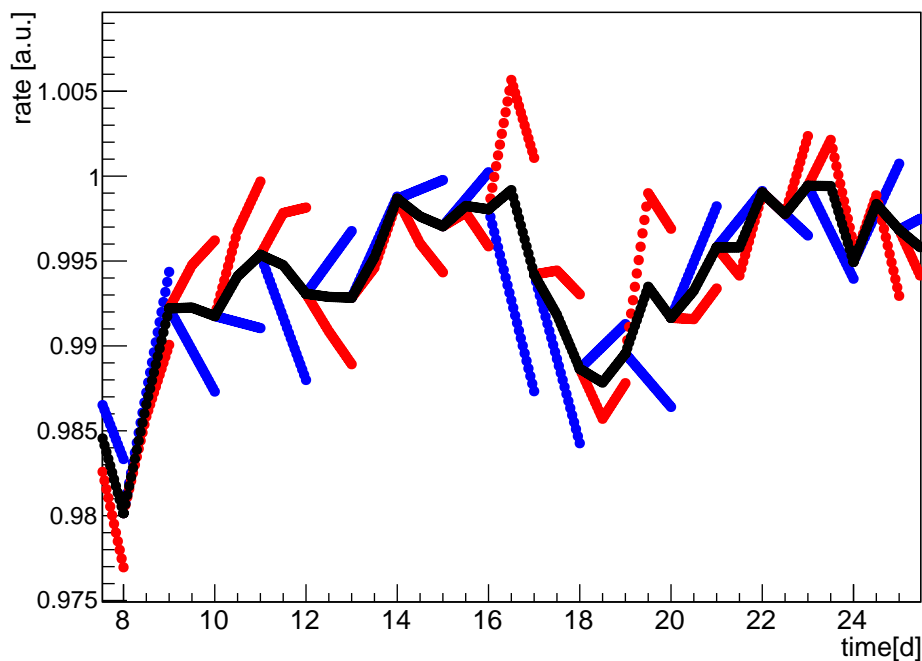


Figure B.6.: The figure shows the principle of the generator. Blue is the rate on the 24 hour scale, the 12 hour scale is red. The resulting rate is black.

C. Muon Panel Performance

Muon rates for single muon modules over 20 hours (runs:myo1410-myo1429):

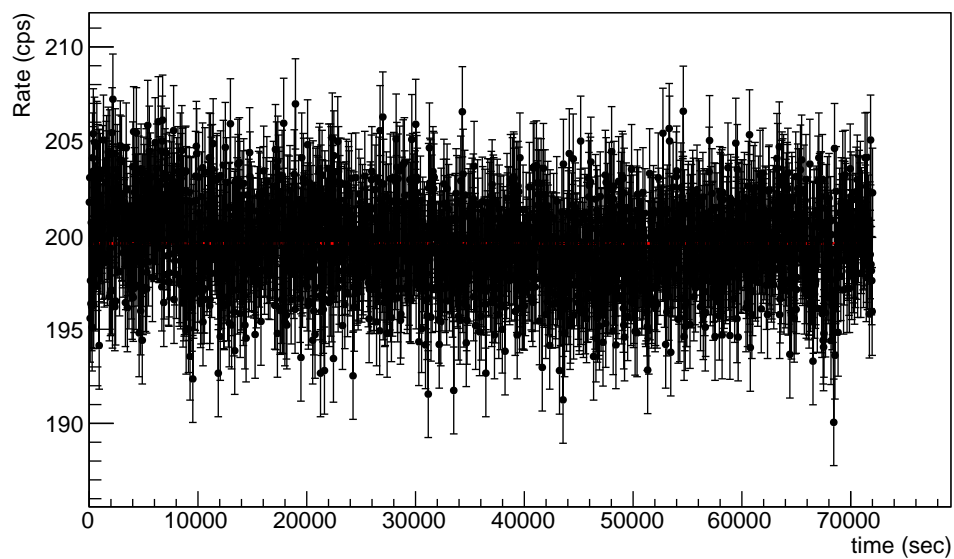


Figure C.7.: Muon rate measured with module 2. This module was excluded from the analysis due to inferior performance.

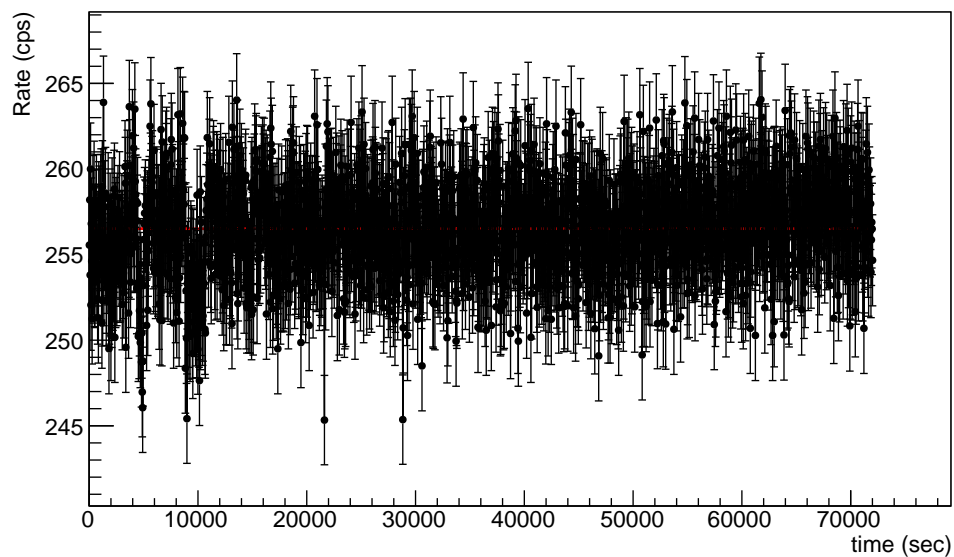


Figure C.8.: Muon rate measured with module 3

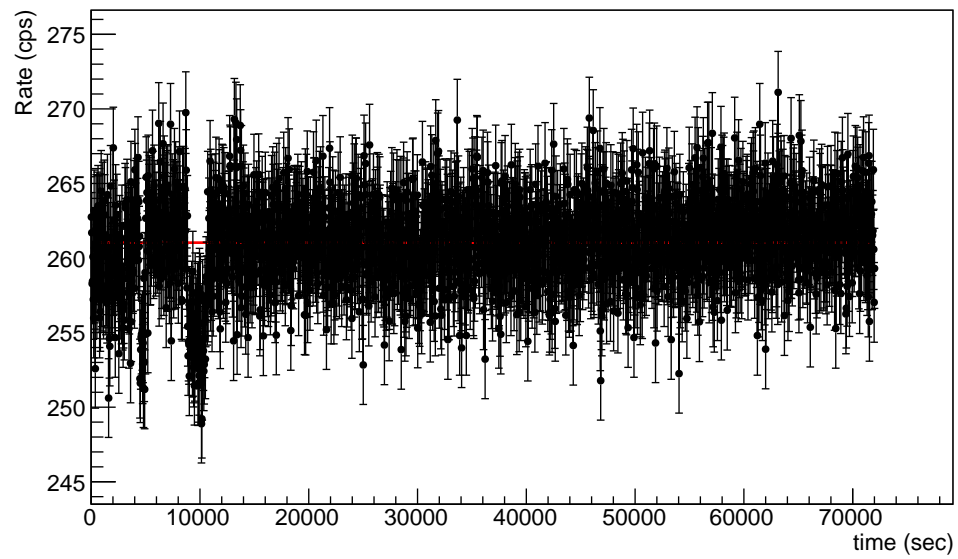


Figure C.9.: Muon rate measured with module 4

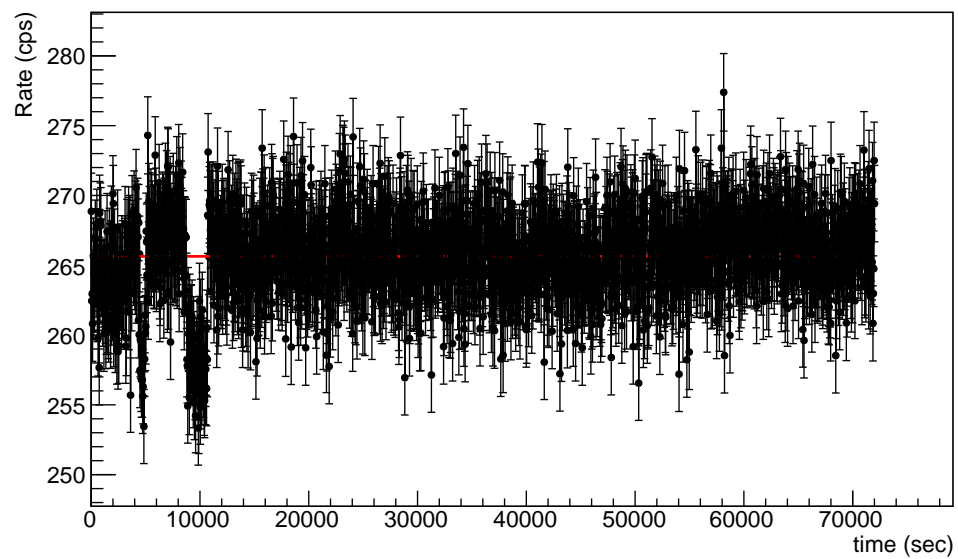


Figure C.10.: Muon rate measured with module 5

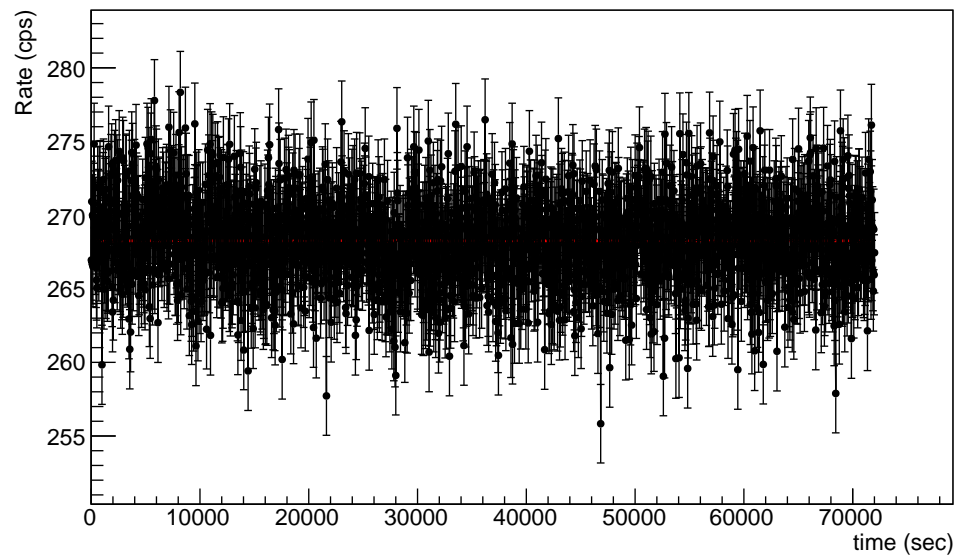


Figure C.11.: Muon rate measured with module 6

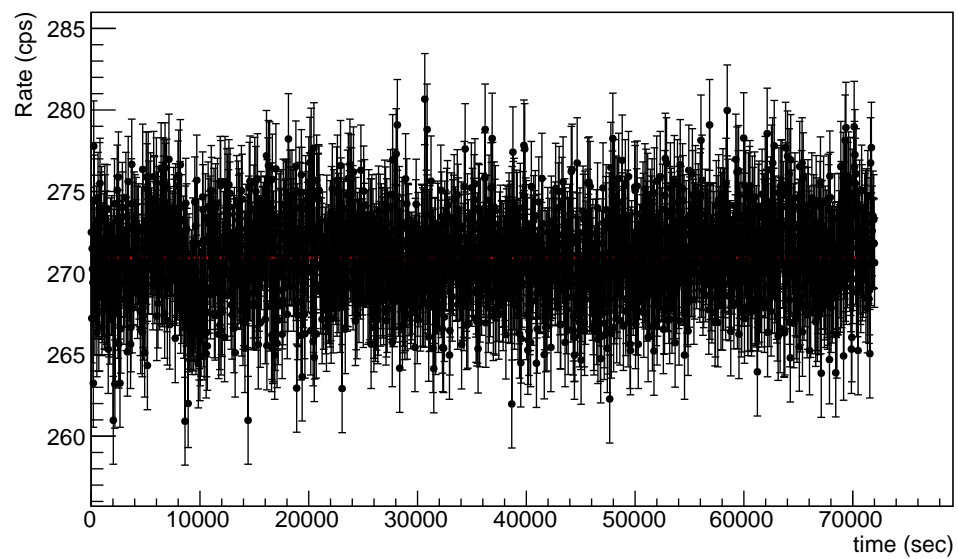


Figure C.12.: Muon rate measured with module 7

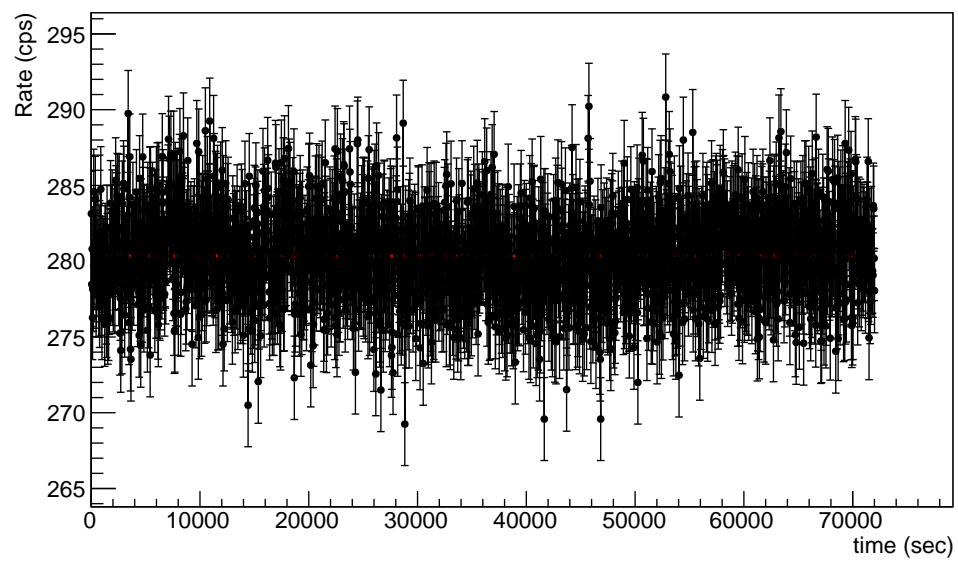


Figure C.13.: Muon rate measured with module 8

D. Surface Interaction Points of Coincidence Events

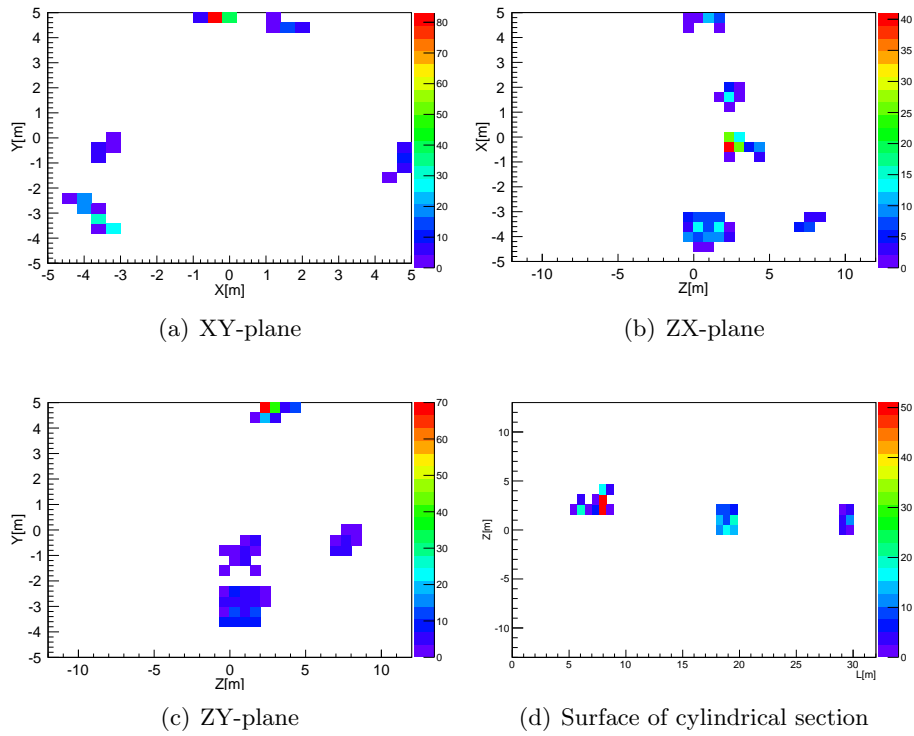


Figure D.14.: **Small module at position 2:** Coordinates for crossing points with tank wall of coincidence events between the small module and any module on the ground projected to different planes. For more information see section 5.4.

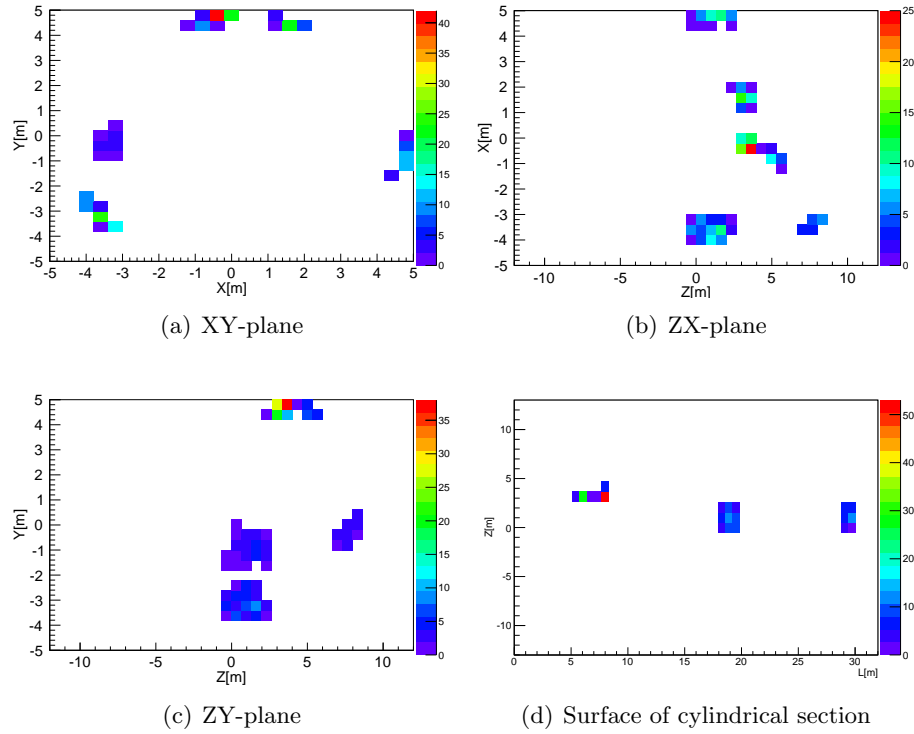


Figure D.15.: **Small module at position 3:** Coordinates for crossing points with tank wall of coincidence events between the small module and any module on the ground projected to different planes. For more information see section 5.4.

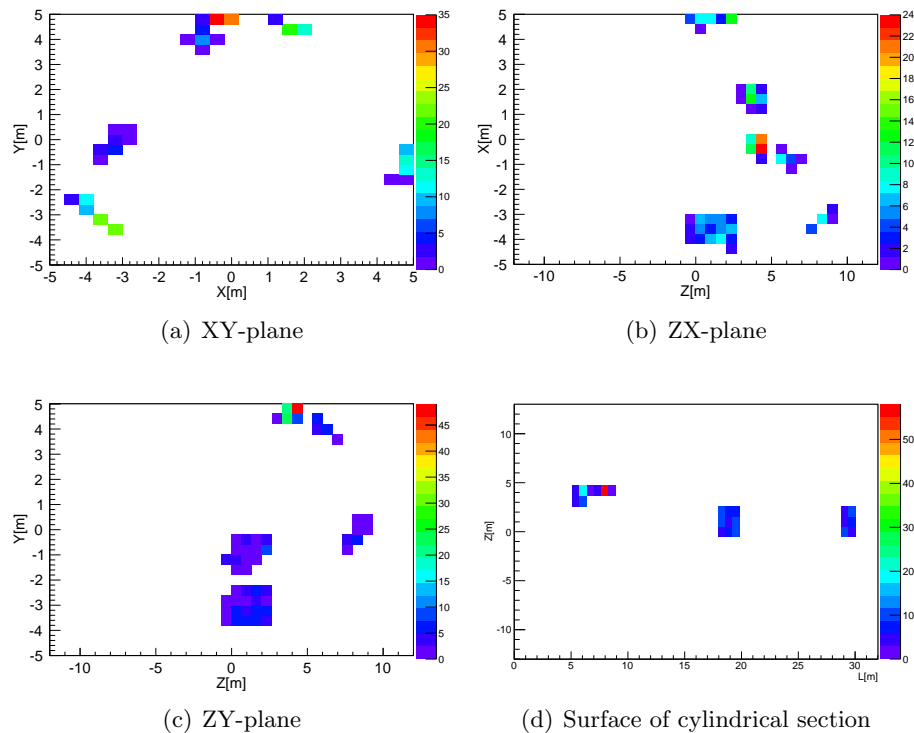


Figure D.16.: **Small module at position 4:** Coordinates for crossing points with tank wall of coincidence events between the small module and any module on the ground projected to different planes. For more information see section 5.4.

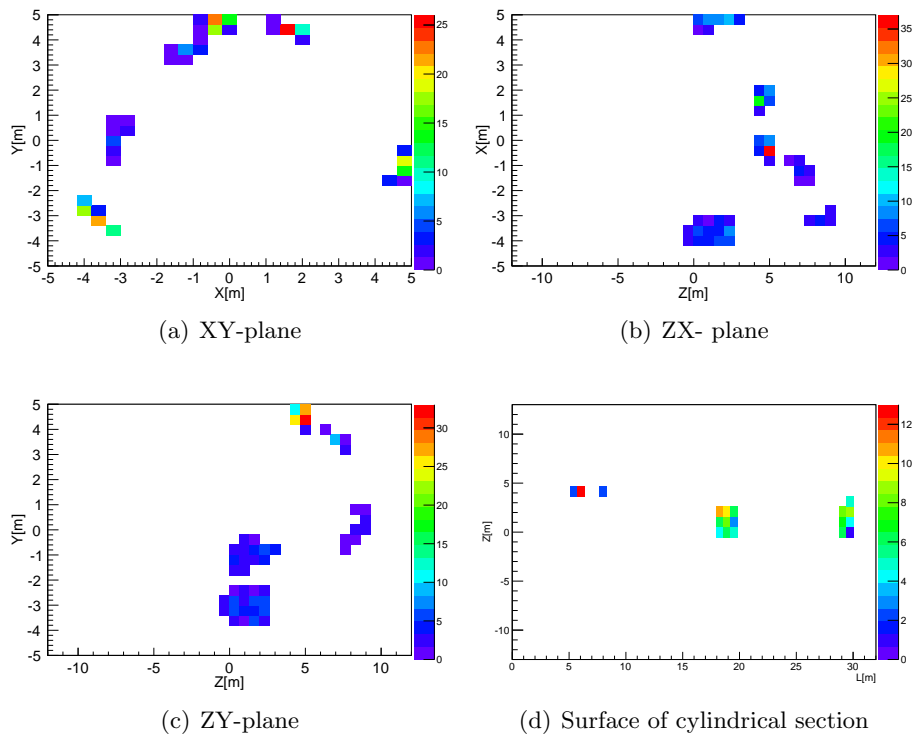
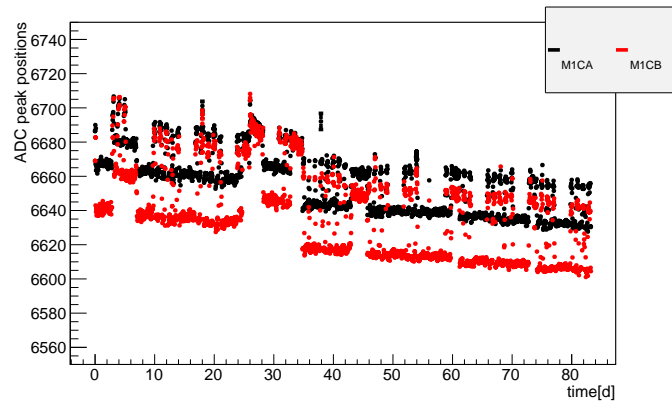
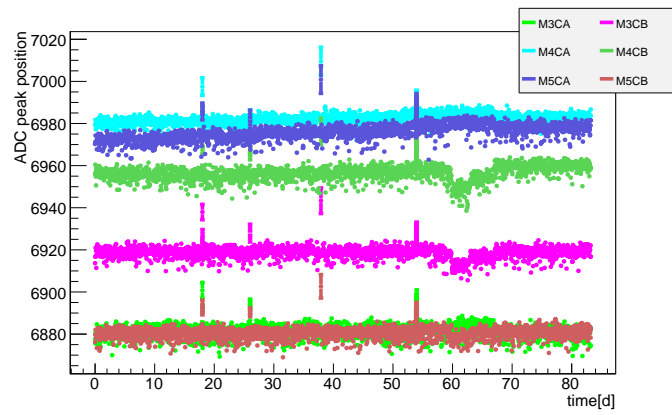


Figure D.17.: **Small module at position 5:** Coordinates for crossing points with tank wall of coincidence events between the small module and any module on the ground projected to different planes. For more information see section 5.4.

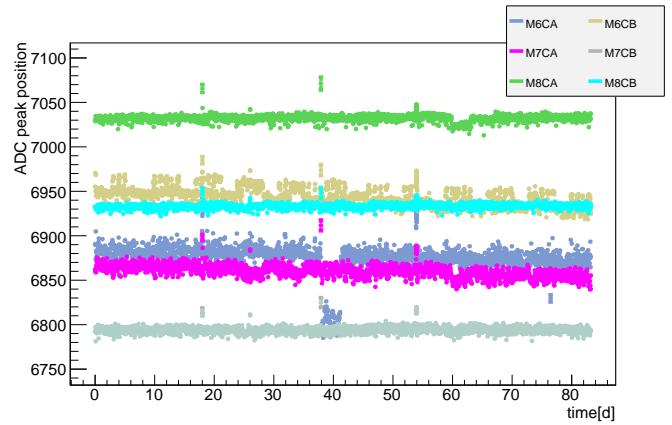
E. ADC Peak Positions



(a)



(b)



(c)

Figure E.18.: ADC peak positions during long term measurement.

F. Run Descriptions Web Page

For the SDS2 measurement phase a web page was set up that provides an FPD run overview with slow control data and some preview plots. Figure F.19 shows a screenshot of the web page with some sample data from 2013. The data access program KaLi is used to read out the mean values for several physical quantities. Preview plots are shown for the detector rate, energy histogram and the inter-arrival times using data analysis program Beans. A filter is implemented to select runs with specific characteristics. The page was created using Exhibit 3.0 [75].

Parameter	Katrin number
PAE Voltage[V]	"525-EHV-0-1050-0001"
Tank Voltage[V]	"436-WHV-0-9999-0003"
Dipole west[V]	"436-WHV-0-9999-0005"
Dipole east[V]	"436-WHV-0-9999-0006"
Current pinch magnet[A]	"521-ELV+0-1205-0001"
Current detector magnet[A]	"521-ELV-0-2205-0001"
Gamma source yes/no	"524-AAI-0-1100-0001"
Electron source yes/no	"524-AAI-0-2100-0001"
Pressure[mbar]	"432-RPI-3-3110"
Beam line gate valve open/closed	"522-VAO-3-1010-0301"
Air coil currents[A]	"433-ELV-1-030n-0001"
	(n=3-16)

Table F.1.: Katrin numbers of shown physical quantities

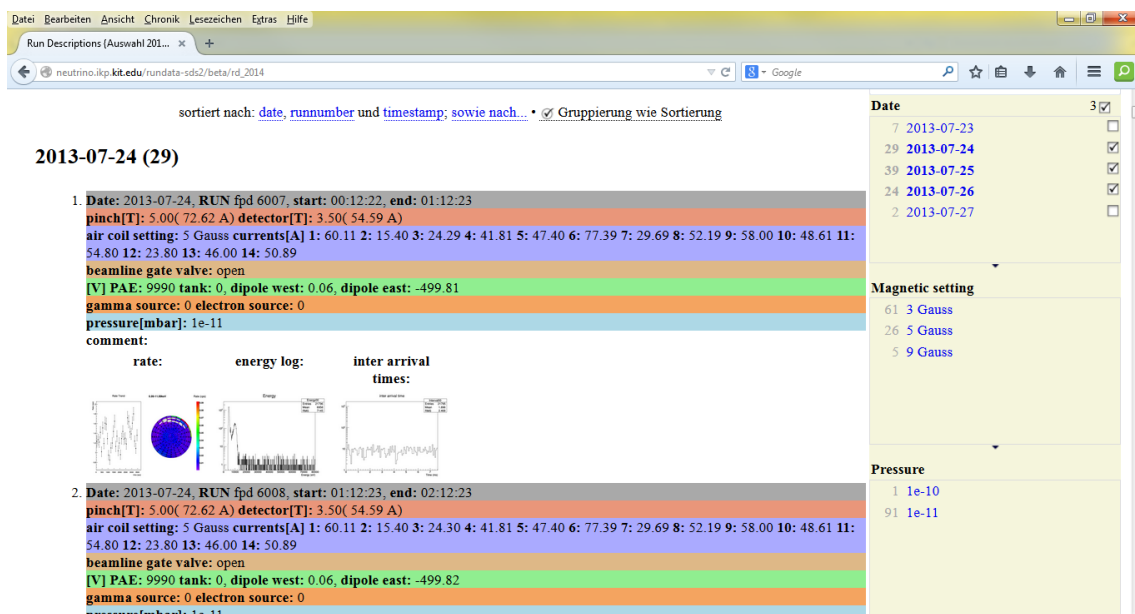


Figure F.19.: Screenshot of run descriptions web page with sample data from 2013.

List of Figures

1.1.	Radium spectrum	2
1.2.	Overview of elementary Standard Model particles	3
1.3.	Solar neutrino spectrum	5
1.4.	Neutrino fluxes (SNO)	6
1.5.	Results of neutrino mass measurements	8
1.6.	Feynman graph and spectrum of neutrinoless double β -decay	9
1.7.	Power spectrum and skymap of CMB anisotropies	10
2.1.	Tritium β -spectrum	12
2.2.	Schematic profile of MAC-E filter	13
2.3.	KATRIN experimental setup	14
2.4.	Windowless gaseous tritium source	14
2.5.	Differential and cryogenic pumping section	15
2.6.	Pre-spectrometer	16
2.7.	Overview of focal plane detector system	17
2.8.	Illustration of electron trajectories in MAC-E filter	18
3.1.	Schematic view of muon module	20
3.2.	Picture of muon modules 6-8	21
3.3.	Positions of muon modules	21
3.4.	Illustration of the filtering process in the DAQ-system	23
3.5.	Small muon module above main spectrometer	24
3.6.	Muon rate measured with module 1	25
3.7.	ADC histogram for two muon channels	25
3.8.	Muon rate measured with the small module	26
3.9.	ADC histogram for channels of small muon module	26
4.1.	Polar angle distributions for cosmic muons	28
4.2.	Measured coincidence rate between small module and any large module	29
4.3.	Coincidence rates for different positions of the small module	30
4.4.	Coincidence rate between large muon modules	30
5.1.	Geant4 simulation geometry	32
5.2.	Coordinates where muons of coincidence events cross the tank wall	36
5.3.	Points on cylindrical section where muons of coincidence events cross the wall	37
5.4.	Flux tube of asymmetric magnetic field	39
5.5.	Pixel distribution for coincidence events	39
6.1.	ADC histogram fitted with Gaussian distribution	42
6.2.	ADC peak positions of muon modules over 12 weeks	42
6.3.	Measured total muon rate over 12 weeks	44
6.4.	Deviation of measured muon rates to the mean rate of long term measurement	44
6.5.	List of systematic uncertainties	45

6.6.	Illustration of parameter inference from integrated β -spectrum	46
6.7.	Distribution of N^{bkg} for different mean background rates	50
6.8.	Best fit m_ν^2 with non-Poissonian background for 10 mcps	52
6.9.	Best fit m_ν^2 with non-Poissonian background for 100 mcps and 400 mcps . .	53
A.1.	Illustration of stored particle trajectory	62
A.2.	Background rate at elevated pressure	62
A.3.	^{219}Rn spectrum of radon event generator	64
A.4.	2D simulation of the cyclotron motion of electron in the analysing plane . .	65
A.5.	Comparison of 2D simulation results with measured data	66
B.6.	Illustration of muon flux generator principle	67
C.7.	Muon rate measured with module 2	69
C.8.	Muon rate measured with module 3	69
C.9.	Muon rate measured with module 4	70
C.10.	Muon rate measured with module 5	70
C.11.	Muon rate measured with module 6	71
C.12.	Muon rate measured with module 7	71
C.13.	Muon rate measured with module 8	72
D.14.	Coordinates where muons of coincidence events cross the tank wall (Position2)	73
D.15.	Coordinates where muons of coincidence events cross the tank wall (Position3)	74
D.16.	Coordinates where muons of coincidence events cross the tank wall (Position4)	74
D.17.	Coordinates where muons of coincidence events cross the tank wall (Position5)	75
E.18.	ADC peak positions during long term measurement.	77
F.19.	Screenshot of run descriptions web page	79

List of Tables

3.1. Assignment of FLT channels	22
4.1. Coincidence rates between the small and all large muon modules	29
5.1. Module positions implemented in Geant4 simulation	33
5.2. Parameters of $\cos^*(\theta)$ distribution	33
5.3. Simulated muon rate of the small module	34
5.4. Simulated coincidence rate between the small module and any large module	35
5.5. Asymmetric magnetic field setting.	40
6.1. Mean peak positions during long term measurement	43
6.2. Measurement time distribution	47
6.3. Statistical uncertainties and sensitivities for different background models . .	54
F.1. Katrin numbers of physical quantities shown on run descriptions web page .	79

Danksagung

An dieser Stelle möchte ich mich bei allen ganz herzlich bedanken, die mich bei dieser Arbeit unterstützt haben. Besonders hervorheben möchte ich:

- Prof. Dr. G. Drexlin für die Möglichkeit diese spannende Arbeit bei KATRIN durchführen zu können.
- Prof. Dr. U. Husemann für die Übernahme des Korreferats.
- Dr. Florian Fränkle für die tolle Betreuung und Unterstützung.
- Dr. Benjamin Leiber für seine ständige Hilfsbereitschaft und viele hilfreiche Anregungen.
- Dr. Marco Kleesiek für die große Unterstützung bei Fragen zu KaLi und KaFit.
- Prof. Dr. Sanshiro Enomoto für die schnelle Beantwortung aller meiner Fragen zu Beans.
- Holger Frenzel für die Hilfe bei der Montage des Myonmoduls.
- Johanna Linek für die gute Zusammenarbeit.
- Herbert Ullrich und Frank Bandenburg für nie langweilig werdende Mittagspausen.
- Und natürlich meiner Familie für die sowohl moralische als auch finanzielle Unterstützung während meines Studiums.